The Dissertation Committee for Taras Alexandrovich Kirichenko certifies that this is the approved version of the following dissertation:

Dynamics of Defects and Dopants in Complex Systems: Si and Oxide Surfaces and Interfaces

Committee:

Sanjay K. Banerjee, Supervisor

Gyeong S. Hwang, Supervisor

John G. Ekerdt

Archie Holmes, Jr.

Dim-Lee Kwong

Dynamics of Defects and Dopants in Complex Systems: Si and Oxide Surfaces and Interfaces

by

Taras Alexandrovich Kirichenko, B.S.;M.S.

Dissertation

Presented to the Faculty of the Graduate School of

The University of Texas at Austin

in Partial Fulfillment

of the Requirements

for the Degree of

Doctor of Philosophy

The University of Texas at Austin

May 2005

To my parents, Galina and Alexandr Kirichenko

Acknowledgments

First and foremost I am happy to have a chance to express my deepest gratitude to both of my advisors, Professor Sanjay K. Banerjee and Professor Geyong S. Hwang. I have been exceptionally fortunate to be working under their joint supervision. I greatly thank Professor Banerjee for giving me inspiration, intellectual freedom and encouragement to explore new ideas as well as the direction to see them through to completion. His broad expertise in the field and guidance have made it possible to accomplish this work. I am very grateful to Professor Hwang for the opportunity to learn from him and profit by his keen, incisive insight and his ability to see the "big picture". His standards of excellence are the ones that I aspire to make my own. Apart and beyond of these he afforded me great deal of his time, patience and tolerance.

I am very grateful to my colleagues and fellow graduate students, Scott Harrison, Decai Yu, Devina Pillay, Jason Kenney, Soohwan Lee, Yung Wang, Puneet Kohli, Li Lin and Swaroop Ganguly for their friendship, support and stimulating discussions. I appreciate the valuable feedback of Hong-Jyh Li and Raghu Shrinivasa when I joined the group. I thank all my friends and who made my graduate school experience memorable and enjoyable. Their names are too numerous to be listed here but their comradery deserves as much ac-

knowledgement.

I am forever grateful to my parents whose unconditional love and support enabled me to get this far. I would like to thank my wife, Ekaterina for her understanding and sharing of all pressures and joys throughout the years of graduate study.

Taras Alexandrovich Kirichenko

The University of Texas at Austin

May 2005

Dynamics of Defects and Dopants in Complex Systems: Si and Oxide Surfaces and Interfaces

Publication No. _____

Taras Alexandrovich Kirichenko, Ph.D.
The University of Texas at Austin, 2005

Supervisors: Sanjay K. Banerjee and Gyeong S. Hwang

Precise control of dopant redistribution and activation in the vicinity of the semiconductor-dielectric interface has become crucial for fabrication of deep sub-micron metal-oxide -semiconductor field-effect transistor devices. During the process of ion implantation and thermal oxidation a great number of native defects (such as vacancies and interstitials) can be created in the substrate. These defects are known to be mainly responsible for transient enhanced diffusion and electrical activation/deactivation of dopant impurities.

In this work we seek to develop a detailed understanding of the exact mechanisms of defect annihilation, and dopant diffusion and clustering/dissolution

in complex systems such as Si surfaces and amorphous-crystalline Si-Si and Si-SiO_2 interfaces using density functional theory total energy calculations.

- *Si(001) surface*

−We examine structure, energetics, and bonding of vacancies and interstitials on the clean and terminated Si(001) surface and its subsurface layers.

− We propose mechanism of vacancy stabilization at the surface and subsurface layers.

− We find Si(001) surface to be an effective sink for vacancies and interstitials, irrespective of surface passivation.

− We present diffusion pathways and barriers of vacancies at and in the vicinity of the clean surface.

− We have demonstrated that the stability of native defects within the topmost three subsurface layers is greatly influenced by surface passivation.

- *Amorphous-crystalline Si interface*

−We present native defect configurations, energetics and the origin of their stabilization at amorphous-crystalline Si interface and in amorphous Si.

−A continuous random network model is employed in the construction of a realistic *a-c* interface structures.

−We propose the 'sponge-like' behavior of the amorphous phase toward native defects.

- *Si/SiO_2 interface*

−We present stable Si interstitial structures at interface and in the oxide.

−We propose mechanism of interstitial diffusion from Si into *a*-SiO_2.

−We consider Boron-Interstitial pair behavior in vicinity of interface.

−We propose a novel mechanism of vacancy stabilization and vacancy cluster-

ing at interface.

We believe the findings we present here show the importance of understanding the role of surfaces and interfaces in affecting defect and dopant behavior in their vicinity. This research leads to an understanding of the broad range of phenomena applicable to modern microelectronics device fabrication and process modeling.

Contents

List of Tables

List of Figures

Chapter 1

Introduction

The primary focus this thesis work is on investigating the atomic and electronic structure and dynamical behavior of defects and dopant-defect complexes in disordered/strained Si and oxide systems, such as i) reconstructed Si surfaces and their subsurface layers, ii) amorphous SiO_2 thin layers, iii) amorphous-crystalline Si interfaces, iv) Si-SiO_2 interfaces. Defect-dopant dynamics is rather well understood in crystalline Si and SiO_2. However, little is known about their diffusion and annihilation (or precipitation) at the surfaces and interfaces, despite its growing importance in determining junction profiles as device dimensions get smaller.

Fabrication of forthcoming nanometer scale electronic devices faces many difficulties including the formation of extremely shallow and highly doped junctions[1]. Currently, ultra-low-energy ion implantation followed by high-temperature thermal annealing is most widely used to fabricate such shallow junctions[2]. In this process, a great challenge lies in achieving precise control

of redistribution and electrical activation of dopant impurities. Native defects (such as vacancies and interstitials) generated typically during dopant introduction into the substrate are known to be mainly responsible for the transient enhanced diffusion (TED)[3, 4, 5, 6] and also influence the electrical activation/deactivation of dopant impurities[7, 8, 9, 10, 11]. Over the last decades a great deal of experimental[12] and theoretical[13, 14, 15, 16, 17, 18] effort has been devoted to understanding the fundamental properties of vacancies and interstitials and their interactions with dopants in semiconductors and oxides[19]. Nonetheless, many fundamental aspects of the defect-dopant behavior are still poorly understood.

The Si surface[20, 21] and Si/SiO_2 interface[22, 23] have been considered as an effective sink for vacancies and interstitials, but a detailed study of the defect interactions with surface/interface is still lacking. The surface/interface annihilation will directly influence the population of defects in the substrate, which in turn affects the redistribution and electrical activation of injected dopant impurities[3, 24]. In addition, the precipitation of dopant impurities at the surfaces and interfaces is also an important issue in ultrashallow junction formation. With continued scaling of devices the surface proximity effect is becoming more important, but the annihilation and precipitation mechanisms are still unclear.

Ion implantation at high doses leads to amorphization of the implanted section. The behavior of native defects in the amorphous layer[25, 26] would be different from those in the crystalline phase[27]. This may, in turn, affect

the spatial distribution of defects. For instance, a difference in defect formation energy between amorphous and crystalline phases would alter the relative population of defects locally in the substrate. Given that single vacancies and interstitials are highly mobile even at room temperature, the existence of amorphous Si may affect significantly annihilation of defects[25] and subsequently their concentration distribution (during implantation and early stage of annealing, i.e., until amorphized layers are fully recrystallized by thermal annealing). However there is no clear description of defect behaviors at the vicinity of the a-c Si interface.

Using density functional theory calculations[28, 29, 30, 31], we have investigated the fundamental properties and dynamical behavior of vacancies, interstitials, and boron-interstitial complexes at the Si(001) surfaces, a-c Si interfaces, and Si/SiO_2 interfaces. This dissertation is organized as follows.

In chapter 2, we provide a brief overview of theoretical methods and techniques employed in this work. We begin with a brief description of the first principles computational methods based on density functional theory. Next we describe charge topology analysis based on QTAM theory, electron localization functions, methods for searching diffusion pathways, such as nudged elastic band method(NEB). In the last section we describe construction of realistic amorphous structures and crystalline-amorphous interfaces.

In chapter 3, we describe our findings on mechanisms of vacancy and interstitial interactions with clean and adsorbate-modified Si(001) surface.

We begin with description of structure of the stable mono-vacancies(MVs) at Si(001) surface and provide an explanation of MV stabilization. Then we describe the interaction of subsurface vacancies with the reconstructed Si(001) surface. We propose a mechanism of vacancy stabilization at subsurface layers. Along with the structure and energetics, we analyze bonding mechanisms of vacancies and interstitials based on electron density and electron localization function topologies. Next we compare the dynamics of vacancies at and near the Si(100) surface with that at the Si bulk. We show the diffusion pathways and barriers of vacancies on the surface and at the subsurface layers. We propose a new mechanism for monovacancy annihilation and single missing dimer creation. Then we consider the structure and energetics of neutral interstitials at subsurface layers. In the last section we describe our investigation into the effect of surface passivation on vacancy and interstitial annihilation on the Si(001) surface.

In chapter 4, we present the behavior of neutral vacancies and interstitials at amorphous-crystalline Si interface, and the formation of native defects in the amorphous Si. A continuous random network model is employed in the construction of a defect-free *a*-*c* interface structure. We also discuss the effect of the 'sponge-like' behavior of the amorphous phase toward native defects on ultrashallow junction formation in the fabrication of microelectronic devices.

In chapter 5, we present the behavior of native defects at Si/*a*-SiO_2 interface. First, we discuss in detail Si interstitial stabilization at interface and in *a*-SiO_2. Next, we propose a novel mechanism for interstitial migration

across the interface. In the last part of the chapter we consider stable vacancy structure at and near Si/SiO_2 interface. We also show that interface may serve as a limited sink for Si vacancies, leading to creation of steps.

In chapter 6, we present our findings on the behavior of Boron-Interstitial(BI) pair at Si/SiO_2 interface. First, we identify stable BI structures at the interface. Next we present diffusion of BI complexes along the interface and into the oxide layer, along with BI dissociation at the interface.

In chapter 7, we propose a method for energy corrections in the charged supercell calculations and apply this method to computations with charged interstitials and boron-interstitial complexes in Si.

In chapter 8, we summarize the major contributions of this work and suggestions for future studies.

Chapter 2

Theoretical Background

2.1 Density functional theory

To understand the native defects and dopants behavior in the complex systems we need to use precise, yet effective, computational techniques. It should be able to capture all intricate details of defect bonding and energetics in variety of environments and in the same time be capable of handling a few hundred of atoms. Total energy electronic structure calculations[32] based on the density functional theory (DFT)[33, 28, 29] are currently among the most successful and widely used approaches for prediction structural and interaction properties of many solid-state and molecular systems. The DFT replaces quantum-mechanical many-body problem of electrons moving in the field of atomic nuclei with that of finding the charge density distribution n(r) that minimizes the energy of the system. The foundation of DFT lies on the Hohenberg-Kohn theorems[28] that state i) the external potential is the unique functional

of n(r) and hence the ground state properties of the system (including the Hamiltonian) are fully determined by the ground state density, and ii) only the exact ground state density delivers the global minimum to the universal energy functional of the system. In Kohn and Sham approach[29], the insurmountably complex problem of deriving the energy functional of the system of interacting electrons was replaced with that for non-interacting electrons moving in the effective potential. The difference between kinetic energy of interacting and non-interacting electrons is represented by the functional of charge density called exchange-correlation energy (E_{xc}[n(r)]). This approach results in formulation of the set of equations, know as Kohn-Sham (KS) equations[29, 34]. The simplest approximation to E_{xc}[n(r)] is the local-density approximation (LDA)[29]. It assumes that E_{xc}[n(r)] depends only on the density at each point in space and independent of the density at other points. In our work we mostly use generalized-gradient approximation (GGA)[35, 36] to E_{xc}[n(r)] which is considered to be more precise compared to LDA. In this approximation E_{xc}[n(r)] is a function of the density and its gradient. The GGA increases the magnitude of the exchange energy, lowering the total energy of the system, and decreases the magnitude of the correlation energy. In order to reduce the problem of finding the total energy of an infinite system with an infinite number of electrons to the problem with the finite number of electrons moving in the periodic potential, the periodic cell approximation17 (the supercell) is used. The Bloch's theorem allows to expand electronic wave functions at each k-point in the Brillouin zone as series of plane waves. This expansion needs

to include only the plane waves with kinetic energy less then some particular cutoff energy. The KS equations are solved self-consistently for the ground state of the non-interacting electrons in effective potential[35, 37]. Only the outer-shell electrons are accounted for and core electrons are replaced with pseudo-potential. Special k-point sampling scheme proposed by Monkhorst and Pack[38], symmetry considerations and the electron smearing methods allow reduce the number of k-points in the Brillouine zone considerably. Ultrasoft Vaderbilt[39] pseudopotentials result in a smaller set of the plane waves needed for the accurate representation of the electronic wavefunctions. The atoms in the supercell are fully relaxed using conjugate gradient or quasi-Newton algorithm until all residual forces on the atoms become sufficiently small.

2.2 Charge density topology

We apply the quantum theory of atoms in molecules (QTAM)[40, 41, 42] to characterizing the bonding mechanism of defect sites. From an analysis of the topological properties of calculated electron densities, we could obtain some insights into the nature of bonding.

Along with a charge density ρ and its gradient $\nabla\rho$, the Laplacian $\nabla^2\rho$ provides physical and at the same time concise basis for classification of atomic interactions.

According to the quantum mechanical virial theorem for the stationary

state,

$$-L(r) = V(r) + 2T(r), \tag{2.1}$$

where

$$L(r) = -\frac{\hbar^2}{4m}\nabla^2\rho \tag{2.2}$$

is the Lagrangian density, and $V(r)$ and $T(r)$ are the constituent potential and kinetic energy densities, respectively. By definition, kinetic energy is positive everywhere and potential energy is negative everywhere. Thus the sign of $\nabla^2\rho$ shows the relative local excess of kinetic or potential energy density in a certain space region compared to their average virial ratio of two to one.

A typical sign of a closed shell bonding is the region of the positive sign of the Laplacian between two interacting atoms. It indicates a relatively large kinetic energy contribution and local charge depletion in this region of space. The regions of the dominance of the potential energy and the charge accumulation are separately localized near interacting atoms.

The negative sign of Laplacian indicates that energy of the system is lowered due to the local excess of potential energy. In this type of interaction we observe charge sharing between two nuclei, a characteristic of a covalent or a polar bond.

A charge density along the Atomic Interaction Line (AIL) between bonded atoms attains maximum with respect to any lateral displacement from the AIL. The negative sign of Laplacian indicates charge accumulation, hence the Valence Shell Charge Concentration (VSCC) regions can be defined as the

regions where $\nabla^2\rho < 0$. Local maxima of $-\nabla^2\rho$ close to or far from the AIL show correspondingly a bonded or non-bonded charge concentrations.

The Laplacian of ρ is calculated as the sum of the eigenvalues of the matrix of the second derivatives (Hessian) of ρ. For the plane-wave basis pseudopotential method the accuracy of the calculation of the laplacian largely depends on the size of the FFT mesh used for representation of the charge density. To circumvent the disadvantage of using plane-wave basis code for the charge topology analysis the values of the laplacian are interpolated between mesh points. To identify the number of Laplacian maxima of the defect structure and their relative position to the AIL we examine the surfaces with the constant value of $\nabla^2\rho$.

2.3 Electron localization function

One aspect that is not directly taken into account by the topology of the charge density is the influence on the bonding due to the Pauli's exclusion principle. Analysis of the charge density and its Laplacian alone can not explain the additional decrease in excess local kinetic energy due to formation of electron pairs. As a robust descriptor of chemical bonding that takes into account the role of Pauli's repulsion we have used the Electron Localization Function (ELF)[43, 44], as proposed by Becke and Edgecombe[45] and implemented in VASP. ELF represents the electron pair localization as a function of the conditional pair probability for the same spin electrons to be at same point normalized to the probability of finding an electron pair with the like-spin in

the uniform electron gas. The ELF is derived from Kohn-Sham orbitals ϕ_i, and is defined as

$$ELF = \frac{1}{1 + \left(\frac{D}{D_h}\right)^2}, \tag{2.3}$$

where

$$D = \sum_{j=1}^{N} |\nabla \phi_i|^2 - \frac{1}{4}\frac{|\nabla \rho|^2}{\rho} \tag{2.4}$$

is the leading term in Taylor expansion of the conditional pair probability. It can be interpreted as the excess local kinetic energy due to fermionic character of electrons. $D_h = \frac{3}{5}(3\pi^2)^{\frac{2}{3}}\rho^{\frac{5}{3}}$ can be interpreted as the local kinetic energy of homogeneous boson gas. Thus the ELF can assume the range between 0 and 1, where the $ELF = 1$ corresponds to perfect electron pair localization and the $ELF = 1/2$ corresponds to homogeneous electron gas-like pair probability.

2.4 Reaction paths

We calculate diffusion barriers and pathways using the nudged elastic band method (NEBM)31,32. The NEBM starts by setting a chain of geometries (replicas) [interpolated between two local minima]. A spring interaction between the adjacent images is added to the true ionic forces, thus mimicking an elastic band. Then, the projection ("nudging") of each force in the direction parallel and perpendicular to the path is performed and only the perpendicular component of the true ionic force and the parallel component of the spring force are added to the total force. While initial and final configurations are

kept fixed, the position of each intermediate image is adjusted to minimize the total force acting on the images. This allows to search for a minimum energy pathway between the two local minima without placing any constraint on the atomic motion and without any prior knowledge about a potential energy surface.

For the study of defect behavior at the amorphous/crystalline Si interface and Si/SiO2 interface, it is very important to construct realistic interface structures. We use a continuous random network model to generate the interface structures. The "bond-switching" method coupled with Keating-like interatomic potential[46] has been successfully employed in generating amorphous interface structures.

2.5 Construction of amorphous-crystalline interface structures

2.5.1 CRN model

Over the past twenty years, a lot of effort has been devoted to the understanding of the properties of amorphous semiconductors due to its potential applications. If we do not consider the dangling bonds, the structure of the amorphous semiconductors can be well represented by the continuous-random-network (CRN) model introduced by Zachaiasen [47] more than seventy years ago. As an amorphous structure of semiconductors (particularly, amorphous silicon and amorphous silicon dioxide) is the prerequisite to study defect-

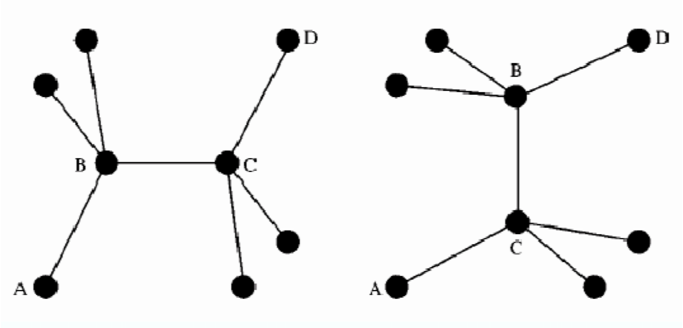

Figure 2.1: The schematic for the WWW bond transposition. Four atoms A, B, C, D are selected following the geometry shown left; two bond, AB and CD are then broken and atoms A and D are reassigned to C and B, respectively, creating two new bonds, AC and BD, resulting in the geometry shown right.

dopant dynamics in these materials, the generation of those structures via CRN has been a subject of intense investigation for many years. The first CRNs were hand built by Polk.[48] The most successful CRN generated by computer was the work from Wooten, Winer and Weaire[49] back in 1985. By employing a basic "bond switch" mechanism, they elegantly produced a perfect fourfold coordinated amorphous silicon/germanium structure in excellent agreement with experiments. Fig.2.1 (from [50]) shows a typical WWW bond switch mechanism. In 2000, Barkema and Mousseau[51] generated a CRN model of amorphous silicon with a size up to 4096 atoms by improving the WWW algorithm.

2.5.2 Interface structures: *a*-Si/*c*-Si and *a*-SiO_2/*c*-Si

[1] In order to study the point defects (vacancies and interstitials) behavior at the amorphous-crystalline silicon and a-SiO_2/c-Si interfaces, we developed our own CRN model for these structures. For the generation of amorphous silicon structure, we use the basic WWW bond switch mechanism with a Keating-like potential[46] for the energy calculations. The potential parameters are chosen to be the same as in Tu and Tersoff's[52] paper. To generate an amorphous silicon cell, we first put the silicon atoms randomly in a cubic box. The size of the box was chosen to make sure that the structure has the experimental amorphous silicon density. Then we assigned four "neighbors" for each atom. The choice of neighbors was based on the consideration that no three or four member rings are allowed and the nearest atoms not fully coordinated will be chosen as neighbors. The initial structure is highly "strained" since there are some unrealistic neighbor pairs. However, the strain is quickly released after the bond switches are started at 5000°K. The simulation is continued until the bond angle deviation is reduced to 12 degrees. This system is further annealed at 3000°K and it takes 300,000 more steps to get a structure with the same characteristics as the experimental a-silicon.

Figure 2.5.2 shows a 216 atom amorphous silicon cell generated by our CRN model. The radial distribution function (RDF) is shown in Fig 2.2 with comparison to the experimental results. The RDF is in excellent agreement with that from the Laaziri et. al.'s experiment[53]. The average bond angle

[1] Implementation of the CRN method and structure constructions reported in this section are performed by D. Yu and G.S Hwang

and bond angle deviation are 109.2° and 10.1° , also consistent with the experimental results[53], which are 109.3° and 9.6°, respectively.

For the structure generation of amorphous silicon dioxide, a similar procedure as that for *a*-silicon is applied. The Keating-like potential parameters are from Tu and Tersoff's paper[52]. For silicon dioxide system, there is another term in the total energy formula in addition to the strain energy. This term is called penalty energy. Although all the silicon and oxygen atoms are perfectly coordinated, it is possible that they may have more than four or two neighbors, respectively, within the second nearest neighbor separation. In such a case, there are strong repulsive interactions between these atoms and their unbonded neighbors. The penalty energy is thus added to penalize Si and O atoms with unbonded atoms within the second nearest neighbor separation. After the initial random positioning of the silicon and oxygen atoms in a cubic box and the assignment of neighbors, the system is annealed at 5000°K without penalty energy. After the system reaches equilibrium, annealing is continued at 3000°K with penalty energy turned on until the structure reaches a new equilibrium.

For the generation of amorphous-crystalline silicon interface structure, we take the following steps. First, we build a crystalline silicon structure. Then we randomize part of the system by bond switching at high temperature while fixing the rest. We continue to anneal the amorphous structure at 3000°K until the structure characteristics is consistent with that from experiments. Finally, the whole structure is relaxed. Fig. 2.5.2 shows the structure of an

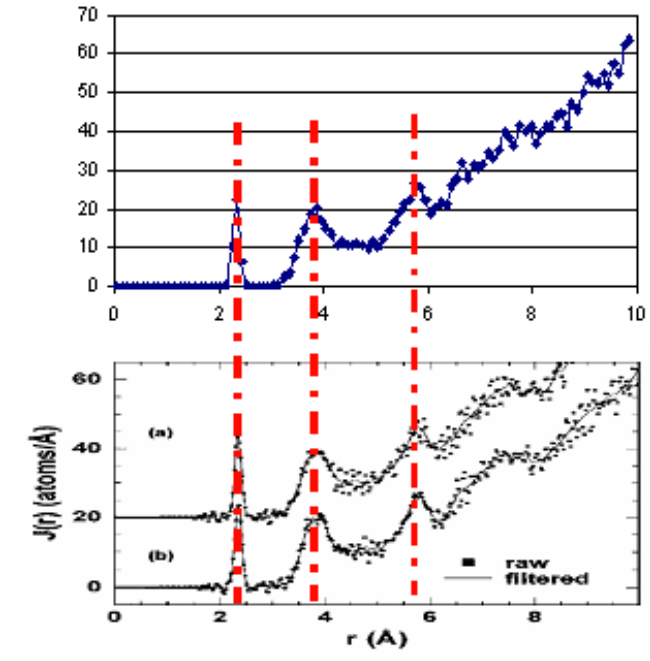

Figure 2.2: Comparison of the radial distribution function (RDF) of amorphous silicon generated by our CRN model with that from Laaziri et al's experiment.

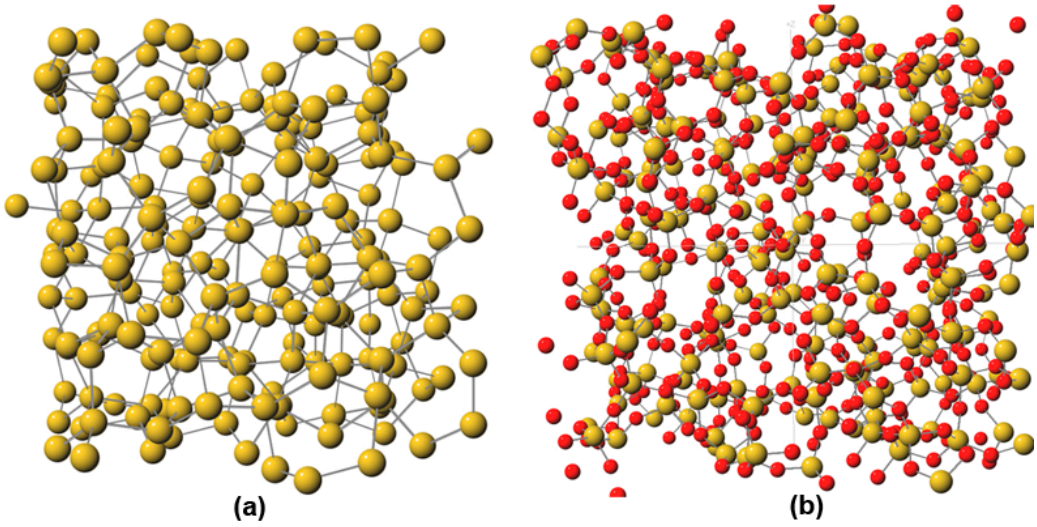

Figure 2.3: The ball-and-stick structure of (a) amorphous silicon and (b) amorphous SiO_2 generated by our CRN model. Light and big balls represent silicon atoms, dark and small balls oxygen atoms.

amorphous silicon dioxide cell. The generation of a-SiO_2/c-Si interface takes similar steps. The starting structure is a crystalline -crystalobalite on c-Si substrate. The SiO_2 is compressed in x- and y- directions and stretched in the z- direction in order to constrain the silica to match the crystalline silicon substrate in x- and y- directions while keeping the experimental amorphous SiO_2 density. Monte Carlo bond switching is performed in the oxide at a relative high temperature to amorphize the oxide and relax the large strain. We then perform unconstrained MC switching in the entire system to equilibrate it at a temperature of 1000°K. The a-Si/c-Si and a-SiO_2/c-Si interface structures are shown in Fig.5.1.

Chapter 3

Vacancies and Interstitials at the Si(001) Surface and Subsurface Layers

3.1 Introduction

The geometry, dynamics and electronic structure of intrinsic defects in semiconductors have been studied extensively because of their scientific interest and technological importance. The defects not only exhibit interesting physics of their own but also alter to a great extent the properties of materials. It is well known that the electrical and optical properties of semiconductors are governed by defects. In addition, surface chemical properties could be modified locally by surface and subsurface defects as well.

Many experimental and theoretical studies have been undertaken to understand the fundamental properties of vacancies and interstitials on the surface and in the bulk. However, little is known about the behavior of intrinsic defects at subsurface layers despite their importance particularly in better understanding their surface annihilation mechanisms. The Si (001) surface has been considered as an effective sink for bulk vacancies, but a detailed study of defect-surface interactions is still lacking. Surface annihilation of point defects is of great interest in ultrashallow junction formation for ever smaller semiconductor devices because it determines the concentration distribution of defects in the vicinity of the surface, which may, in turn, directly affect redistribution and electrical activation of injected dopant impurities.

We examine the interactions of neutral vacancies and interstitials with the clean Si (001) surface using density functional slab calculations. First, we calculate the structure, energetics, chemical bonding and diffusion dynamics of neutral vacancies on the clean surface and subsurface layers. Then, we look at the structure, energetics and chemical bonding of neutral interstitials on the clean surface and its subsurface layers.

All structures and energetics are calculated using the plane-wave-basis pseudopotential method within the generalized gradient approximation (GGA)[37] to density functional theory (DFT)[28, 29], as implemented in the Vienna Ab-initio Simulation Package (VASP)[30, 31]. We use Vanderbilt-type ultrasoft pseudopotentials[39]. A plane wave cutoff energy of 150 eV is used. We use

a $(2 \times 2 \times 1)$ mesh of k points in the scheme of Monkhorst-Pack[38] for the Brillouin zone (BZ) sampling.

The structures and relative formation energies of vacancies and interstitials at subsurface layers reported herein are calculated using the ten-atomic layer (4×4) slab. The slab is separated from its vertical periodic images by a vacuum space of 15 Å. We have checked carefully the convergence of structure and energetics with respect to the slab thickness and the surface unit cell size [by increasing the thickness to thirteen layers and the surface cell size to (4×6)]. The comparisons show there is no significant change in structural properties and energetics with the slab thickness. Regarding the cell size, the difference between the (4×6) and the (4×4) surface cell for the relative energies of the surface and the first subsurface vacancies is only about 0.05 eV (well within the error of a DFT calculation), but the structural properties remain virtually unchanged. The convergence test confirms that our (4×4) model surface with ten-atomic layers is sufficient. The dynamics of vacancies on the clean surface is investigated using a five-layer (4×6) slab. The bottom layer Si atoms are fixed at the bulk position and their dangling bonds are passivated by H atoms. The remaining Si layers are fully relaxed using conjugate gradient method to minimize the total energy until all residual forces on the atoms become smaller than 5×10^{-2} eV/Å. Electron wavefunction optimization at each ionic iteration is performed using the residual minimization method, direct inversion in the iterative subspace (RMM-DIIS)[54], with a convergence of 10^{-5} eV. We calculate diffusion barriers and pathways using the nudged

elastic band method (NEBM)[55]. We apply the quantum theory of "atoms in molecules" (QTAM)[40, 41, 42] to investigating the bonding mechanism of defective systems.

It is well known that the surface atoms of Si(001) are dimerized to reduce the surface energy. At low temperatures (≤ 200°K), the dimers appear to remain alternatively buckled along a dimer row, with antiphase correlation between dimer rows, leading to the well-ordered c(4×2) structure. The antiferromagnetic phase is widely accepted as the ground state of Si(001),[56] although a controversy still remains [57, 58, 59]. For the c(4×2) state, our DFT-GGA calculation yields the bond length of 2.31 Å and the buckling angle of 18.0°, in good agreement with previous DFT calculations[60, 61]. In the following sections, we will present the structure, energetics and bonding of neutral vacancies and interstitials on the clean Si(001) surface and its subsurface layers.

3.2 Structure, energetics and chemical bonding

Figure 3.1(a) shows the c(4×2) reconstructed surface. Here atoms 1-6 belong to surface layer, atoms 7-14 to the first subsurface layer, atoms 15-18 to the second sublayer, and atoms 19-21 to the third sublayer. In table 3.4 we summarize the change of total energy of the defective system with position of neutral vacancy. The total energy increases rapidly as the vacancy is moved into a

deeper subsurface layer, and it levels off beyond the fourth subsurface layer. The large energy difference of 2.4 eV between the surface and the fourth layer vacancies suggests that neutral vacancies could be trapped (annihilated) near the surface. First, we look at the structure and bonding of single vacancies on the Si(001)-c(4×2) surface. The up- and down-atom vacancies are constructed by removing the buckled up and down Si atoms, respectively. Figure 3.1(b) shows the relaxed configuration of the up-atom vacancy at the neutral state. For both the up- and down-atom vacancies, the second layer atoms [indicated as 12 and 13 in Fig 3.1(c)] around the vacancy undergo a significant inward relaxation to form the weak 12-13 bond with a distance of 2.82 Å. For the up-atom vacancy, the remaining atom of the 'defect' dimer moves upward by 0.39 Å. Thus, it appears that three consecutive dimers (including the defect dimer) are oriented in the same direction. The remaining atom is bonded to two subsurface atoms. The 2-8 and 2-9 back-bonds (2.34 Å) are noticeably shortened relative to the back-bonds (2.40 Å of an up atom on clean Si(001). The centers of the ELFs and the Laplacian critical points are slightly displaced from the straight 2-8 or 2-9 paths, indicating the back-bonds are strained to some extent. Now we can expect that the remaining atom has a lone pair of electrons. (Indeed, as shown in Fig. 3.1(b), the ELF isosurface of non-bonding localized electrons appears to be larger than that of an up-atom on the clean surface. Here, the value for all ELF isosurfaces is set to be 0.86.) The buckling of the next neighboring dimers gets weaker; that is, the buckling angle reduces from 18° to 14°. The buckling reduction leads to less charge transfer from the

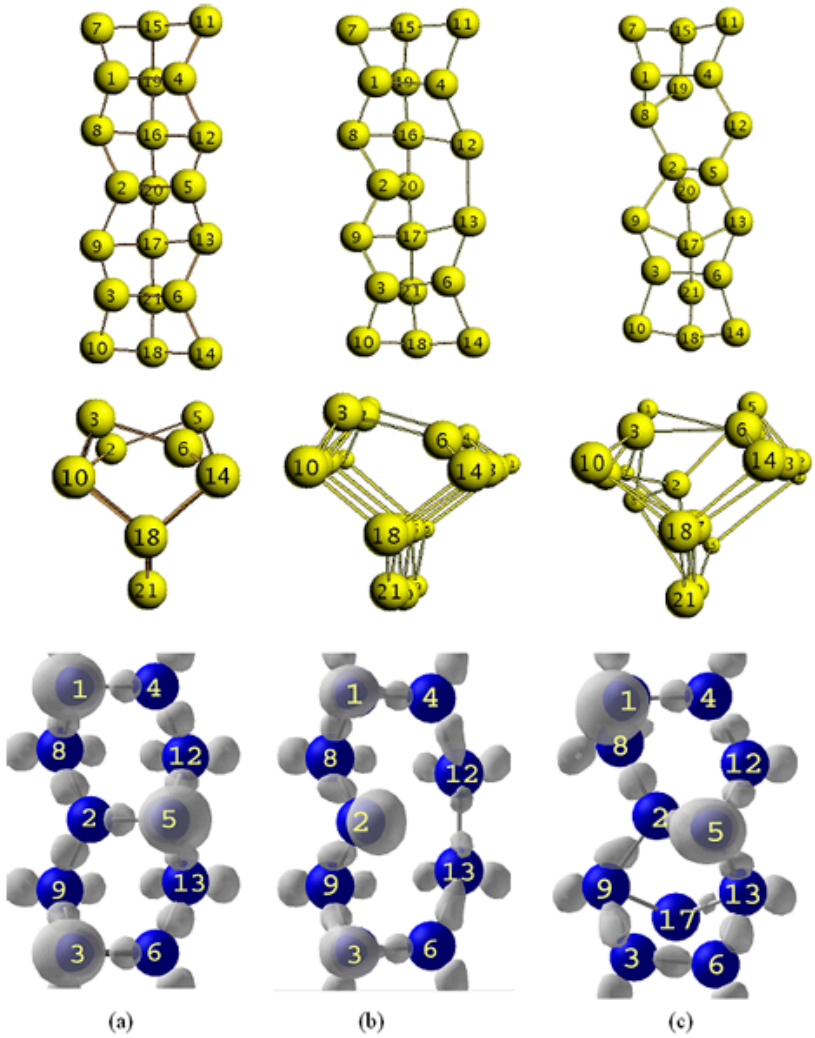

Figure 3.1: Top (top) and side (middle) view, together with ELF=0.86 isosurface maps (bottom), of surface and subsuface vacancy defect structures. (a) c(4 × 2) reconstructed clean Si(001) surface. (b)Up-atom surface vacancy: The atom 5 [from (a)] is removed. The bond lengths change to d_{12-13}=2.82 Å, d_{2-8}=d_{2-9}=2.34 Å, and d_{1-4}=d_{3-6}= 2.32 Å. (c) Second layer vacancy at the state 2A. The atom 16 removed, resulting in d_{2-20}=2.39 Å, d_{2-5}=2.36 Å, d_{2-8}=2.33 Å, d_{2-9}=2.47 Å.

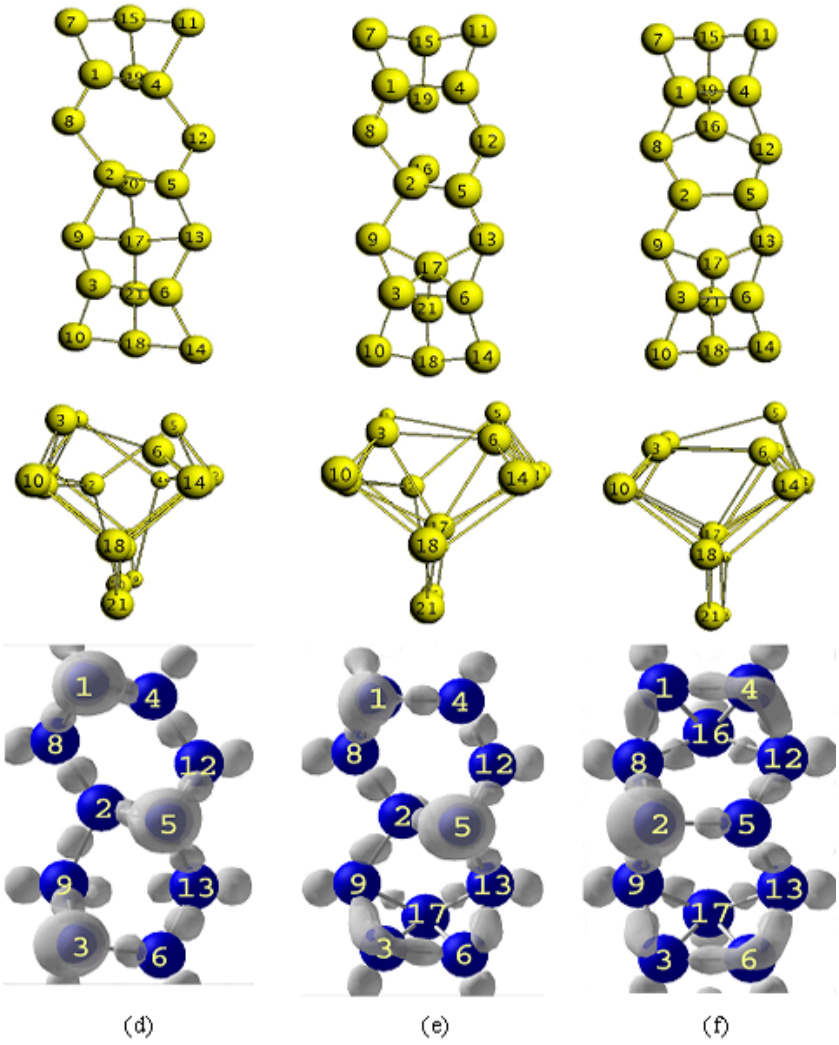

Figure 3.2: Top (top) and side (middle) view, together with ELF=0.86 isosurface maps (bottom), of surface and subsuface vacancy defect structures. (d) Second layer vacancy at the state 2B, with d_{19-20}=3.87 Å, d_{1-4}= d_{2-5}= 2.39 Å. (e)Third layer vacancy at the state 3A. d_{2-16}=2.43 Å, d_{1-8}=d_{4-12}=2.25 Å. (f) Third layer vacancy at the state 3B, with d_{1-4}= d_{3-6}= 2.30 Å and the distance between two fourth layer atoms (which were bonded to the removed atom 20) of 3.34 Å.

down atom to the up atom, which is well demonstrated by the reduced area of ELF isosurfaces for non-bonding localized electrons (on top of the up atoms). The down-atom vacancy formation is accompanied by the flipping of the next neighboring dimers, and thus five consecutive dimers (including the 'defect' dimer) are buckled to the same orientation. The down-atom vacancy turns out to be as stable as the up atom vacancy. (The energy difference between them is only 0.03 eV per (4×6) surface cell, well within the error of a DFT calculation). We also check the effect of next neighboring rows by comparing the energy difference between the up and down atom vacancies from the C(4×2) and the p(2×2) surface cells. The energy difference is estimated to be less than 0.02 eV, suggesting the influence of neighboring rows is insignificant. We also examine an outward relaxation of the second layer atoms, as suggested by Low et al.[62] However, this configuration turns out to be 0.13 eV (per (4×6) unit cell) less favorable than the up-atom vacancy.

We also investigated formation of di-vacancy(DV) on the Si(001)surface. The DV is constructed by removing the remaining atom of the 'defect' dimer. Compared to two MVs separated by two dimers, the DV formation lowers the total energy by 1.7 eV. The energy difference is quite similar to the energy gain by the vacancy-vacancy pairing in Si[63]. In fact, it is not surprising as the stabilization is mainly ascribed to the reduction of dangling bonds. This result clearly demonstrates that a DV is energetically far more stable than two separated MVs.

Second, we look at single vacancy formation at the first subsurface

layer[64] by removing the atom 8. Upon geometry optimization, the surface atom 1 slides down to the position of the removed atom 8, leading to a surface vacancy. This suggests that a vacancy at the first subsurface layer is unstable.

Third, we identify a very stable state [state 2A] of neutral vacancies at the second subsurface layer. The vacancy is created by removing the atom 16. Initially, four dangling bonds are created (at the atoms 8, 12, 19, and 20, around the vacancy). Upon geometry relaxation, as shown in Fig. 3.1(c), the surface atom 2 is greatly displaced downward. This leads to the formation of weak 2-20 and 8-19 bonds with distances of 2.39 Å and 2.54 Å, respectively. The 2-9 bond is significantly stretched to 2.47 Å (initially, 2.34 Å). As the atom 9 is dragged towards the atom 3, the up atom 3 is moved down and thus the 3-6 dimer is nearly symmetrized.

The atom 2 forms three covalent bonds with neighboring 5, 8 and 20 atoms that appear to exist nearly on the same plane, and also it barely exhibits a fourth close-shell interaction (with the atom 9). This suggests the surface atom 2 still retains the $sp2$ hybridization. It is likely that some charge is transferred from the down atom 2 to the up atom 5. The atom 12 shows a characteristic of sp2 hybridization; that is, it forms three covalent bonds that lie on a plane. A released electron from the atom 12 is delocalized, populating more negative charge at the adjacent dimers. The non-local effect has been found to be significant along a dimer row. Indeed, the sum of all bond angles of the up atom 5 is decreased from 281° to 264°, implying that the mixing ratio of s-orbital in the dangling bond is increased and the energy of the occupied

states is decreased.

The vacancy state is energetically only 0.2 eV (per (4×4) surface cell) less stable than the surface vacancy. We attribute the stabilization to i) reduction of dangling bonds in the subsurface layers and ii) delocalization of electrons on the local surface. We also identify a meta-stable vacancy [state 2B] at the second subsurface layer [Fig. 3.1(d)]. The 8-19 bond is now broken, and the weak 19-20 bond is formed by the Jahn-Teller distortion. The atoms 8 and 12 are three-coordinated, exhibiting sp2 hybridization. The released electrons from the atoms 8 and 12 are again delocalized on the local region, which in turn lowers the total energy.

The vacancy (state 2B) is about 0.2 eV less favorable than another (state 2A) second layer vacancy (vide supra). No bond breakage is involved in the transformation from the state 2B to the state 2A. Thus, the energy barrier is minimal *(vide infra)*. At elevated temperatures, we can therefore expect that the former can easily be converted to the latter.

Fourth, we look at vacancy formation at the third subsurface layer by removing the atom 20. The relaxed structure is shown in Fig. 3.2(e) [state 3A]. Initially, four dangling bonds are created [at the atoms 16, 17, and two other atoms at the fourth subsurface layer (not shown in Fig. 3.2(e)]. The surface atom 2 is significantly displaced downward to form the 2-16 bond (2.43 Å) while pushing the atom 16 down. This in turn leads to i) breakage of 12-16 and 8-16 bonds and ii) formation of bonds between 16 and fourth layer atoms (which were connected to the removed atom 20). As a result, the atoms 8 and

12 have a dangling bond, whereas the fourth layer atoms are four coordinated.

The atom 2 now shows a $sp3$ characteristic, rather than $sp2$. The atoms 8, 12, and 17 exhibit three normal covalent bonds that lie on a plane. The atom 17 also shows a fourth weak close-shell interaction (out of the plane, pointing to the center of the symmetrized 3-6 dimer.) It appears that released electrons from the atoms 8 and 12 are delocalized on the local surface. The 1-8 and 4-12 bond distances are about 2.25 Å, much shorter than 2.40 Å for corresponding back-bonds of an asymmetric dimer on the clean surface. The stronger bonding interactions are well demonstrated by ELF (Fig.3.2(e)) and charge and Laplacian density topology maps that exhibit more charge accumulation within the bonds.

The third layer vacancy turns out to be very stable; its formation energy is only 0.2 eV larger than the surface vacancy and about 2.2 eV smaller than the fifth layer vacancy (which assumes to be similar to a bulk vacancy).

We identify another stable configuration of neutral vacancies at the third layer (state 3B). Again, the atom 20 is removed. The relaxed structure is shown in Fig.3.2(f). In this case, the surface atom 2 is insignificantly displaced and retains the $sp2$ hybridization. The 8-16 and 12-16 bonds are preserved. The atoms 16 and 17 undergo significant outward relaxation. The two fourth layer atoms (which were bonded to the removed atom 20) form a weak bond with a distance of 3.34 Å (not shown in Fig. 3.2(d)). The 1-4 and 3-6 dimers are symmetrized.

The atoms 16 and 17 exhibit three normal covalent bonds that lie on

a plane, and also show a fourth weak close-shell interaction (out of the plane, pointing to the center of the symmetrized 1-4 and 3-6 dimers, respectively). The p-like interactions are likely to stabilize the defective system substantially. The formation energy of the third layer vacancy is about 1.55 eV lower than that of the fifth layer one (which exhibits large pairing Jahn-Teller distortions, like a typical bulk vacancy [65, 66, 67, 68, 69, 70, 71], resulting in two weak bonds between the atoms around the vacancy). However, the 3B vacancy state is energetically less favorable than the 3A state shown earlier (in which the dangling bonds at the fourth layer are terminated by the atom 13). The transformation from the state 3B to the state 3A involves breakage of 8-16 and 12-16 bonds, leading to a relatively large energy barrier of 0.6 eV *(vide infra)*.

Finally, we look at a neutral vacancy at the fourth and fifth subsurface layers. No significant changes arise in the surface structure, suggesting the vacancy-surface interaction is no longer significant. The fourth layer vacancy appears to be about 0.2 eV more stable than the fifth layer vacancy. The former exhibits the C_{2v}-point symmetry while the latter exhibits the D2d-point symmetry. Note that the symmetry of a neutral vacancy at the bulk lowers from Td to D_{2d} by the Jahn-Teller effect, although the change in formation energy is insignificant[70]. Here, the C_{2v} symmetry at the fourth layer is mainly due to the strain induced by surface reconstruction; that is, the fourth layer vacancy helps to relieve the sublayer strain to some extent, resulting in the formation energy lowering with respect to the fifth layer one.

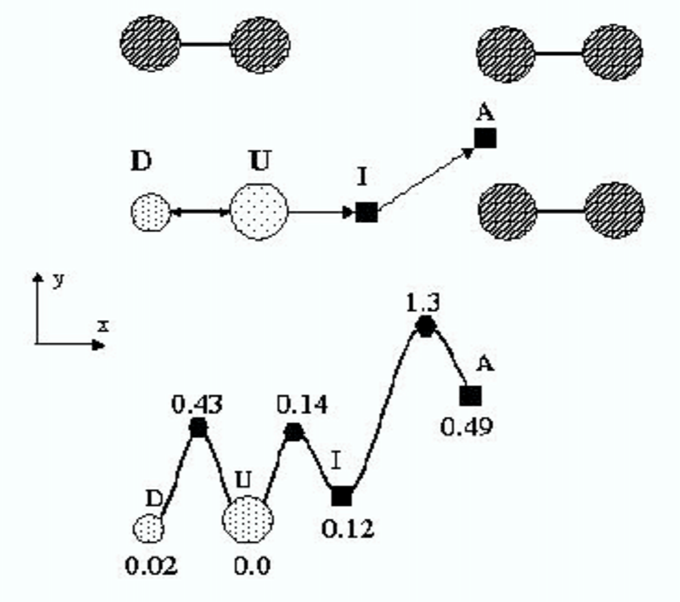

Figure 3.3: Surface monovacancy desorption. An arrow shows the direction of the 'defect-dimer' atom migration. D and U are the buckled-up and down sites at the 'defect-dimer', I is a (meta)stable intermediate position and A is an adatom site.

3.3 Diffusion dynamics

In this section, we present the diffusion pathways and barriers of a neutral vacancy on the clean surface and its subsurface layers.

As shown above, MVs can be created on the Si(001). However, it is still unclear how the MVs disappear almost completely, as shown in STM images.

Next, we discuss possible mechanisms for the MV disappearance.

i) Escape of the remaining atom from the 'defect' dimer': the remaining atom may leave very rapidly and form a 'stable' single missing-dimer va-

cancy, as proposed by Zhang and Metiu based on their classical SW potential calculations[72],

ii) Diffusion of mono-vacancies along a dimer row and formation of 'stable' missing-dimer vacancies (type-A defects) via vacancy-vacancy pairing: rapid surface diffusion of mono-vacancies may lead to type-A[60] defect creation.

iii) Rapid hopping of the remaining atom between two possible energy minima in the 'defect' dimer: suppose that the remaining atom undergoes hopping between the buckled-up and down sites very rapidly, the 'defect' dimer may look somewhat like a single missing-dimer vacancy (i.e., a time-averaged image).

iv) Diffusion of the surface monovacancy into the subsurface layers: a MV may be trapped in the subsurface layers.

First, we look at the escape of the remaining atom from the 'defect' dimer, leading to the creation of a DV and an adatom. Figure 3.3 shows a possible escape pathway from the up-atom position (indicated as U) to nearest 'stable' adatom site (A) through an intermediate local minimum site (I). First, the remaining atom is pulled along the x direction, leading to a local minimum state (I) with a return barrier of only 0.02 eV, (this state is probably not stable.) Then, we search a diffusion pathway from I to A (adatom site) using the NEBM method[55]. The escape requires overcoming a barrier of 1.18 eV. Thus, assuming steady state kinetics, the overall activation energy for the escape process is estimated to be 1.3 eV. The state A turns out to be energetically less favorable than the state U, resulting in a returning barrier of 0.8 eV which is in good agreement with 0.74 eV, as obtained by SW calculations[72]. Based

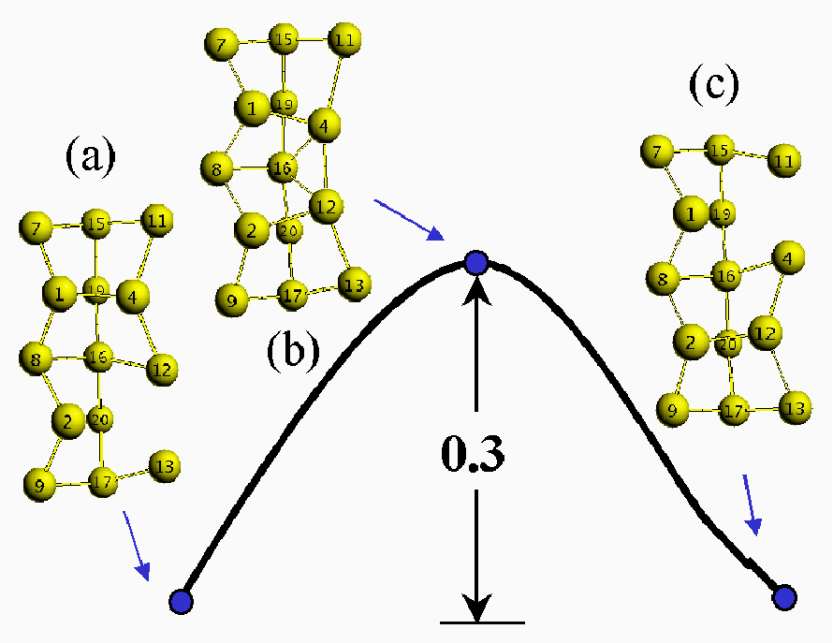

Figure 3.4: Pathway and energetics for neutral vacancy diffusion along the dimer row. (a) initial state (up-atom vacancy), (b) transition state, and (c) final state (down-atom vacancy).

on the calculated barrier of 1.3 eV, we estimate the mean time required for the atom escape from the 'defect' dimer. For a pre-exponential factor of 10^{13} sec^{-1}(Debye frequency), the escape rate is $k_e = 10^{13} exp(\frac{-1.3}{k_B T})$ sec^{-1}, where kB is the Boltzmann constant and T is the surface temperature. At room temperature, $k_e = 2.6 \cdot 10^{-10}$ sec^{-1}, i.e., the residence time is $\tau_e (= \frac{1}{k_e}) = 3.8 \cdot 10^9$ sec, far larger than the STM scanning time. This implies that an isolate MV can exist stably at room temperature, rather than liberating the remaining atom rapidly, in direct contradiction with a previous DV formation model proposed by Zhang et. al[72].

Next we examine MV diffusion along a dimer row using the NEBM

method. Figure 3.4 shows the initial, transition, and final state configurations of the diffusing MV between two adjacent vacancy sites. The vacancy diffusion involves a concerted motion of two surface atoms (1 and 2). In the transition state,(Fig. 3.4 (b)) the atom 2 moves outward to interact with the remaining atom 3 while the atom 1 moves downward to form a weak bond with the third layer atom 10. The diffusion barrier is calculated to be 0.4 eV. The low barrier indicates that surface MVs are highly mobile at elevated temperatures, which can in turn lead to DV creation by vacancy-vacancy pairing. Our calculation also shows there is no sizable barrier for the pairing. The total energy lowers as the vacancy-vacancy distance decreases. For instance, the total energy of two adjacent vacancies is 0.2 eV lower than that of two separated vacancies by two dimers. These results suggest that the vacancy-vacancy pairing may play a major role in creating missing-dimer vacancies.

We also look at vacancy hopping between the up- and down-atom site in a 'defect' dimer. In the calculation, we fix the x and y coordinates of the remaining atom at certain values and only allow the z coordinate to move. The rest of the atoms in the slab supercell are fully relaxed except the bottom Si layer and hydrogen atoms (used for the bottom layer passivation). The hopping barrier is calculated to be 0.3 eV. Suppose again the prefactor is 10^{13} sec^{-1}, the hopping rate is $10^{13} \cdot exp(\frac{-0.3}{k_B T})$ sec^{-1}. At room temperature, the corresponding residence time ($\tau_h = \frac{1}{k_h}$) becomes 10^{-13} sec, far smaller than the STM scanning time ($\approx 10^{-3}$ sec). This suggests that it may be hard to identify MVs, if any, at elevated temperatures. Since the surface diffusion is

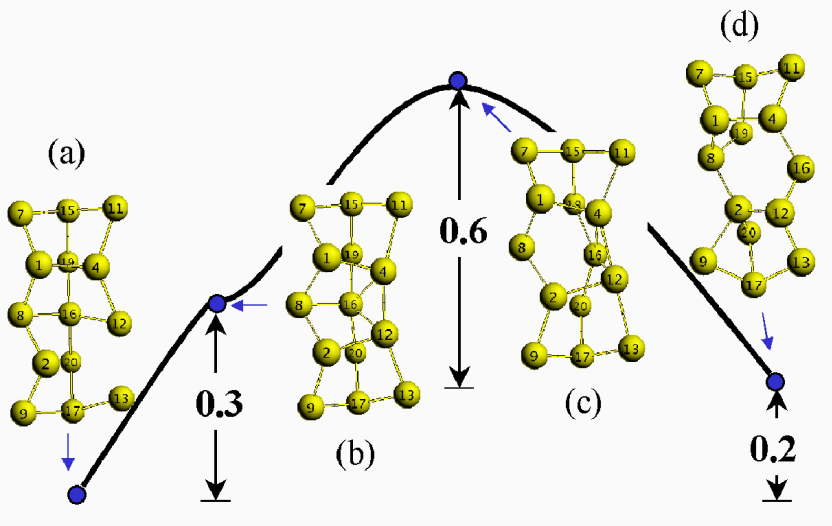

Figure 3.5: Pathway and energetics for neutral vacancy diffusion into the subsurface layer. (a) initial state (up-atom vacancy), (b) intermediate saddle point, (c) transition state, (d) final state (subsurface vacancy).

more facilitated (according to out calculation results), in fact, it is unlikely that a vacancy remains in the defect dimer and undergoes hopping between the up and down sites for a long time period.

Third, we calculate vacancy diffusion from the surface to the subsurface. The barrier is estimated to be 0.8 eV, with a return barrier of ≈ 0.6 eV. Figure 3.5 shows intermediate configurations of the diffusing vacancy along the diffusion pathway: i) the surface vacancy (a) starts moving along the (011) direction, ii) the vacancy passes through the saddle point (b) of diffusion along a dimer row (as shown earlier), iii) instead of hopping to the adjacent surface site, the vacancy continuously moves down to the subsurface, which involves a consorted motion of the atoms 2 and 12.

The atom 12 moves up to restore a dimer with the remaining atom 2

while the atom 2 sinks to form a bond with the atom 20. The transition-state configuration is displayed in Fig.3.5 (c). Since the diffusion will take place through the transition state of surface diffusion, it is likely that a surface vacancy mostly migrates to the adjacent surface site, rather than to the subsurface by overcoming an additional relatively large barrier of 0.5 eV. (Note that the barriers for vacancy diffusion along a dimer row and to the subsurface are 0.3 eV and 0.8 eV, respectively).

The complete energy diagram for vacancy diffusion up to the fourth subsurface layer is shown in Fig. 3.6. From the fourth to the third layer [state 3B], the diffusion barrier is estimated to be 0.13 eV. (The return barrier is 1.5 eV). The diffusion shows a similar feature to the bulk diffusion.

Vacancy diffusion from the state 3B to the state 3A at the third layer requires overcoming an energy barrier of 0.6 eV. There is relatively large return barrier of 1.3 eV from the state 3A to the state 3B. This suggests that at moderate temperatures vacancies in the neutral state can be trapped at the third subsurface layer [state 3A]. The surface atom 2 moves down and interacts with the atom 16. The atom 16 is dragged and pushed down to the position of the removed atom 20 and forms bonds with fourth layer atoms (which were originally connected to the atom 20). At the same time, the 16-8 and 16-12 bonds are broken, largely responsible for the relatively large diffusion barrier.

From the third layer site [state 3A] to the stable second layer site [state 2A], vacancy diffusion takes place through the meta-stable state [state 2B]. The barrier of 0.4 eV from 3A to 2B may be associated with the breakage of

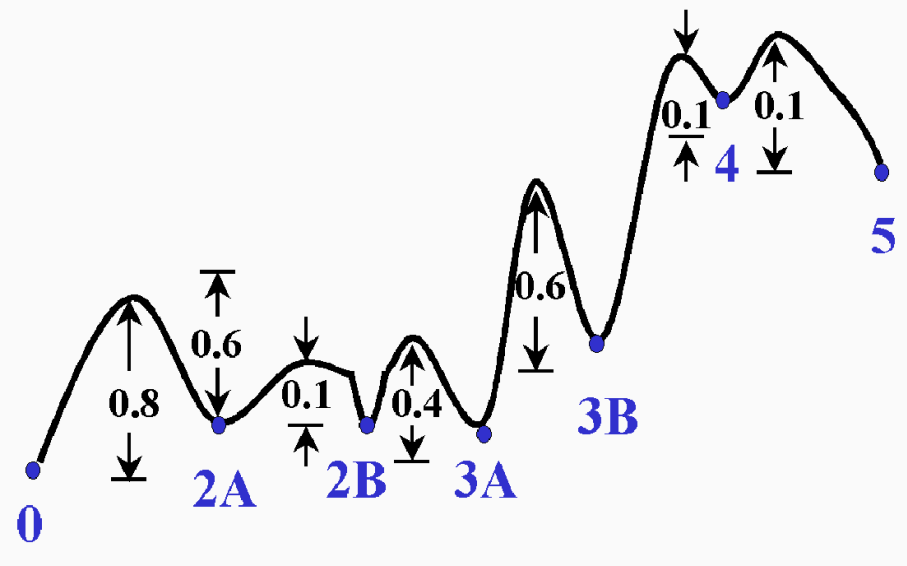

Figure 3.6: Energetics (in eV) along the diffusion pathway for a subsurface neutral vacancy. 0 denotes the surface vacancy, 2A and 2B indicate the second sublayer vacancy at the state A and B, respectively, 3A and 3B is the third sublayer vacancy at the A and B state, and 4 and 5 are the vacancy at the fourth and fifth subsurface layers.

the weak 16-19 bond. From the meta-stable to the stable state at the second layer, the vacancy can easily jump across with a very small barrier of 0.1 eV. (No bond breaking is associated with the diffusion.)

These results suggest that most neutral monovacancies may stay at the surface, rather than being trapped in the subsurface layers. Since the energy barriers for jumping across from the surface to the third layer are ¡ 1.0 eV and the formation energy differences are ¡ 0.2 eV, we expect that neutral vacancies will also be highly populated at the subsurface layers at elevated temperatures.

3.4 Surface chemistry effects on vacancy annihilation on Si(001)

We compare the structure and bonding of single vacancies on the reconstructed clean, H-terminated, and Cl-terminated Si(001) surfaces, as shown in Fig. 3.7. Here, we only report the up-atom vacancy (created by removing a buckled-up Si atom [Fig. 3.7(a)]) on the clean surface. The up-atom vacancy is energetically more stable than the down-atom vacancy, albeit to the slightest degree (0.02 eV per (4×6) surface cell)[73]. This is not surprising given the fact that the surface structure becomes energetically more stable as more dimers are alternatively buckled. (For the up- and down-atom vacancies, three and five consecutive dimers around the 'defect' dimer along a row are oriented along the same direction, respectively.) On the H- and Cl-terminated surfaces, the H and Cl atoms (initially on the removed Si atom) are allowed to move and terminate the dangling bond of the remaining Si atom of the defect-dimer.

In Fig. 3.8, we summarize the total energy variation in terms of the position of single vacancy for the clean, H-terminated, and Cl-terminated cases. For each surface system, the energy zero is taken to be the vacancy at the fifth subsurface layer (in which the surface effect is expected to be insignificant).

For all surfaces considered, the total energy increases rapidly as the single vacancy moves from the surface into a sub-surface layer, and it levels off beyond the fourth layer. The large energy difference of about 2.4 eV between the surface and the fifth layer vacancies suggests that neutral vacancies

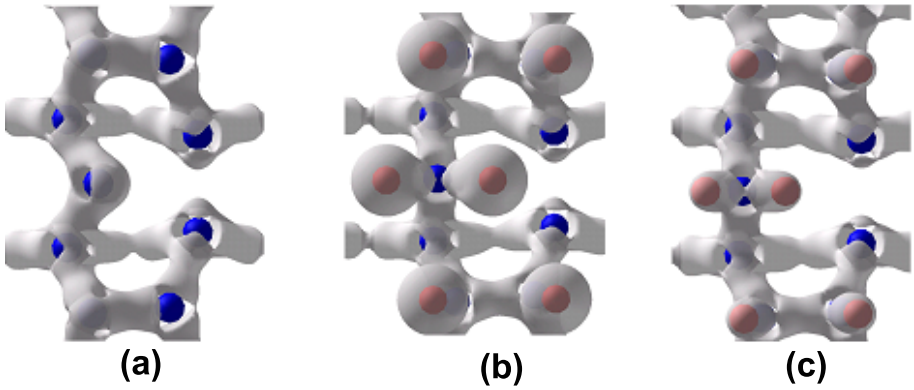

Figure 3.7: Charge density iso-surfaces of a) the clean, b) Cl-terminated, and c) H- terminated Si(001) surfaces, with a single vacancy at the surface. The back and greay balls represent the Si and Cl/H atoms, respectively.

can be effectively trapped (annihilated) at the surface, irrespective of surface passivation.

It is interesting to note the significant energy differences of 1.2-1.4 eV and 0.7-0.8 eV, respectively, at the second and third layer between the clean and passivated surfaces. To look at the origin of these energy differences, we calculate the total energy variation before atomic structure relaxation and find that i) the total energy changes significantly in the clean surface case while the energy variation is insignificant in the terminated cases and ii) the resulting energy differences between the clean and terminated cases are about the same as those after relaxation.

This suggests that the greater stabilization of vacancies in the clean surface case could primarily be attributed to the strong interaction of vacancies with surface dangling orbitals. Figure 3.9 shows the iso-surfaces of charge gain and loss associated with vacancy creation at the second layer for the clean and

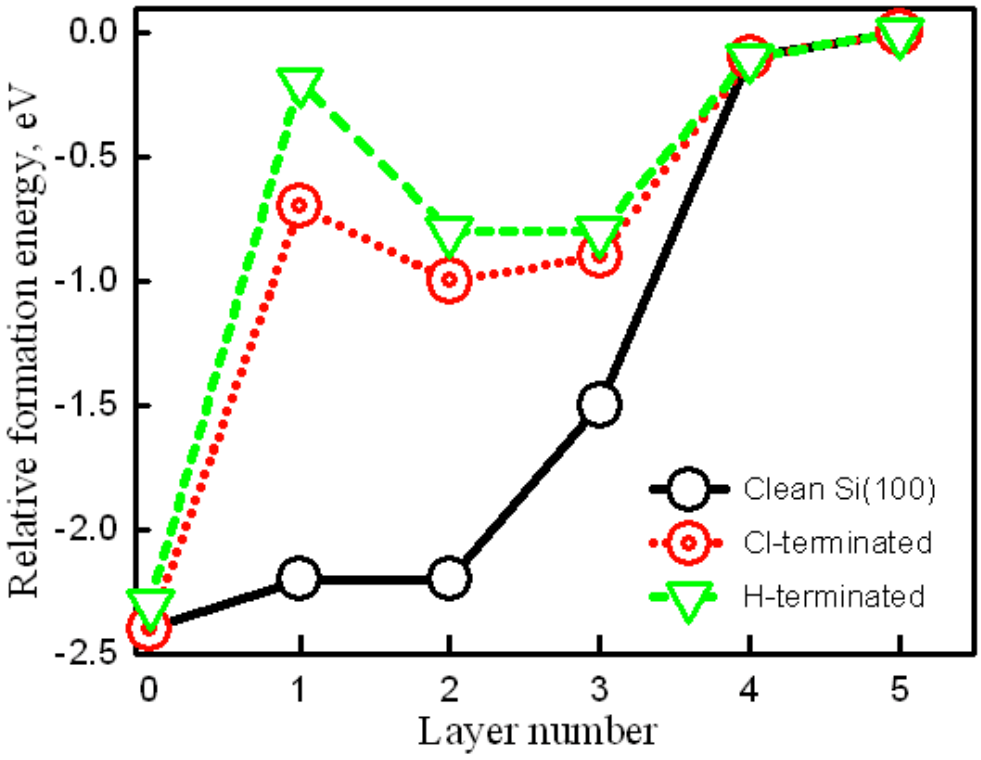

Figure 3.8: Variation of relative vacancy formation energy within the topmost five sub-surface layers for the clean, Cl-terminated, and H- terminated Si (001) surfaces. The energy zero is taken to be the vacancy at the fifth subsurface layer (in which the surface effect is expected to be insignificant).

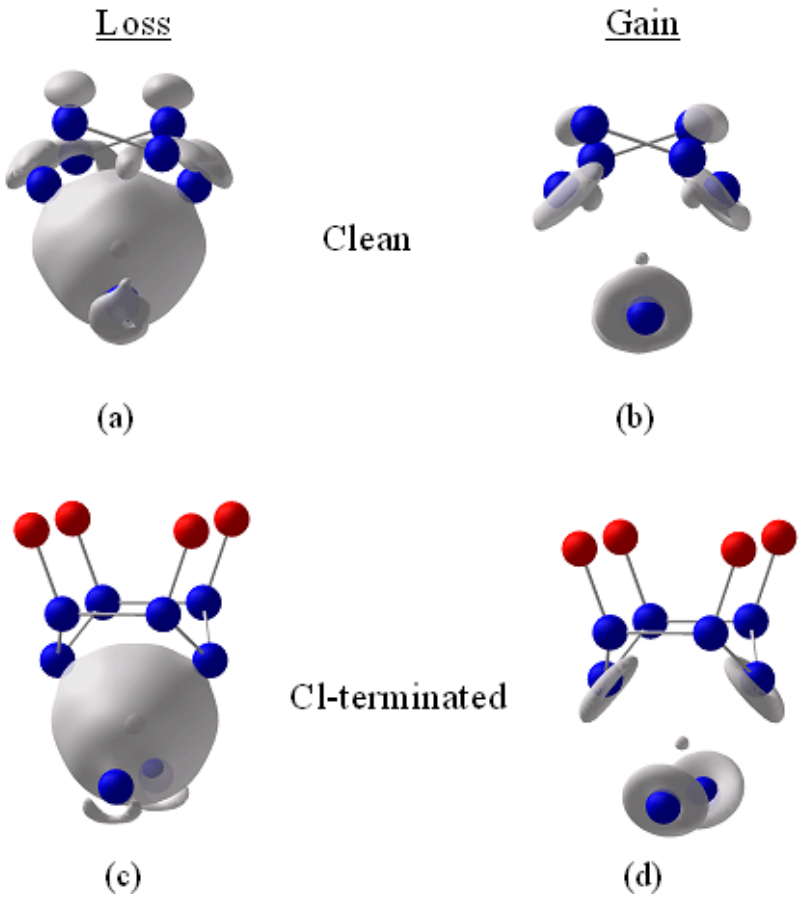

Figure 3.9: Charge density differences upon vacancy creation at the second subsurface layer. These plots are constructed by subtracting the charge densities after vacancy creation from those of vacancy-free ones, with no atomic displacement.

Layer number	2	3	5
Clean	-1.0	-0.6	0.0
H-terminated	0.1	0.0	0.0
C-terminated	0.1	-0.1	0.0

Table 3.1: Relative vacancy formation energies with respective to the fifth layer vacancy for the clean, H-terminated, and Cl-terminated Si(001) surfaces.

H-/Cl-terminated surface cases.

This clearly demonstrates that there is noticeable charge transfer between the vacancy site and the surface for the clean surface case. For both the clean and passivated cases, we can expect that the additional energy gain at the second and third layers (with respect to the fifth layer) mainly results from vacancy stabilization by i) rearrangement of surface atoms and/or ii) compressive-strain-assisted chemical pairing, possibly with a minor contribution of the relief of sublayer strain induced by surface reconstruction.

H- and Cl-terminated Si(001) surface. Since the surface dangling bonds are terminated (by either H or Cl atoms), no significant vacancy-surface interaction is expected. At the second and third layers, there exists compressive strain induced by (2×1) surface reconstruction. At these subsurface layers, therefore, vacancies can be stabilized by strain-assisted chemical pairing. Indeed, the second and third layer vacancies show significant inward relaxation. In addition, the sublayer strain can be relived by vacancy creation to some

Layer number		1	2	3	4
Clean	H	-0.4	-0.3	-0.2	0.0
	$(110)_{\perp}$	-1.3	-0.3	-0.1	-0.1
	$(110)_{\|\|}$	-3.0	-0.5	-0.1	-0.1
H-terminated	H	0.0	0.1	-0.1	0.0
	$(110)_{\|\|}$	-0.2	0.2	-0.1	-0.1
C-terminated	H	0.1	0.2	0.0	0.0
	$(110)_{\|\|}$	-0.4	0.2	-0.1	-0.1

Table 3.2: Relative interstitial formation energies with respective to the fifth layer hexagonal interstitial for the clean, H-terminated, and Cl-terminated Si(001) surfaces.

extent. We therefore suspect that the strain effect is mainly responsible for the stabilization of vacancies at the subsurface layers (when the surface is passivated). At the fourth and fifth subsurface layers, the strain effect becomes unimportant. We could also expect the surface-defect electrostatic interaction by adsorbate-induced polarization when vacancies remain near the surface, albeit it would be minimal.

3.5 Interstitials at the Si(001) surface and sub-surface layers

In table 3.5, we summarize the variation of relative interstitial formation energy within the topmost five subsurface layers for the clean and H-/Cl-terminated surface cases. For each surface system, the energy zero is taken to be the hexagonal (H) interstitial at the fifth sub-surface layer (where the surface effect is likely to be insignificant). Since surface reconstruction induces the anisotropy of the system, we identify two (110)-split states: i) parallel to the dimer row, i.e. along (011) direction, (indicated as $(110)_{||}$-split) and ii) perpendicular to the dimer row ($(110)_{\perp}$-split). Here, we only consider the H and (110)-split interstitials. Our calculations show that in bulk, the H and (110)-split interstitials are energetically almost equivalent, and they are about 0.29 eV more favorable than the T interstitials, in good agreement with previous DFT studies.

For all surfaces considered, there is a significant energy gain (of ¿ 2.5 eV) when interstitials are placed on the surface, relative to the fifth layer interstitials. This indicates that interstitials can be effectively trapped (annihilated) at the surface. While the interstitial stabilization at the surface is rather insensitive to the surface chemistry, the stability of subsurface interstitials is strongly influenced by the surface passivation. For the clean surface, the energy gains of 3.0 eV and 0.5 eV at the second and third layers, respectively, with respect to the fifth layer is apparently attributed to strong interstitial-

surface interactions, which not arise in the H- and Cl-terminated cases. Next, we discuss the behavior of interstitials at the subsurface layers.

3.5.1 Clean Si(001) surface

At the first sub-surface layer, the (110)-split interstitial appears to be unstable due to strain induced by surface reconstruction. Upon geometry relaxation, with an initial position at the (110)-split site, the interstitial slides to the H site between the first and second layers. At the second layer, the $(110)_{||}$-split interstitial turns out to be very stable. It is only 0.2 eV less favorable than the most stable adatom and 1.0 eV more stable than the H-interstitial in between the first and second layers. For the $(110)_{||}$-split interstitial, two adjacent dimers, 1-4 and 2-5, are symmetrized [Fig. 3.10].

Given such low formation energy, we expect that a large fraction of neutral interstitials could remain at the second subsurface layer as well.

At the third layer, the $(110)_{\perp}$-split interstitial appears to be most favorable, about 0.8 eV more stable than the H interstitial (staying at between the second and third layers). As shown in Fig. 5 (c), two Si atoms, 20 and 0 (inserted interstitial), share a lattice site while interacting with the second layer atoms, 8, 9, 12 and 13. The 16-20 and 17-20 bonds are broken and the atoms 16 and 17 undergo an outward relaxation. They are stabilized by interacting with the symmetrized dimers 1-4 and 3-6, respectively.

At the third and fourth layers, the surface effect diminishes substantially. The difference in the relative formation energy between the (110)-split and the H interstitial reduces to 0.2 eV and 0.05 eV at the third and fourth layer, respectively. The overall formation energies are very close to those at the bulk.

3.5.2 H- and Cl-terminated Si(001) surface

The total energy varies insignificantly at the sub-surface layers. The small fluctuation would be attributed to the variation of sublayer strain. At the first layer, in contrast to the clean surface, interstitials can remain stable at the $(110)_{\perp}$ state, but there is no noticeable reduction in formation energy compared to the fifth-layer interstitials. At the second layer, the $(110)_{||}$-split interstitial turns out to be most stable, with an energy gain of about 0.2-0.4 eV with respect to the fifth layer. At the third layer, the $(110)_{\perp}$-split interstitial appears to be favorable. This shows the stability of interstitials is mainly governed by sub-layer strain. Overall, the interaction of interstitials with the terminated surfaces is much weaker than with the clean surface, indicating that the terminated surfaces are not as effective as the clean surface for surface annihilation of interstitials.

3.6 Conclusions

The structure, energetics, and bonding of neutral vacancies and interstitials on the clean Si(001) surface and its subsurface layers are examined using first principles quantum mechanics calculations [density functional theory and quantum theory of "atoms in molecules "]. We also present the diffusion pathways and barriers of vacancies at the vicinity of the surface.

We find that the formation energy of vacancies (interstitials) at the surface is about 2.5 eV (3.2 eV) lower than that at the fifth subsurface layer in which the intrinsic defects show a similar characteristic to the bulk ones. It appears that both vacancies and interstitials at the neutral state are unstable at the first subsurface layer such that they migrate to either the surface or the second subsurface layer immediately. We identify the very stable states of vacancies at the second and third subsurface layers, with the formation energy of only 0.2 eV greater than the surface one.

Interstitials are also found to exist very stably at the second and third subsurface layers, with the formation energies of about 2.9 eV and 1.2 eV lower than the fifth layer one, respectively. Beyond the third layer, the surface proximity effect dwindles rapidly. The significant stabilization at the subsurface layers is mainly attributed to i) the reduction of dangling bonds in the subsurface layers as a result of rearrangement of surface atoms and ii) the delocalization of electrons on the local surface. It is likely that the strain induced by surface reconstruction plays a minor role in determining the relative stability of defects.

Our calculations also predict that the barriers for vacancy diffusion across the surface and subsurface layers are less than 0.4 eV and 0.8 eV, respectively. This suggests that neutral vacancies can easily jump across in the vicinity of the surface at elevated temperatures. Given the relatively small difference in formation energy between the surface and the subsurface layers, we expect that a large fraction of neutral vacancies and interstitials would remain within the third subsurface layers.

In this study, we only consider intrinsic defects at the charge neutral state. We suspect the behaviors of charged defects would be different from the neutral ones.

We also present the effect of surface passivation with H and Cl atoms on the annihilation of neutral vacancies and interstitials at the Si(001) surface. We find that surface passivation does not alter the energy gain of surface defects relative to bulk ones, but it greatly affects the stability of defects within the topmost three sub-surface layers. For a single vacancy, compared to the fifth layer one, the formation energy reduces by 2.2 (1.5) eV and 0.8-1.0 (0.8-0.9) eV at the second (third) sub-surface layer in the clean and terminated-surface cases, respectively. For the most-stable interstitial state each layer, compared to the fifth layer one, the formation energy changes by -3.1 (-0.6) eV and -0.3-0.5 (+0.1) eV at the second (third) sub-surface layer in the clean and terminated-surface cases, respectively. This stability difference at the sub-surface layers implies that the terminated surfaces are not as effective as the clean surface for the surface annihilation of vacancies and interstitials. We

expect that the detailed understanding of defect-surface interactions will be useful to develop a predictive model to simulate highly doped ultra-shallow junction formation required for nanometer scale electronic devices.

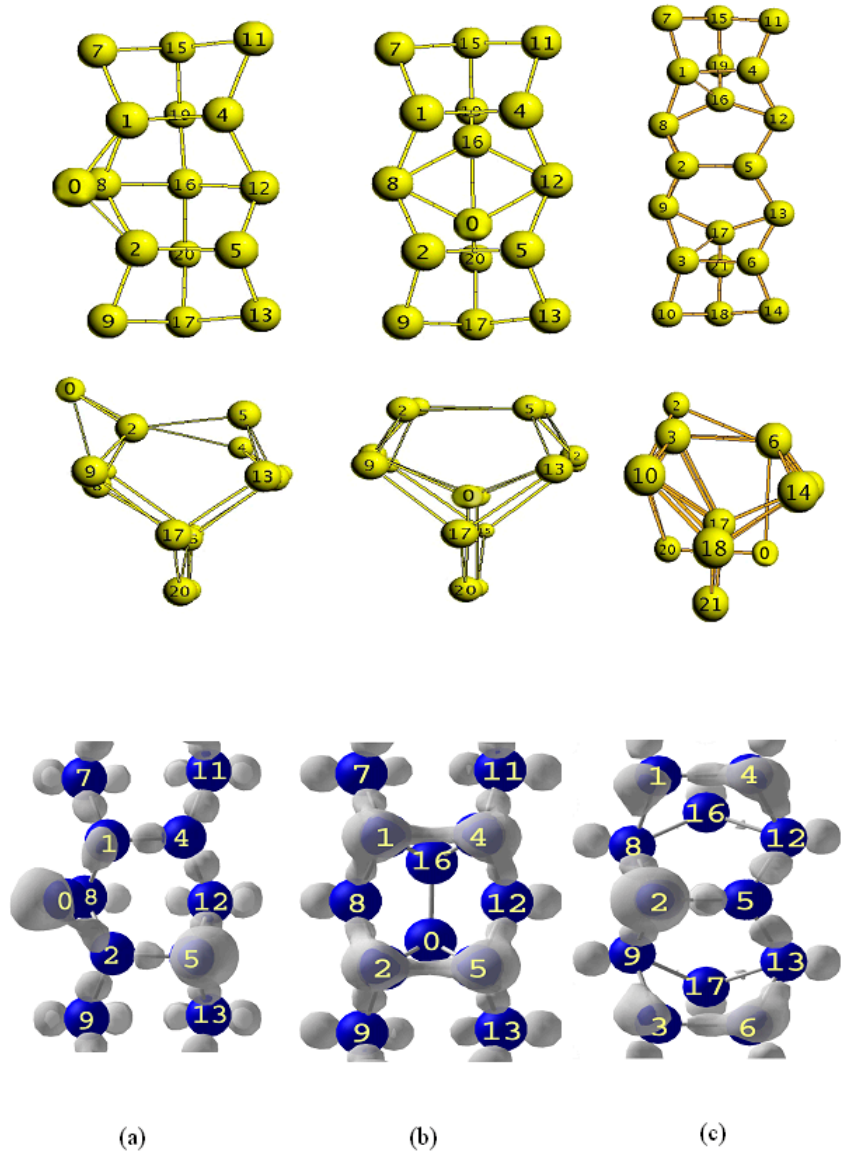

Figure 3.10: Top (top) and side (middle) view, together with ELF=0.86 isosurface maps (bottom), of adatom and sublayer interstitial defect structures. (a) adatom, indicated as 0. d_{0-1}=d_{0-2}= 2.40 Å. (b) $(110)_{||}$-split interstitial at the first sublayer. d_{0-16}=2.39 Å, d_{1-4}= d_{2-5} =2.45 Å, d_{1-16}= d_{0-5}=2.50 Å, d_{16-4}= d_{0-2}=2.48 Å. (c) $(110)_{\perp}$ -split interstitial at the second sublayer. d_{0-20}=2.84 Å, d_{1-4}= d_{3-6}=2.38 Å, d_{0-9}= d_{0-8}=2.52 Å.

Chapter 4

Silicon Interstitials at c-Si/a-Si Interface

4.1 Introduction

[1] Fabrication of forthcoming nanometer scale electronic devices faces many difficulties including formation of extremely shallow and highly doped junctions [1]. Currently, ultra-low-energy ion implantation followed by high-temperature thermal annealing is mostly used to fabricate such ultrashallow junctions. In this process, a great challenge lies in achieving precise control of redistribution and electrical activation of dopant impurities. Thus, many experimental and theoretical studies have been performed to elucidate underlying mechanisms of the Transient Enhanced Diffusion (TED) of dopant impurities during

[1]Results presented in this chapter are after "Origin of vacancy and interstitial stabilization at the amorphous-crystalline Si interface" by S. Harrison, T. Kirichenko, D. Yu., T. Edgar, G. S. Hwang and S.K. Banerjee, J. Appl. Phys., 96 (2004).

implantation and post-implantation annealing [74, 24, 63, 75, 3, 76, 77] and activation/deactivation [78, 79, 80, 81, 82, 83, 10]. These recent studies suggest that native defects (such as vacancies and interstitials) created during implantation are mainly responsible for the TED, and also greatly influence electrical activation/deactivation. It is therefore necessary to develop a detailed understanding of defect diffusion and annihilation behavior.

Ion implantation at high doses may lead to amorphization of the implanted section. Behavior of native defects in amorphous regions would be different from that in crystalline regions. This could in turn affect the density and spatial distribution of defects. For instance, if there is a difference in formation energy between the amorphous and crystalline regions [83], the relative density of interstitials and vacancies will vary with the phase. Since single vacancies and interstitials are highly mobile even at room temperature [10], their clustering and annihilation dynamics could greatly be affected by substrate amorphization (during implantation and early stage of thermal annealing where the amorphous region is not fully recrystallized). Despite technological importance of defect dynamics in the vicinity of the amorphous-crystalline (*a-c*) Si interface, there is still, to our best knowledge, no clear description available of this defect behavior.

In this study, we examine the relative stability of neutral vacancies and interstitials in the vicinity of the *a-c* Si interface using density functional theory slab calculations. We also discuss the origin of defect stabilization near the *a-c* interface. This study provides valuable insight into the clustering and an-

nihilation of vacancies and interstitials in the presence of amorphous volumes. This fundamental understanding and data will be very useful in developing a comprehensive kinetic model for ultrashallow pn junction formation.

We use a continuous random network (CRN) [84, 52, 46] model for an amorphous-crystalline Si structure. Starting with a periodic crystalline Si structure (which contains 192 atoms with a fixed lattice constant of 5.431 Å), the amorphous layer is generated via a large number of bond transpositions while the crystalline section is fixed. First, at a high temperature of 5000^0K, the amorphous layer is randomized. Then, the whole system is relaxed at 2000K via a sequence of bond switching (which is performed using the Metropolis Monte Carlo method based on energetics from the Keating-like potential of Si). The CRN approach has been proven to be reliable in constructing defect-free disordered structures. We used this approach to generate an amorphous Si structure which possesses an average bond length of 2.34 Å, an average bond angle of 109^0, and bond angle deviation of 10^0. Thus calculated structural factors are in excellent agreement with past experimental and theoretical results [53].

Figure 1 shows a ball-and-stick illustration of a defect-free CRN structure of amorphous-crystalline Si employed in this study, together with the strain energy of each Si atom. This result shows that this Si structure is most strained at the *a*-*c* interface. The strain decreases rapidly in the crystalline layer while decreasing rather slowly in the amorphous layer. All geometric structures and relative formation energies of vacancies and intersti-

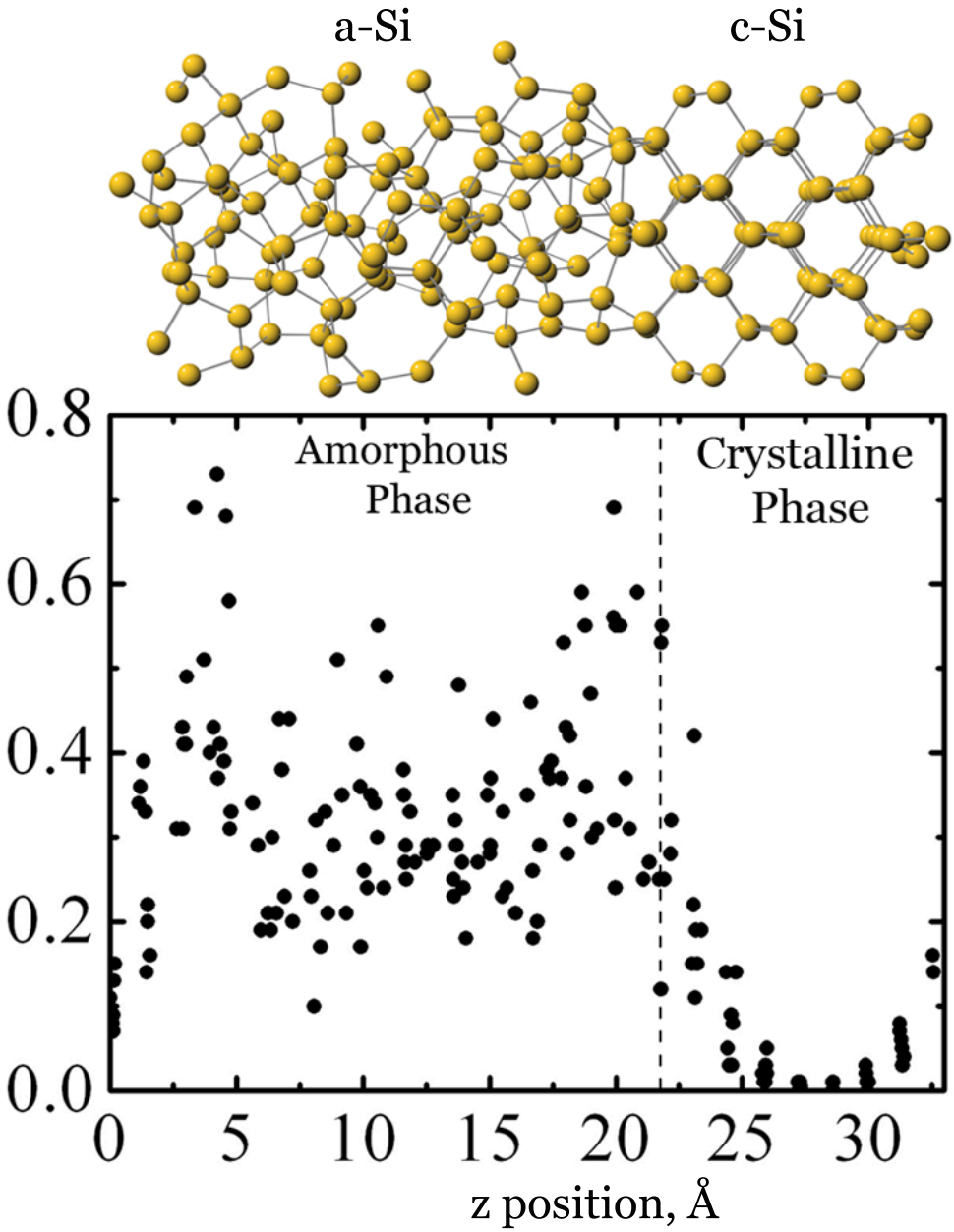

Figure 4.1: The *a-c* structure is depicted in (a) along with (b) the plot of strain energy of silicon atoms in the structure versus x-position.

tials are calculated using density functional theory (DFT). A plane-wave-basis pseudopotential method within the Generalized Gradient Approximation (GGA), [34, 37] is used, as implemented in the Vienna Ab-initio Simulation Package (VASP) [30, 31]. We use Vanderbilt-type ultrasoft pseudopotentials [85] and a plane wave expansion with a cutoff energy of 112.9 eV. For DFT calculations, the lattice constant was rescaled to the optimal value of 5.457 Å. All atoms were fully relaxed using the conjugate gradient method until all residual forces on constituent atoms become smaller than 5×10^{-2} eV/Å. One k-point (at Gamma) is used for the Brillouin zone sampling for the results we present. We performed several additional calculations of interstitial and vacancy structures with a denser $2 \times 2 \times 1$ k-point Monkhorst Pack mesh [38] to verify that Gamma point sampling is sufficient to support our observations. We analyze bonding mechanisms using the Electron Localization Function (ELF) as proposed by Becke and Edgecombe [45].

4.2 Silicon vacancies at *a-c* interface

Figure 2(a) shows a variation in the relative formation energy of single vacancy created at various locations in the *a-c* Si supercell described earlier. Here, the energy zero is taken to be the most stable vacancy in the supercell. The most stable vacancies are found near the *a-c* interface, with about a 3-4 Å shift toward the amorphous part. The formation energy decreases substantially when a vacancy moves from the crystalline region to the amorphous side. This result clearly demonstrates that vacancies prefer to reside on the amorphous side of

the *a*-*c* interface.

A comparison of Fig. 1(b) and Fig. 2(a) demonstrates there is a correlation between vacancy stability and strain field in the *a*-*c* Si system. In a strained region, vacancy formation can lead to local strain relief by allowing neighboring lattice atoms to relax. It is clear that the energy gain by strain relief is directly related to the initial strain of the removed atom and its neighbors. As demonstrated by the comparison of Figs. 1(b) and 2(a), an increase in local strain can facilitate vacancy creation. This suggests that vacancies will have a greater density in a more strained region.

While local strain relief is directly responsible for vacancy stabilization, it is not clear whether the strain relief is mainly from the relaxation of next neighbors or other lattice atoms further away from the vacancy site. To determine the relative contribution of neighboring lattice atoms to the strain relief, we computed the relative vacancy formation energies by allowing only the immediate neighbors (i.e., first shell atoms) of the vacancy to relax. Figure 2(b) depicts the relative formation energies of these partially relaxed vacancies at various positions in the *a*-*c* Si system. The overall formation energy variation is similar to the fully relaxed case. However, the energy decrease is not nearly as pronounced as when the vacancy was allowed to fully relax.

Figure 2(c) presents the energy difference between the energies presented in Figs. 2(a) and 2(b). This comparison clearly indicates that the first shell relaxation is only partially responsible for the vacancy stability. That is, the relaxation of lattice atoms beyond the immediate neighbors of the va-

cancy can provide a substantial amount of strain relief. Figure 3 shows the averaged displacements of first, second, and third shell atoms of single vacancy at various locations as indicated. This clearly illustrates there is significant lattice atom relaxation beyond the first shell. As a consequence, the relative vacancy formation energy is widely scattered even in the crystalline region as it is strongly influenced by the relaxation of strained atoms near the *a-c* interface. The long-range strain effect could lead to enhancement of vacancy trapping at the interface. While strain relief plays a dominant role in vacancy stabilization in a highly strained *a-c* Si system, the chemical bonding of under-coordinated first shell lattice atoms can also provide additional stabilization. For a neutral vacancy in crystalline Si, the first shell atoms commonly undergo a symmetric lowering Jahn-Teller distortion [71, 67] to form two weak chemical bonds. Thus, the vacancy symmetry lowers from T^d to D^{2d}. In the highly strained Si system, however, two main types of pairing are exhibited: i) under compressive strain, the two pairs of dangling bonds form weak chemical bonds, thereby effectively annihilating the vacancy and ii) under tensile strain, one pair of dangling bonds forms a weak bond while the other pair of dangling bonds remains largely separated. In areas of high tensile strain, bond transpositions also occur during relaxation, but these transpositions still leave one weak chemical bond and a pair of dangling bonds. We expect that at elevated temperatures dangling bonds will migrate and annihilate each other in the amorphous region.

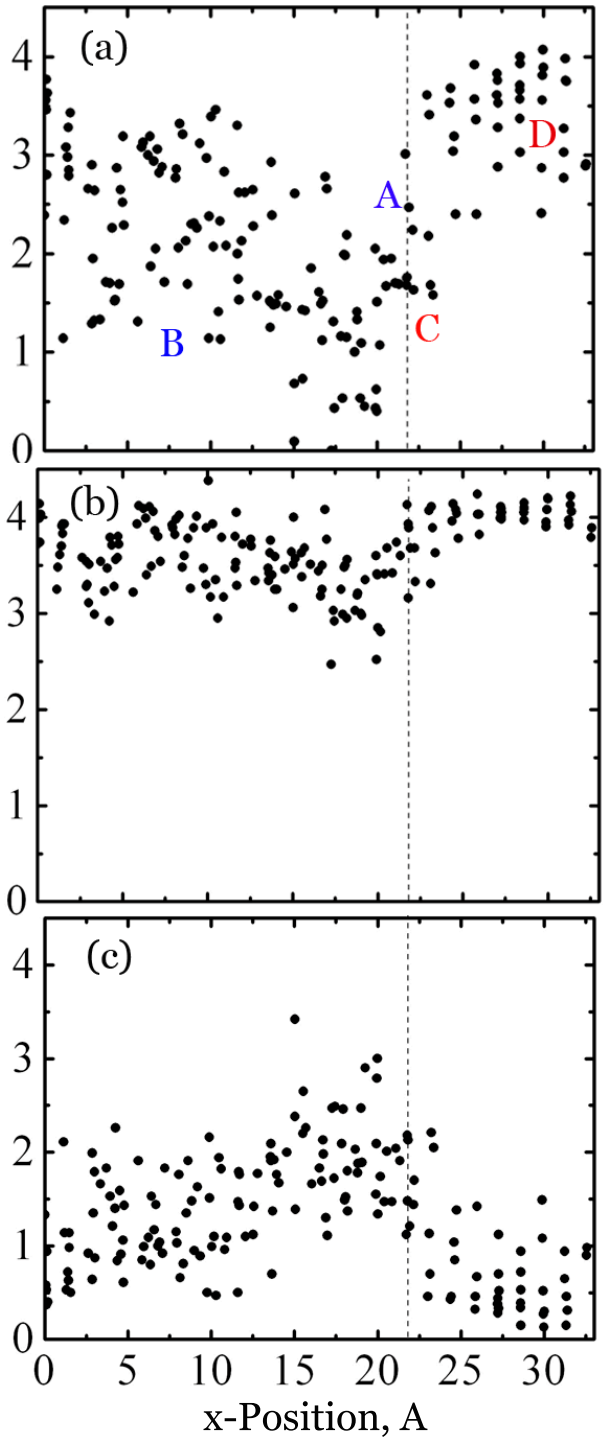

Figure 4.2: Completely relaxed vacancy energy versus x-position is shown in the top plot (a). In the lower plots, (b) partially relaxed vacancy energy versus x-position, as well as (c) energy difference between the vacancy energies in plots (a) and (b) are displayed.

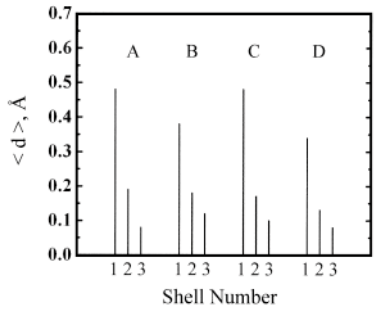

Figure 4.3: The average atomic displacement ($< \bar{d} >$) of each of the first three neighboring shells of vacancies A, B, C, and D are shown. Vacancies A, B, C, and D are labeled in Fig. 4.2(a).

4.3 Silicon interstitials at *a-c* interface

Figure 4 displays the relative energy variation of single Si interstitial inserted at various locations within the previously described *a-c* supercell. Here, the energy zero is taken to be the most stable interstitial in the supercell. The most stable interstitials are also found near the interface, about 3 Å into the amorphous region. Similar to the vacancy case, the total energy decreases considerably as a Si interstitial moves from the crystalline region to the amorphous region, and it reaches a minimum on the amorphous side of the interface. This result clearly demonstrates that interstitials prefer to reside in the amorphous region. A comparison of Fig. 1(b) and Fig. 4 also reveals that there is a strong correlation between interstitial stability and local strain. The most stable interstitials are created near the *a-c* interface, which is the most strained location in the Si structure. While substrate strain clearly correlates with interstitial stability, it is not apparent that strain relief is the only source of

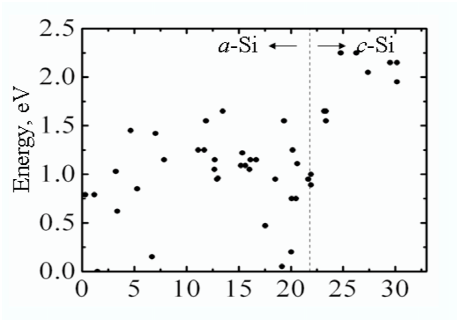

Figure 4.4: The interstitial energy versus x-position is shown.

interstitial stability.

To further investigate the cause of interstitial stability, we examined the bonding mechanisms of several interstitials. Figure 5 depicts ELF isosurfaces of (a) a low energy interstitial on the amorphous side of the *a*-*c* interface, (b) an average energy interstitial in the amorphous region, and (c) a high energy interstitial in the crystalline region, (as indicated in Fig. 4). This bonding analysis illustrates that the low energy interstitial forms strong covalent bonds with its four neighbors, while the average energy interstitial forms rather weak bonds with its neighbors, and the high energy interstitial forms virtually no bonds with its neighbors. We also analyzed the bonding nature of the surrounding Si atoms prior to interstitial insertion. Figs. 5(d),(e) and (f) show the ELF isosurfaces of bond networks in the examined local regions (with future interstitial positions as marked with an X). All surrounding atoms are four-coordinated, but we could expect that the covalent Si-Si bonds are rather weak in a highly strained region. Thus, when a Si interstitial is inserted, these strained bonds are able to break and new covalent bonds form with the inter-

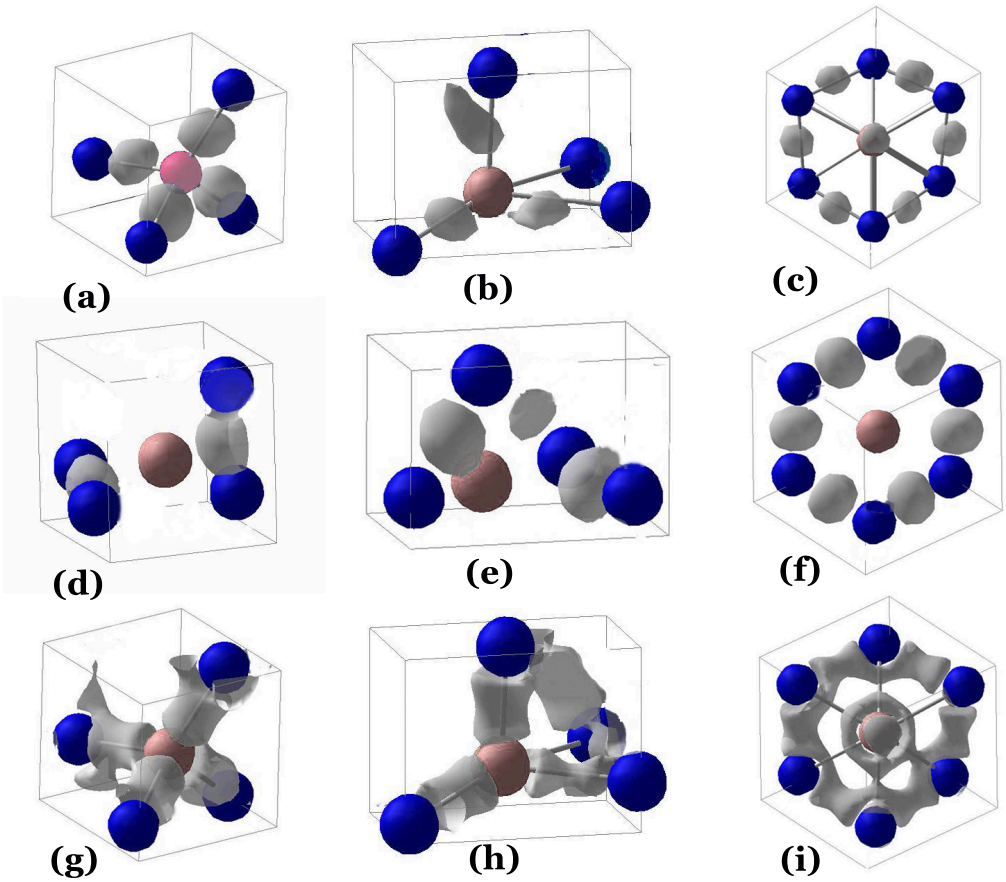

Figure 4.5: The ELFs of (a) a low energy amorphous phase interstitial, (b) average energy amorphous phase interstitial, and (c) a high energy crystalline phase interstitial are shown. Additionally, the ELFs of the local regions shown in (a), (b), and (c) before interstitial insertion are depicted in (d), (e), and (f). In (d)-(f), the site of the interstitial after insertion is marked with an X. All ELF isosurfaces shown have a value of 0.82. (g)-(i) depict charge denisty isosurfaces of relaxed interstitial structures.

stitial. The interstitial incorporation into the substrate lattice clearly results in stabilization of the interstitial structure. In addition, the lattice displacements (caused by the bond rearrangement) may also affect interstitial stability to a certain degree. On the other hand, we would not expect such bond breaking and formation and large lattice displacement by interstitial insertion in the insignificantly strained crystalline Si region. As a result, unlike the vacancy case, there is no significant total energy variation with the interstitial location in the crystalline part of the *a-c* interface structure.

This study suggests that in a highly strained region the stability of interstitials is determined not only by local strain change but also by integration into the substrate lattice. Although the source of interstitial and vacancy stabilization differ, both defects show a strong tendency to be stabilized on the amorphous side of the *a-c* interface.

4.4 Implication for shallow pn junction formation

This study suggests a 'sponge-like' behavior of amorphous Si volumes for vacancy and interstitial accumulation; that is, the defects are likely segregated into the amorphous regions while their densities decrease in crystalline regions. Given the high mobility of defects, even at room temperature, it can be expected that a large portion of single interstitials and vacancies will be absorbed into amorphous volumes during ion implantation and the early stage

of post-implantation thermal annealing. Depending on their relative densities in an amorphous pocket, the accumulated vacancies and interstitials could be annihilated (by interstitial-vacancy recombination) or remain clustered as an amorphous volume is recrystallized.

Due to the described 'sponge-like' behavior, the annihilation and clustering dynamics of vacancies and interstitials will be significantly affected by the presence of amorphous pockets (which can be created during high-dose ion implantation). For instance, we expect that i) annihilation of vacancies and interstitials would be facilitated by recombination when amorphous pockets are available and ii) clustering of excess interstitials and/or vacancies would predominantly occur in the amorphous volumes. As a consequence, substrate subamorphization is expected to play an important role in controlling the density and spatial distribution of defects, and subsequently dopant TED and electrical activation. Recent experimental studies have shown that TED and electrical activation of dopant impurities are strongly influenced by substrate subamorphization. Sultan et al. [86] showed that a subamorphizing implant could be used to reduce B TED. Aronowitz et al. [87] extended these results by finding that the use of a subamorphizing silicon pre-implant could reduce TED as well as enhance electrical activation of B, P, and As dopants during the annealing process. Schenkel and co-workers have subamophized Si to increase ^{31}P activation [88]. They plan to extend this method to implant single ^{31}P dopants into amorphous silicon pockets to gain precise control over single dopant activation. From experimental results, it is clear that amorphous

silicon regions can positively influence ultrashallow junction formation. Our finding that the strained interface alters the defect density in adjacent silicon regions may provide some understanding of the source of these experimental observations. In addition, our results provide motivation to study the fate of defects in the amorphous volumes as they recrystallize.

4.5 Conclusions

Our DFT slab calculations show that interstitials and vacancies tend to segregate to the amorphous side of the *a*-*c* Si interface. The most stable defect position tends to be 3-4 Å from the *a*-*c* interface. Vacancies and interstitials in the the amorphous Si side are predicted to be approximately 2.5 eV and 2.0 eV more stable than those in the crystalline Si part, respectively. It is found that i) vacancy stabilization in amorphous Si is due to strain relief provided to the silicon lattice by the vacancy and ii) interstitial stabilization is due to bond rearrangement associated with interstitial integration into the substrate lattice. This study suggests that substrate subamorphization may play an important role in controlling the density and spatial distribution of defects, and consequently, dopant TED and electrical activation. Our results provide a potential explanation for the dopant TED reduction and enhanced dopant activation that have been experimentally observed when subamorphization strategies have been employed. We believe the findings we present here show the importance of understanding the role of strained *a*-*c* interfaces in affecting defect density in its vicinity and that these findings should spur additional

study on the behavior of defects in amorphous regions as they recrystallize.

Chapter 5

Vacancies and Interstitials at Si-SiO_2 Interface

5.1 Introduction

Atomic-level understanding of defect and impurity behavior at the oxide interfaces is crucial in the evolution of semiconductor technology. The formation and dynamics of interstitial Si in the vicinity of Si/SiO_2 are of particular interest as they directly influence the fabrication and performance of Si-based electronic and photonic devices. Included among those effects are the redistribution and electrical activation of dopant impurities[89, 90] in the formation of ultrashallow junctions for deep submicron MOS devices, Silicon on Insulator (SOI) technology and growth and structure of oxide-embedded Si nanocrystals[91, 92, 93] for memory and photonic devices.

Most theoretical studies have focused on exploring the behavior of point

defects in the well-defined crystalline Si[14, 15, 17, 16, 18] and SiO_2. [94] Little is therefore known about defect formation, diffusion, clustering, and annihilation in complex systems, such as surfaces, interfaces, and amorphous regions. Silicon surfaces [20, 21, 95, 96] and Si/SiO_2 interfaces [19, 97] are considered to be an effective sink for excess interstitials and vacancies in Si. The surface and interface annihilation directly influence defect concentrations in Si, which in turn affects redistribution and electrical activation of dopant impurities during ultrashallow junction formation. [3, 13] With continued scaling of devices, the surface proximity effect become more important, but a detailed study of the interactions of native defects with the Si surfaces and Si/SiO_2 interfaces is still lacking.

In this work we examine the structure, bonding, energetics, and diffusion of interstitials in the vicinity of the defect-free Si/SiO_2 interface. This study intends to increase our understanding of interstitial dynamics in the Si/SiO_2 composite system. Such improved understanding will greatly contribute to developing a better physical model not only for ultra-shallow junction formation in Si, but also for silicon oxidation. Here, we consider two different interface structures: i) Si(001)/crystalline SiO_2 (tridymite) and Si(001)/amorphous SiO_2 (a-SiO_2).

Figure 5.1 shows the interface structures of (a) Si/tridymite and (b) Si/a-SiO_2 considered, together with the strain energy of each atom. For both cases, the strain built at the interfaces reduces rapidly so that the strain energies at the fourth Si sublayer from the interface is negligible. A continuous

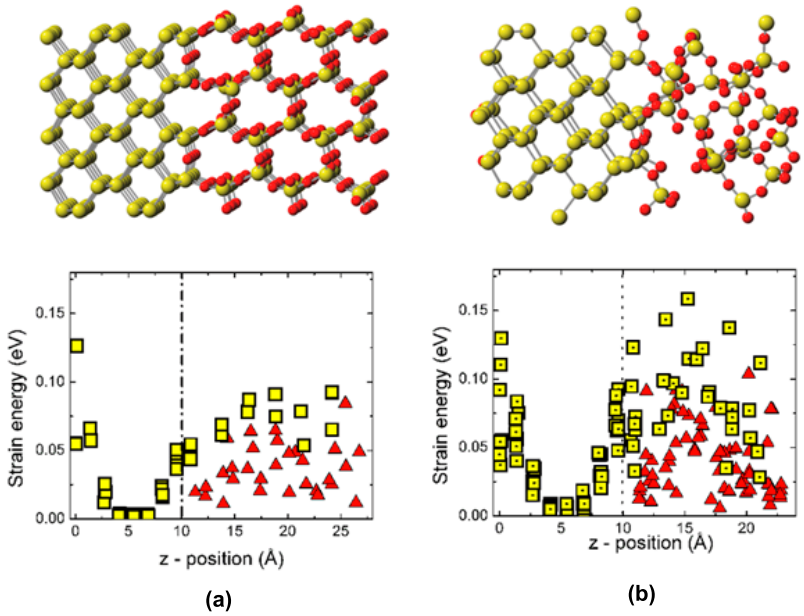

Figure 5.1: Configurations (top)and strain distributions (bottom) of (a) *c*-Si/*c*-SiO_2 and (b) *c*-Si/*a*-SiO_2 periodic systems. The Si/SiO_2 interfaces are positioned at z=0 and z=10 Å. Si and O atoms/strain energies are indictaed in yellow(light gray) and red(dark gray), respectively.

random network (CRN) model [49, 84, 52] is used for the construction of Si(001)- a-SiO_2 (Si/a-SiO_2) structures. Starting with a periodic Si/tridymite (Si/c-SiO_2) structure (which contains nine c-Si atomic layers and four a-SiO_2 layers), an amorphous SiO_2 layer is created via a large number of bond transpositions while the crystalline Si layer is fixed. The lateral size of the simulation cell corresponds to the (2×2) cell of Si, with a Si lattice constant of 5.431 Å. First, the amorphous SiO_2 layer is randomized. Then, the whole system is relaxed at 1500° K via a sequence of bond switching (which is performed using the Metropolis Monte Carlo method based on energetics from Keating-like potentials. [46] To check the reliability of this approach, we also constructed a-SiO_2, with fixed experimental density of 2.2 g/cm^3, yielding the average Si-O-Si bond angle of $136° \pm 15°$, consistent with experimental measurements [98].

We calculate the structure and energies of Si interstitials using plane-wave pseudopotential method within the density functional theory (DFT) [28, 29], as implemented in Vienna ab-initio Simulation Package (VASP) [30, 31]. The exchange-correlation energy functional is represented using the generalized gradient approximation (GGA) in the Perdew and Wang form (PW91)[37]. To represent nuclei and core electron shells of O and Si atoms we have used ultra-soft Vanderbilt-like [39] pseudo-potentials[54]. Outer electron wave-functions are expanded with plane-wave basis set upto cutoff energy of 300 eV. For the k-space summation, we use the $(2 \times 2 \times 1)$ Monkhorst-Pack mesh [38] and finite temperature smearing.[99] All atoms are fully relaxed using the conjugate

gradient method to minimize the total energy until all residual forces on each constituent atom become smaller than $5 \cdot 10^{-2}$ eV/Å. To examine convergence in the k point sampling and kinetic energy planewave cutoff we performed several additional calculations with a higher 400 eV cutoff energy E_{cut} and a denser $(4 \times 4 \times 1)$ k-point mesh. For both cases we increased a FFT mesh to contain all wave vectors up to $2\sqrt{E_{cut}\frac{2m}{\hbar^2}}$ in order to avoid completely possible 'wrap-around' errors. We also optimize realspace projection operators to yield the precision of up to 4×10^{-4} eV/atom. These test calculations yield just a small variation (of less than 0.1 eV) in relative total energies. The (2×2) interface supercell may be insufficient to portray all possible atomic configurations at the complex a-SiO_2 and c-Si interface [100]. However, we believe the model structure can capture the important physical features of the interface, such as local strain variation and atomic structure, considering that the defect free SiO_2-Si interface structure is rather well defined.

We calculate diffusion barriers and pathways using the nudged elastic band method (NEBM).[55].

We analyze bonding mechanisms using the electron localization function (ELF). [43, 45]

5.2 Si interstitials at interface

For the sake of reference, we first calculate the structure and energetics of neutral interstitials in the Si bulk as well as in the inner Si layer of Si/SiO_2 supercell (as depicted in Fig.5.1). For both cases, among three configurations consid-

ered [such as (110)-split, Hexagonal (H), and Tetrahedral (T)], the (110)-split and H interstitials are almost energetically equivalent, and they are about 0.3 eV more favorable than the T interstitial. (The calculated formation energies are in excellent agreement with previous DFT studies for neutral interstitials in the Si bulk [14, 17]). This suggests no significant interface effect exists at the fourth Si sublayer from the Si-SiO_2 interface. This conclusion can also be inferred from the unnoticeable strain at the fourth layer (Fig. 5.1). Herein, we therefore estimate the interstitial formation energy at various locations in the Si-SiO_2 supercells by comparing with the (110)-split interstitial at the fourth Si sublayer. The fourth layer (110)-split interstitial is hereafter referred to as the bulk (110) interstitial unless specified otherwise.

c-Si/*c*-SiO_2 interface

To examine the relative stability of single interstitials in the *c*-Si/*c*-SiO_2 system, we calculate a variation in total energy by placing an interstitial at various locations. In the Si part, the (110)-split interstitial turns out to be the most favorable. In fact, at the first three sublayers from the interface its formation energy is a function of the split-direction, parallel or perpendicular to the Si-O-Si bridge row. For all locations examined, the perpendicular state is more energetically favorable than the parallel state. (The energy gain is about 0.1 eV at the second sublayer, and it becomes negligible at the third sublayer.) For the most stable (110)-split interstitial at each layer, we find the formation energy has virtually no change between the third and fourth Si sublayers, and

it drops by approximately 0.1 eV at the second sublayer largely due to strain induced by the Si/SiO_2 interface.

At the c-Si/c-SiO_2 interface, as depicted in Fig. 5.2a, we identify three stable interstitial configurations: i) (111)-split where an interstitial and an interface Si atom are aligned in the (111) direction while sharing a lattice site, ii) Si^{2+}-O bond centered (BC_I), where an interstitial is incorporated in a Si^{2+}-O bond and iii) Si^{4+}-O bond centered (BC_{II}), where an interstitial is incorporated in a Si^{4+}-O bond. The (111)-split and BC_I interstitials are respectively predicted to be 1.6 eV and 0.5 eV more stable than the bulk (110) interstitial, but the BC_{II} interstitial turns out to be 0.3 eV less favorable than the (110) bulk interstitial. We also find that an interstitial at the Si^{4+} -O BC site in the middle of the SiO_2 layer is energetically less favorable than the BC_I interstitial at the interface, mainly due to larger strain caused by greater (interstitial induced) lattice distortions (*vide infra*). These results suggest that excess Si atoms in the c-Si/c-SiO_2 system may be preferentially trapped at the interface. The atomic structure and bonding mechanisms of the interface interstitials are discussed below.

For the (111)-split state (Fig. 5.2b)), interstitial insertion results in the formation of new (strained) bonds between the interstitial and neighboring Si atoms, 3, 4, and 5, by breaking the original Si-Si bonds, 3-4 and 3-5. The (111)-split structure is very unlikely in c-Si because of the large strain it induces, but the flexibility of the Si-O-Si bond angle appears to accommodate the interstitial-induced lattice distortions at the interface. The (111)-split

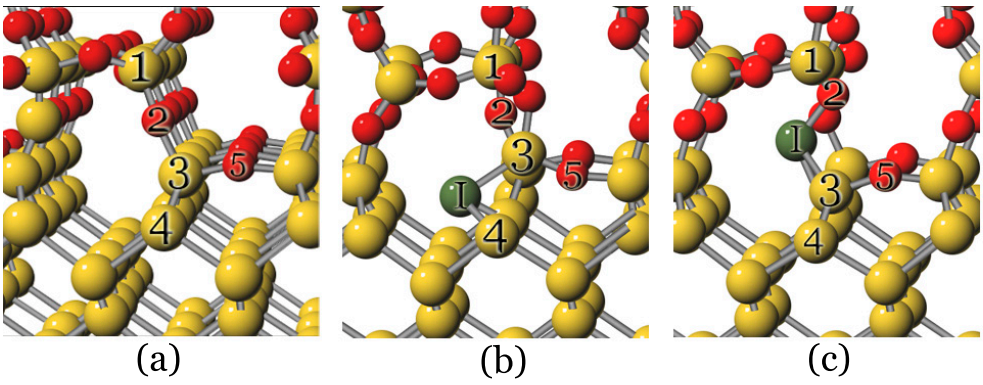

Figure 5.2: Atomic structures of (a) defect-free$c$-Si/c-SiO_2 interface, (b) (111)-split interface interstitial, and (c) BC_I interface interstitial. The green (indicated as I), yellow(light gray) and red(dark gray) balls represent the interstitial, Si and O lattice atoms, respectively.

state renders the interstitial and interface (indicated as 3) atoms threefold coordinated. It turns out there is charge transfer from the interface atom to the interstitial, leaving an electron lone pair on the interstitial [as illustrated by the ELF isosurface plot (Fig. 5.3a)). The presence of an lone pair is also manifested by the interstitial local density of states (LDOS), showing two sharp peaks just below the c-Si valence band edge (Fig.5.4 a)).

For the BC_I state, the interstitial insertion leads to a large displacement of the interface O atom in the (110) direction, which in turn induces significant distortions in the SiO_2 part. The resulting strain makes the BC_I structure less stable than the (111)-split structure. In the c-SiO_2 bulk, a BC interstitial causes even larger strain, and thus it becomes energetically less favorable than an interface BC interstitial. The ELF and charge density analysis shows that the BC_I interstitial forms bonds with the interface Si (indicated as 3) and O

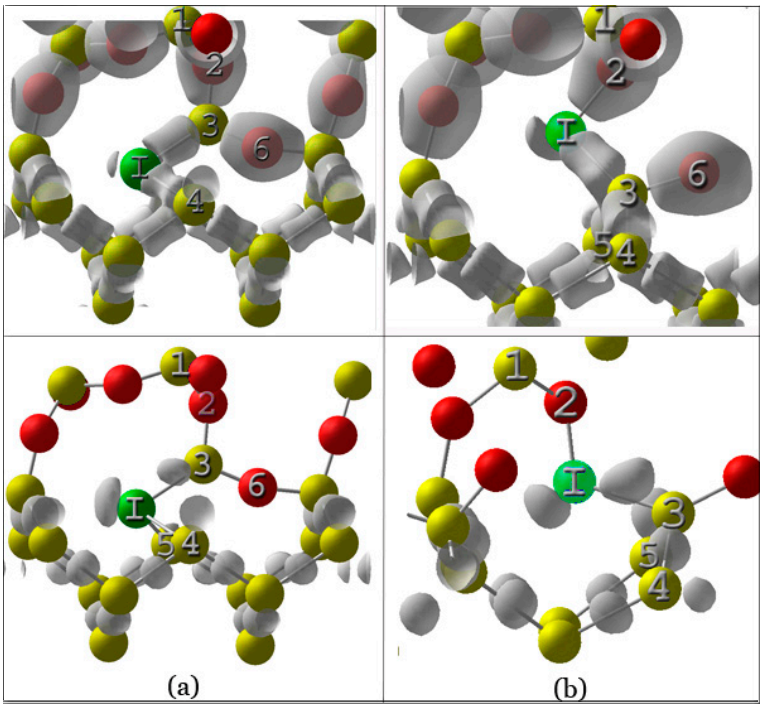

Figure 5.3: Isosurface plots of charge densities (top) and ELFs =0.9(bottom) of (a) (111)-split and (b) BC_I interstitial. The green (indicated as I), yellow(light gray) and red(dark gray) balls represent the interstitial, Si and O lattice atoms, respectively.

(indicated as 2) atoms, but not as strong as normal Si-Si (in c-Si) and Si-O (in c-SiO_2) bonds. The Si-Si bond (between the interstitial and interface Si atoms) appears to be highly distorted; that is a bond center is displaced away from the atomic interaction line, while moving towards the interface Si atom. The induced strain also weakens the Si-O bond (between the interstitial and interface O atoms). The remaining two valence electrons of the interstitial are localized to form a lone pair, as demonstrated by ELF (Fig. 5.3b)) and LDOS (Fig. 5.4b)) plots.

The BC_{II} interstitial shows a similar bonding mechanism to the BC_I interstitial, but the former brings about greater lattice distortions and thus larger local strain. The interstitial insertions at the Si^{4+}-O and Si^{2+}-O bond centers alter the charge state of the lattice Si atoms from Si^{4+} and Si^{2+} to Si^{3+}- and Si^{1+}, respectively. The resulting changes in suboxide penalty energy are -0.24 eV and $+0.04$ eV, respectively, according to suboxide penalties (Si^{4+} = 0.0, Si^{3+} = 0.24, Si^{2+}=0.51, and S^{1+}=0.47 in eV) from a recent theoretical study.[101] Thus, we could attribute the about 0.8 eV gain of the BC_I over the BC_{II} state to both its lower local strain and suboxide penalty.

c-Si/*a*-SiO_2 interface

Our calculation results show that in general the structure and bonding of single interstitials in the c-Si/a-SiO_2 system are similar to those in the c-Si/a-SiO_2 system. However, their formation energies vary significantly site to site near the interface mainly because of a variation in local strain by the disordered

nature of a-SiO_2. We also find that interstitials can be greatly stabilized in the a-SiO_2 bulk, implying that excess Si interstitials may favorably diffuse into the SiO_2 layer. (Recall that interstitials are predicted to remain preferentially at the interface in the c-Si/c-SiO_2 system). Next, we discuss the structure, bonding, diffusion, and energetics of single interstitials examined in the c-Si/a-SiO_2 system.

We identify three stable states of interstitials at the Si/a-SiO_2 interface: (a) (111)-split, (b) Si^{2+}-O bond centered (BC_I), and (c) Si^{4+}-O bond centered (BC_{II}). Each state is examined at several different locations, showing a significant site-to-site variation in the total energy. On average, however, the interface interstitials turn out to be substantially more favorable than the (110)-split bulk interstitial.

The (111)-split interstitial is examined at eight different locations. The most and least stable states are respectively 1.2 eV and 0.03 eV more stable than the (110)-split bulk interstitial, with an average energy gain of about 0.8 eV. Here, it is interesting to note that the (111)-split interstitials are overall less favorable than those at the c-Si/c-SiO_2 interface. This is largely attributed to the disordered a-SiO_2 network that imposes more strain on the (111)-split structures, relative to the c-Si/c-SiO_2 case.

Unlike at the c-Si/c-SiO_2 interface, both BC_I and BC_{II} interstitials turn out to be energetically more favorable than the (110)-split bulk interstitial, with an average energy gain of 0.4–0.5 eV for seven different locations examined. For both BC_I and BC_{II}, the most and least stable ones are 1.6 eV

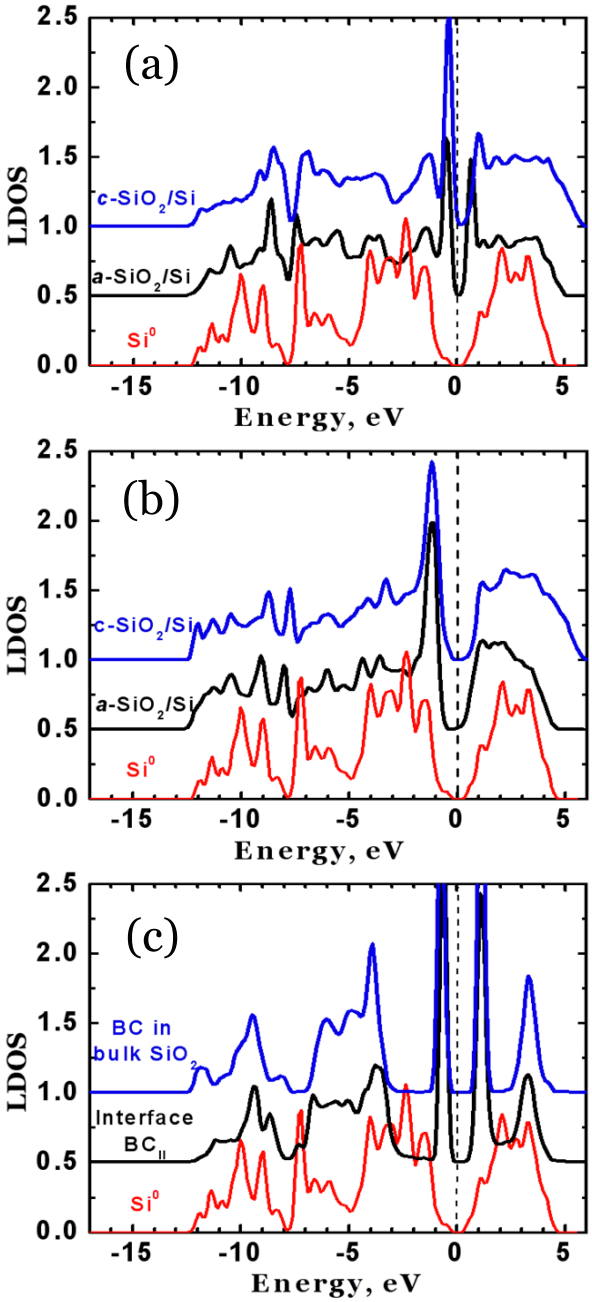

Figure 5.4: Local density of states of a single Si interstitial in (a) (111)-split, (b)Si^{2+}-O bond-center (BC_I), and (c) Si^{4+}-O bond-center (BC_{II}) states. Si^0 is LDOS of a Si atom in a deep Si layer (away from interface). The LDOS plots are drawn with a vertical offset of 0.5 units for clarity.

more and 0.1 eV less stable than the (110)-split bulk interstitial, respectively. The BC interstitial stability is found to be determined largely by local strain associated with bond topology on the SiO_2 side; that is, more flexible bond topology with tensile strain yields more stable interstitials.

We also find that BC interstitials in the a-SiO_2 bulk are as stable as those at the c-Si/a-SiO_2 interface. Moreover, as predicted by recent theoretical studies, [102] excess Si atoms in a-SiO_2 can be further stabilized by incorporation into the Si-O bond network. (That is, an excess interstitial is bonded to neighboring two Si and two O lattice atoms by breaking two original Si-O bonds.) We calculate the interstitial incorporation at several locations in the middle of the a-SiO_2 layer. It turns out that the most stable one is about 1.8 eV more stable than the (110)-split bulk interstitial, with an average energy gain of 0.5 eV.

As an interstitial moves into a deeper Si sublayer from the Si-SiO_2 interface the total energy overall increases with a significant site-to-site variation because of the unevenly distributed interface strain. In some regions the interface strain significantly influences the stability of interstitials up to the third Si sublayer; for instance, the energy gains at the first, second, and third Si sublayers are 0.4 eV, 0.2 eV, and 0.1 eV, respectively, relative to the (110)-split bulk interstitial. The presence of such low-energy channels may in turn facilitate interstitial migration to the Si-SiO_2 interface. We also find that the formation of (110)-split interstitials more strongly depends on their split direction, parallel or perpendicular to the Si-O-Si bridge row, than the c-Si/c-SiO_2

case. For all locations examined, the maximum difference can be 0.8 eV at the first sublayer, then it reduces to 0.1 eV at the third sublayer and virtually disappears at the fourth sublayer.

5.3 Structure of excess silicon atoms in SiO_2

To elucidate complex behavior of Si interstial at Si/SiO_2 interface and decouple the role of interface from the one of the SiO_2 we also have to consider excess Si atoms in bulk SiO_2. [1] c-SiO_2 (α-quartz) is modeled using a 72-atom supercell with lattice constants of a = 4.917 Å and c = 5.430 Å. Bulk a-SiO_2 is constructed using a continuous random network (CRN) model[84, 52].

5.3.1 Interstials in defect-free crystalline SiO_2 (α-quartz)

As summarized in Fig. 5.5, we have identified three stable excess Si configurations:

(1) Fourfold Coordinated (FC) where the excess Si atom is bonded to neighboring two Si and two O lattice atoms by breaking two original Si-O bonds;

(2) Bond Centered (BC) where the excess Si atom is located at the center of a Si-O bond;

[1] Results reported in this section are after the study "Structure and Diffusion of Excess Si Atoms in SiO_2" by D. Yu, T. Kirichenko, G. Hwang and S. Banerjee, submitted for publication in Physical Review B.

(3) Ring Centered (RC) where the excess Si atom is located at the center of a six-member ring by weekly interacting with neighboring two Si and two O lattice atoms.

Figure 5.5(b) shows two different FC structures; that is, the excess Si insertion may involve the break of two Si-O bonds associated with either the third or the second Si neighbors on a six-member ring (C-F or A-C) while forming four new bonds between the inserted Si atom and the dissociated Si and O lattice atoms. (Hereafter the former and the latter are referred to as FC_I and FC_{II}, respectively.) The FC_{II} state turns out to be 0.34 eV less favorable than the FC_I state, mainly because it causes greater lattice distortions and in turn larger strain.

There are two slightly different Si-O BC sites in α-quartz [Fig.5.5(c)]; that is, long (A-1, d = 1.62 Å) and short (C-1, d = 1.61 Å) Si-O bonds. (Hereafter, the states of excess Si residing in the long and short bond centers are referred to as BC_I and BC_{II}, respectively.) It turns out that the BC_I and BC_{II} states nearly degenerate, and they are about 0.57 eV less energetically favorable than the most stable FC_I state.

As shown in Fig. 5.5(d), the excess Si placement at a ring center results in a noticeable inward displacement of two Si and two O lattice atoms on the six-member ring to interact with the inserted Si atom. The RC state is predicted to be 1.8 eV less stable than the FC_I state.

The bonding mechanisms for the FC, BC, and RC structures are analyzed based on electron localized functions (ELF), decomposed charge densi-

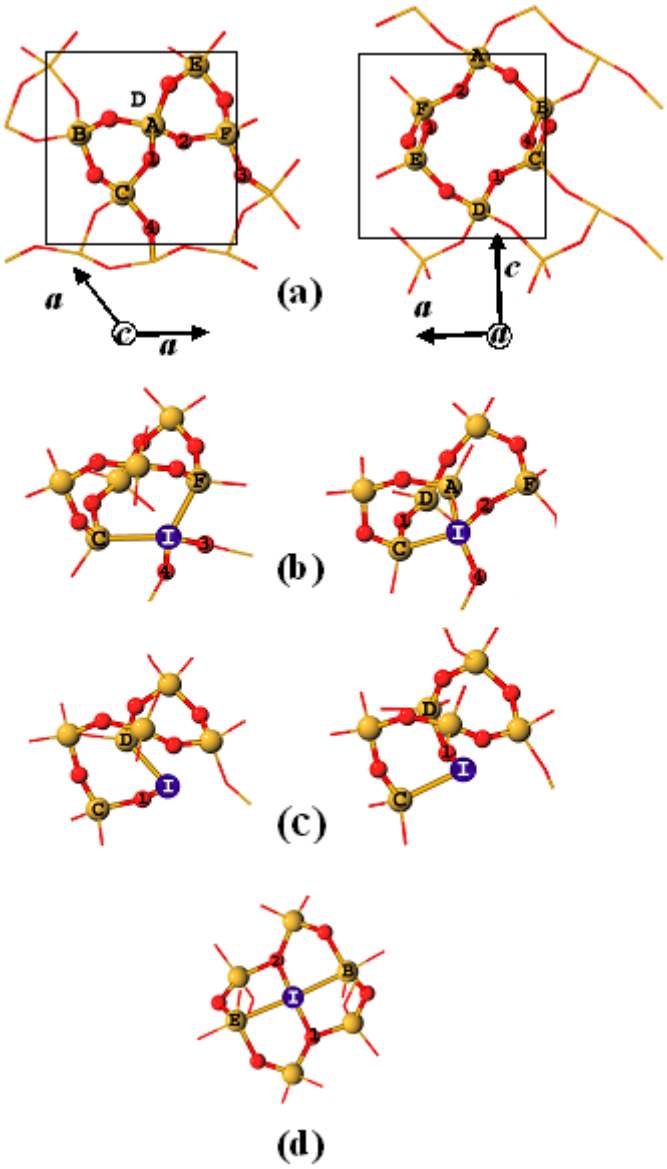

Figure 5.5: Structure of α-quartz and the silicon interstitial structures formed within. (a) α-quartz viewed along its c- and a- axis; (b) FC_I interstitial and FC_{II} interstitial; (c) BC_I interstitial and BC_{II} interstitial; (d) RC interstitial. The FCs and BCs are shown from the c-axis perspective, while RC is from the a-axis. For clarity only relevant atoms in the local structure are shown.

ties, and local density of states (LDOS), as shown in Figs. 5.6 and 5.7.

For the FC_I structure, the ELF analysis [Fig. 5.6(a); left panel] clearly demonstrates the formation of covalent and ionic bonds between the inserted Si atom and neighboring Si and O lattice atoms, respectively. However, due to the local strain induced by significant lattice distortions, the newly formed Si-Si and Si-O bonds are substantially weaker than normal Si-Si (in c-Si) and Si-O (in c-SiO_2) bonds. This can be inferred from excess Si LDOS that exhibits two sharp peaks above the Si^{4+} valence band edge [Fig. 5.7], indicating that the valence electrons of excess Si are partially involved in the bond formation. The rest partial charge tends to be delocalized to populate the lower energy states of neighboring Si and O lattice atoms, as demonstrated by corresponding decomposed charge densities [Fig. 5.6(a); right panel].

For the BC_I structure, the ELF analysis [Fig. 5.6(b); left panel] shows the formation of covalent and ionic bonds between the excess Si and adjacent Si and O lattice atoms, respectively. The induced local strain makes the newly formed Si-Si and Si-O bonds highly distorted, such as the Si-Si bond center is displaced away from the atomic interaction line while moving towards the lattice atom. The remaining two valence electrons of excess Si are localized to form a lone pair, as demonstrated by the ELF. The presence of a lone pair is also manifested by a sharp peak near the Fermi level in excess Si LDOS [Fig. 5.7] and corresponding decomposed charge densities [Fig. 5.6(b); right panel].

The ELF analysis of the RC structure [Fig. 5.6(c)] exhibits weak inter-

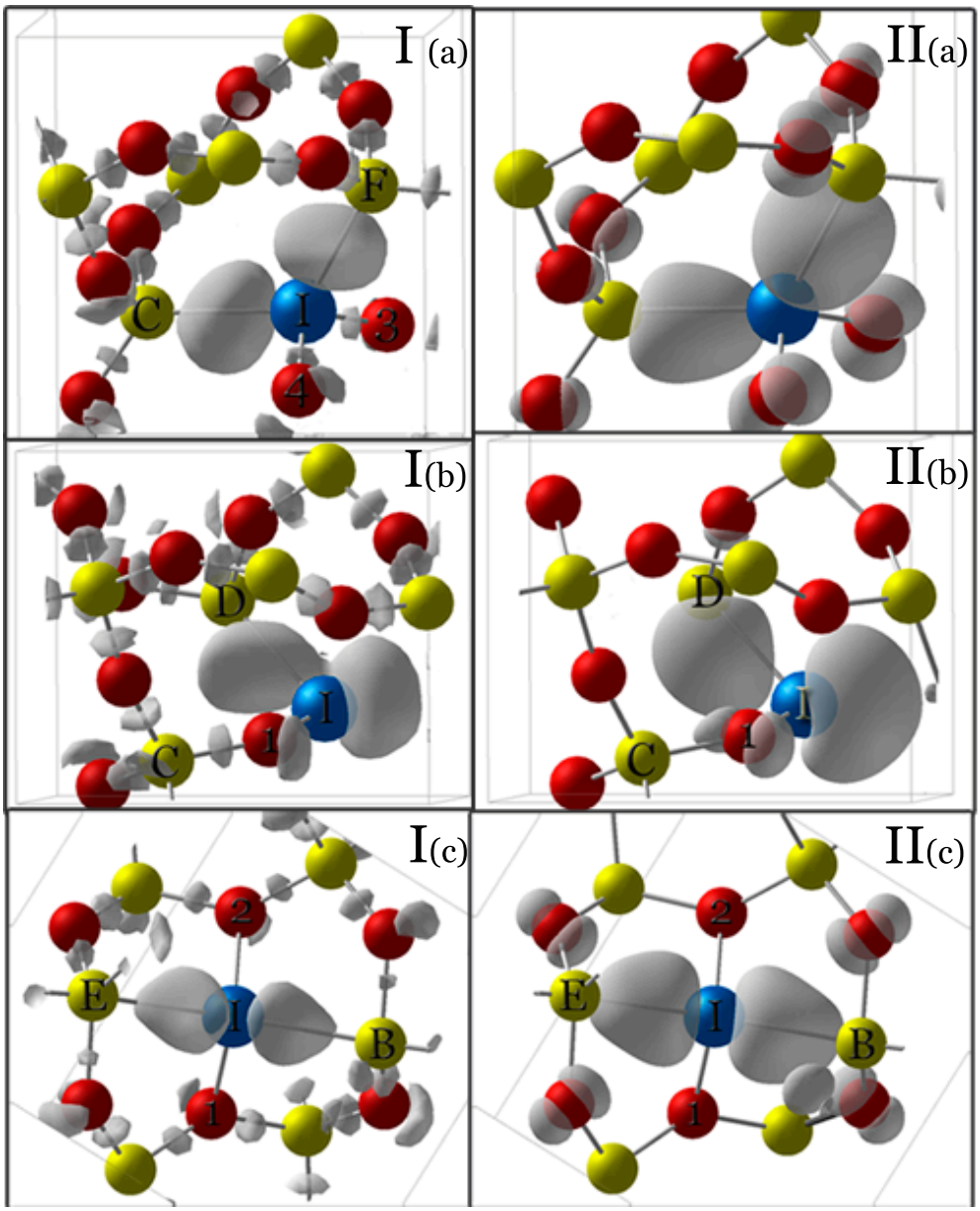

Figure 5.6: ELF=0.82 (Column I) and isosurfaces of decomposed charge density (Column II) of (a) FC_I (b) BC_I and (c) RC interstitials in α-quartz. The decomposed charge densities correspond to the energy range where the the two shaded sharp peaks in DOS of each interstitial stand in Fig. 5.7

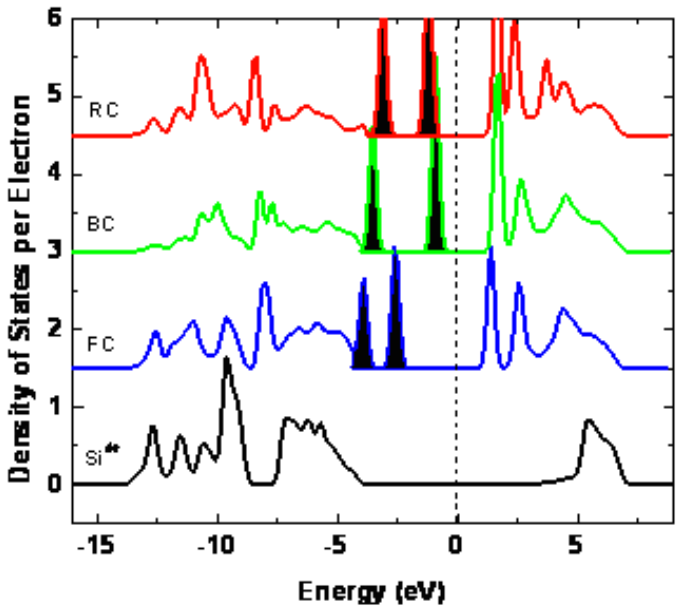

Figure 5.7: Local density of states of excess Si atom in FC_I, BC_I and RC state. Si^{4+} is the silicon atom in pure α-quartz. Zeros are offset by 1.5 unit for clarity. Zero point energy is the Fermi level for Si^{4+} state. The excess silicon DOS are aligned with O 2s band of Si^{4+}

actions between the excess Si and neighboring Si and O lattice atoms. Given that the RC structure yields the least strain, followed by BC and FC structures, the relative energy gains of FC and BC structures are mainly attributed to bond formation with adjacent Si and O lattice atoms.

5.3.2 Interstitial in defect-free amorphous SiO_2

Stable FC and BC structures of excess Si are identified, whereas the RC structure turns out to be unlikely simply because of the lack of symmetric six-member rings in a disordered a-SiO_2 matrix. Here, for good statistics we placed an excess Si atom at many different locations using five different (72-atom) a-SiO_2 supercells. The amorphous network renders very stable FC sites in which excess Si can be fully incorporated into the Si-O network with no significant increase of strain. However, it provides a less number of stable FC sites than α-quartz because of the sparse and disordered network of a-SiO_2 in nature.

The stability of BC structures shows a significant site-to-site variation, depending on local strain. They turn out to be 0.5-2 eV less favorable than the most stable FC structure identified here.

The FC structure yields the Si^{3+}-Si^{2+}-Si^{3+} charge configuration; that is, the charge states of the inserted Si and adjacent Si lattice atoms are 2+ and 3+, respectively. Here, we can expect the migration of a second neighboring O atom to a Si-Si BC site, rendering the Si^{3+}-Si^{3+}-Si^{3+}- Si^{3+}charge configuration. Allowing successive O migration to a Si-Si BC site (which cor-

responds to O-vacancy diffusion), the excess Si can be fully integrated into the amorphous Si-O network, with two separate Si^{3}+-Si^{3+} charge configurations. The resulting change in the suboxide penalty energy is minimal, according to calculated values (of Si^{4+} = 0.0, Si^{3+} = 0.24, Si^{2+}=0.51, and Si^{1+}=0.47 in eV 26). This suggests that the separate structure is energetically comparable to the FC structure, if both cases are fully relaxed.

5.4 Interstitial migration from Si into SiO_2

Figure 5.8 shows a diffusion path with barriers for an interstitial from the first Si sublayer to the Si/SiO_2 interface. Here, we only present interstitial diffusion in a region where interstitial formation energies are relatively lower, i.e., via a low-energy channel as discussed earlier. (In fact, the diffusion barriers are greatly scattered site-to-site, depending on local strain at the interface, but the overall diffusion behavior is alike in all interface regions examined.) We could expect that interstitials preferentially diffuse to the interface via a low-energy channel. An interstitial migrates from the first Si sublayer to the (111)-split site through the adjacent hexagonal site (which turns out to be unfavorable), with no sizable barrier [(a) $\rightarrow$ (b)]. The (111)-split interstitial then shifts in the lattice site while pushing the (original) interface atom 3 towards the BC_I site [(b) $\rightarrow$ (c)]. The kick-in process occurs by crossing an energy barrier of 0.1eV. The Si atom at the BC_I site can further migrate to the BC_{II} site in the SiO_2 region (by switching its position with the adjacent O atom) [(c) $\rightarrow$ (d)]. The exchange of Si and O positions requires overcoming a large energy barrier

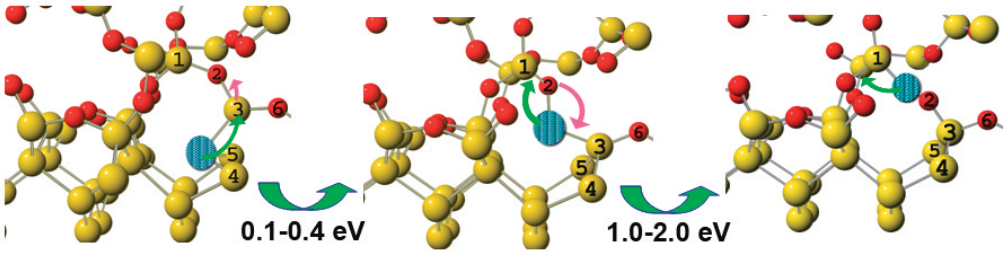

Figure 5.8: Paths and barriers for single Si interstitial diffusion from the first Si sublayer to the Si/SiO_2 interface. (a) (111)-split, (b) BC_I, and (c) BC_{II} states. The shaded, yellow(light gray), and red(dark gray) balls represent the diffusing interstitial, Si and O lattice atoms, respectively

of approximately 1.0, 1.8 and 2.0 eV for three considered interface locations.

Recent theoretical study[102] of excess Si diffusion in a-SiO_2 confirms this mechanism of Si interstitial diffusion in SiO_2. Several possible migration pathways that have been considered by D. Yu and coworkers: (a) O hopping to a Si-Si BC site (or O vacancy diffusion), (b) Si hopping from a FC site to a BC site, (c) Si hopping from a BC site to a BC site, (d) Si hopping from a BC site to a FC site, and (e) O hopping to a Si-Si BC site. Due to the disordered nature of a-SiO_2, the diffusion barriers exhibit a significant site-to-site variation. However, extensive calculations at various locations suggest that the overall barrier for excess Si diffusion is primarily determined by the O-vacancy migration (corresponding to the O hopping to a Si-Si BC site) [(a)] and the FC BC Si hopping [(b)]. For well-relaxed structures, the corresponding O and Si hopping barriers are both estimated to be approximately 4.5 eV, respectively. For the BC-to-BC Si hopping, the majority of the barriers ranges from 2.2 eV to 3.2 eV, depending on the O-Si-O bond network topology as pointed

out earlier. Considering the formation energy difference of 2 eV between the fully relaxed FC and BC structures, the overall barrier for excess Si diffusion between fully integrated states (at either Si^{3+}-Si^{2+}-Si^{3+} or two separate Si^{3+}-Si^{3+} charge configurations) can be approximated to be 4.5 - 5.2 eV. This is in good agreement with 4.74 ± 0.25 eV as estimated from recent experimental observations .8

These results demonstrate the ease of interstitial stabilization at the Si-SiO_2 interface, with no sizable diffusion barrier from the Si side. They also suggest that excess Si interstitials may favorably diffuse into the SiO_2 layer during thermal oxidation and ultrashallow junction formation, as the SiO_2 layer mostly remains amorphous.

5.5 Silicon vacancies at Si-SiO_2 interface

Interactions of dopant atoms and point defects with surface films and interfaces are becoming of major importance in determining the concentrations of dopants and point defects, and therefore the resulting redistribution of dopants during high temperature treatments. Thus understanding the behavior of native point defects on the atomic scale is an important issue in current silicon technology. However, it is extremely difficult to provide a direct experimental study of the details of the structure and dynamics of native defects at the very interface. On other hand, theoretical investigation of defects behavior at interface until recently was hindered by the lack of realistic interface structures and computational cost involved in study of amorphous-crystalline interface.

In this section we will address the structure, bonding, energetics and diffusion of neutral Si vacancies at the vicinity of Si/a-SiO_2 interface.

To model Si/SiO_2 interface we consider defect-free Si(001)/amorphous SiO_2 (a-SiO_2) structure. For its constraction we use continuous random network (CRN) model [49, 84, 52]. Figure 5.1 shows the constructed Si/a-SiO_2 interface, together with the strain energy of each atom. We find that strain built at the interfaces reduces rapidly and becomes negligible at the fourth Si sublayer from the interface.

To check the reliability of the structure constracted using this approach, we also constructed a-SiO_2, with fixed experimental density of 2.2 g/cm^3, yielding the average Si-O-Si bond angle of $136^\circ \pm 15^\circ$, consistent with experimental measurements. [98] For structure and energetics of defects we employ "large" $4 \times 4 \times 5.26$ Si/SiO_2 supercell, whereas defect dynamics was studied on "small" $2 \times 2 \times 4.26$ supercell. We calculate interstitial defect structures and energies using plane-wave pseudopotential method within the density functional theory (DFT) [28, 29], as implemented in Vienna ab-initio Simulation Package (VASP) [30, 31]. The exchange-correlation energy functional is represented using the generalized gradient approximation (GGA) in the Perdew and Wang form (PW91)[37]. To represent nuclei and core electron shells of O and Si atoms we have used ultra-soft Vanderbilt-like [39] pseudo-potentials[54]. Outer electron wave-functions are expanded with plane-wave basis set upto cutoff energy of 210 eV. For the k-space summation, we use gamma point only for the "large" supercell and the $(2 \times 2 \times 1)$ Monkhorst-Pack mesh[38] for the "small"

supercell. All atoms are fully relaxed using the conjugate gradient method to minimize the total energy until all residual forces on each constituent atom become smaller than $5 \cdot 10^{-2}$ eV/Å. We calculate the diffusion pathways and barriers under the static approximation using the climbing nudged elastic band method. [55]

5.5.1 Subinterface vacancy structure and energetics

For the sake of reference we first calculated neutral vacancy structure and formation energy in the bulk 216 atom *c*-Si supercell as well as inner Si layer of Si/SiO_2 supercell (as depicted in Fig.5.1). In bulk 216 supercell we found formation energy of single vacancy to be 3.7 eV, an observed significant reduction to 1.6 eV per vacancy for the six-member ring vacancy cluster, in good agreement with recent theoretical studies [71].

For Si/SiO_2 supercell we found that variation in total energy for single vacancy created at 5th and 6th Si inner layers 5.1 to be less than 0.2 and 0.1 eV, correspondingly, with virtually no changes in relaxed vacancy geometry compared to the bulk Si 216 atoms supercell. Vacancy formation energy determined largely by relaxation of the four nearest neighbors, two of which are located one layer closer to interface than the vacancy itself. Insignificant variations in formation energy of vacancies at the 5th sublayer suggests that there is no significant interface effect exist at the fourth Si sublayer from the $Si\text{-}SiO_2$ interface. Herein, we therefore estimate the vacancy formation energy at various locations in the *c*-Si/a-SiO_2 supercell by comparing with the va-

cancy at the sixth c-Si sublayer. The 6th sublayer vacancy is hereafter referred to as the bulk vacancy unless specified otherwise.

To examine the relative stability of single vacancies in the c-Si/a-SiO_2 system, we calculate a variation in total energy by placing a vacancy at various sub-layers. Vacancy formation energy at each layer is calculated at several different locations, showing a significant site-to-site variation in the total energy, mainly because of a variation in local strain. On average, however, at the interface and the first two c-Si sublayers under the interface vacancies turn out to be substantially more favorable than the bulk vacancy. Vacancy formation energy is reduced by 0.9 eV and 1.3 eV at the III and II Si sublayers, respectively. We attribute this stabilization to the two factors: i) strain relief c-Si sub-layers under Si/SiO_2 interface, and ii) strain-assisted pairing between vacancy neighbors and the effect change of periodicity and chemical composition of the system on electronic states associated with a vacancy. Next we discuss the influence of these two factors on sublayer vacancy stability in detail.

Overall formation of c-Si/a-SiO_2 interface introduces tensile strain into Si substrate due to the difference a-SiO_2 and c-Si molecular volumes. However Si atoms at sub-interface are subject to alternating strain depending on the specific location: tensile for the atoms located under the troughs formed at interface and compressive for the atoms located under Si-O-Si bridges. Removal of one Si atom from the c-Si sublayer provides immediate strain relief on the vacancy nearest neighbors. Furthermore, upon vacancy structure relaxation

additional reduction of strain at the second and third nearest neighbor shells occurs. We therefore suspect that one of the major sources of vacancy stabilization at c-Si sublayers is strain-assisted pairing and immediate strain relief. Indeed, relaxed vacancy structures at second and third sublayers show significant inward relaxation compared to the bulk. For vacancy at the third sublayer the largest stabilization is observed for vacancies created directly under Si-O-Si bridge, where vacancies on average are 1.2 eV more stable compared to the bulk vacancy. Two of the bond lengths between first shell of vacancy neighbors at second and forth Si sub-layers are reduced from 3.86 Å to $\cong 2.7 - 2.8$Å. The other four distances between vacancy nearest neighbors are reduced to 3.3-3.5 Å. This distance can be compared to the considerably longer 3.6-3.7Å distance between pairs of first shell neighbors of the relaxed bulk vacancy. At some highly strained locations at interface (what can be identified by distorted Si back bonds), vacancy formation energy at the second sublayer is reduced by 1.8 eV, which is comparable with the vacancy stabilization at the Si/SiO_2 interface (vide infra).We found that the interface strain significantly influences the stability of vacancies up to the fourth Si sub-layer, with a possible formation of a (110) zig-zag chain of low energy vacancy sites in (100) direction. The presence of such low-energy channels may in turn facilitate vacancy migration to the $Si\text{-}SiO_2$ interface as well as formation of thin ($\cong$ 10 Å) vacancy-reach layer near the very interface. This will in turn enhance pile-up and diffusion of dopants that strongly interact with vacancies, such as As.

We carefully examine the influence of the interface on the electronic

structure of the sub-interface and interface vacancy. Consider vacancy created by removing Si atom in the *c*-Si layer away from interface. In unrelaxed vacancy structure one of the vacancy-induced defect levels is created inside the valence band manifold and the one triply degenerate level inside the band gap. The band gap level is unstable with respect to Jahn-Teller (JT) distortion due to the orbital degeneracy. As vacancy structure relaxes, JT distortion lows the symmetry and partially remove degeneracy of the triplet, splitting it into two levels in the band gap. It has been shown [Antonelli, Kaxiras, Chadi, PRL 98] that two distinct JT distortions can be associated with neutral vacancy in Si. Small magnitude distortion is favored at zero external pressure, while large magnitude distortion is more stable in presence of compressive strain which also is present under Si-O-Si interface bridge. This pairing will sweep defects states from the band gap. The effect of pairing close to interface is well reflected in the vacancy DOS and should be distinguished from the pure strain relief effect discussed earlier. The bulk vacancy DOS shows a sharp peak at mid gap in the local densities of states (LDOS) plot. This peak can be clearly associated with b2 and b1 deep states. However for the third and second sublayer vacancies we observe no states in the gap but rather two new peaks: one under the valence band maxima and another shallow in the conduction band. Naturally, as doubly occupied defect level moves from band gap into the valence band, energy of the vacancy structure is reduced.

Besides pure effect of strain assisted pairing we should also take into account possible interaction between vacancy states and the states close in

energy what are induced by distorted Si bonds near the interface as well as by interface sub-oxidized Si atoms. Although it is difficult to distinguish between this resonance effect and strain-assisted pairing, we can gain some insight by comparing vacancy stabilization under Si/aSiO$_2$ with Si/c-SiO$_2$ interface. Both interfaces have comparable oxidation-induced strain. However the interface states Si/a-SiO$_2$ inherently have broader spectrum compared to the Si/c-SiO$_2$. Thus coupling of the interface-induced states with vacancy defect states is more feasible in case of Si/aSiO$_2$. This may explain why we observe much smaller vacancy stabilization of 0.6 eV under Si/c-SiO$_2$

5.5.2 Interface vacancy structure and dynamics

Next we investigate Si vacancy structure at Si/SiO$_2$ interface (Si layer I). To create interface vacancy we remove Si atom 7 (Fig. 5.9(a)) from the interface Si-O-Si bridge and relax the configuration. Upon structure relaxation (5.9(b))bridging O atom 6 forms the bond with the second layer Si atom 11.

The arm O atom 4 is shifted down towards II layer Si atom 10, forming another Si-O bond. Thus all atoms in interface vacancy structure become fully coordinated. As a result interface vacancy structure does not have any dangling bonds at all and is expected to be much more energetically stable compared to vacancy in c-Si layer. The interface vacancy structure is examined at eighteen different locations. Each interface vacancy structure is pre-relaxed using same classical Keating-like potential as for construction of Si/SiO$_2$ supercell. Out of several possible configurations at the same inter-

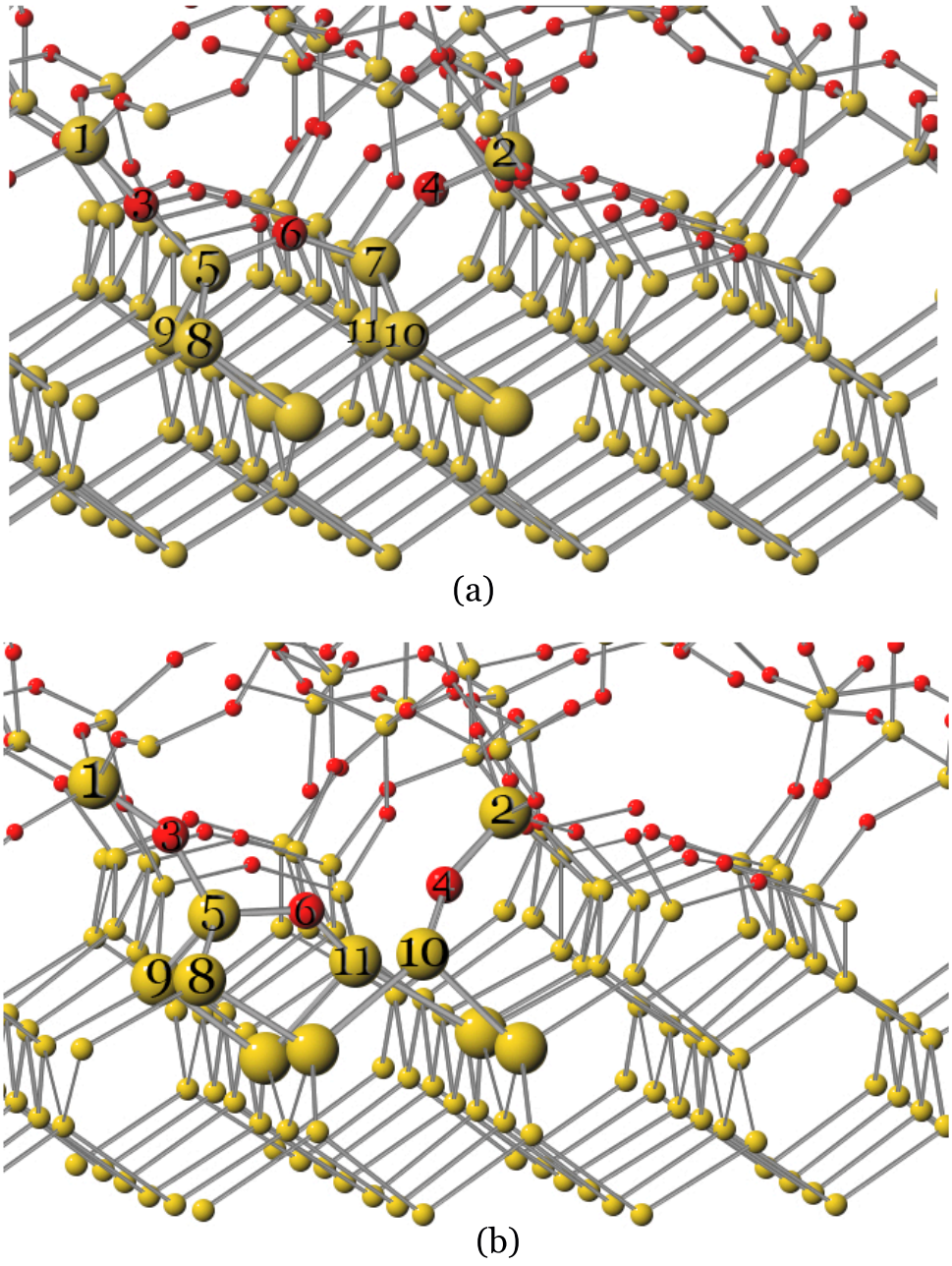

Figure 5.9: (a) Defect-free Si-aSiO$_2$ interface. For the sake of clarity atoms involved in the vacancy structure are enlarged. Si atoms are shown in yellow(light grey) and oxygen atoms are shown in red(dark). (b) Interface Si vacancy structure.

face location the one which introduces the least strain is relaxed farther, using DFT calculation. The most and least stable states are respectively 1.9 eV more and 0.8 eV less stable than the bulk vacancy, with an average energy gain of about 1.0 eV. Vacancy stabilization at the interface is facilitated by rearrangement of interface O atoms and formation of strong Si-O bonds with vacancy neighbors and strongly depends on the a-SiO_2 network topology near interface vacancy site. At elevated temperatures formation of vacancy at interface may introduce topology changes in amorphous oxide network, leading to farther stabilization. In addition, an interface vacancy may migrate along the interface to more energetically favorable position.

To identify the possible mechanism of formation of single vacancy at Si/SiO_2 interface we calculate migration pathway of vacancy to the interface from the c-Si sublayer. Figures 5.10 and 5.11 show a diffusion path for a vacancy from the first Si sublayer to the Si/SiO_2 interface. Here, we only present vacancy diffusion in a region where vacancy formation energies are relatively lower, i.e., via a low-energy channel as discussed earlier. (In fact, the diffusion barriers are greatly scattered site-to-site, depending on local strain at the interface, but the overall diffusion behavior is alike in all interface regions examined.) We could expect that vacancies preferentially diffuse to the interface via a low-energy channel. A vacancy migration from the first Si sublayer to the interface involves concerted motion of three interface atoms: Si atom 2 and O atoms 4 and 5. Si atom 2, followed by bridging O atom 5 moves downward and takes position of vacancy, while O atom 4 detaches at the saddle

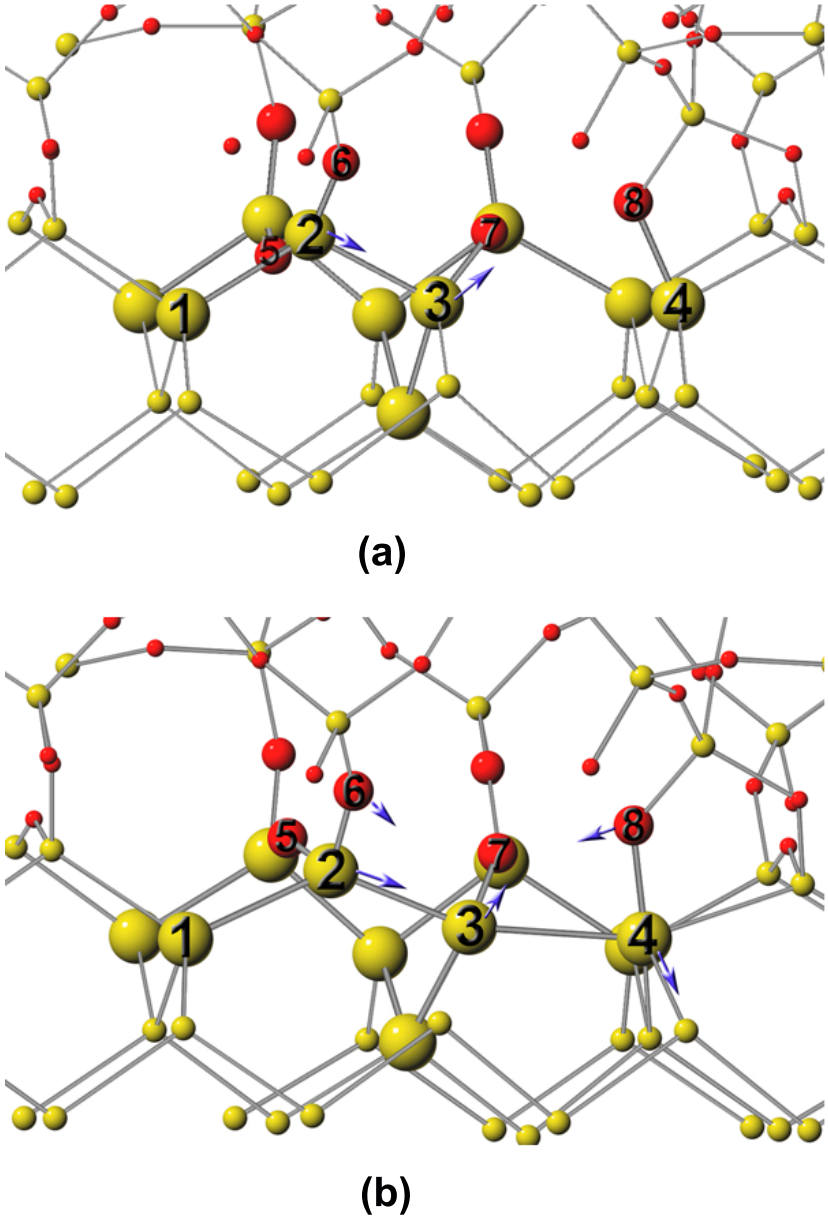

Figure 5.10: Initial configuration (a) and first saddle point (b) of Si vacancy diffusion along Si/SiO_2 interface. Arrows show direction of the atom displacements.

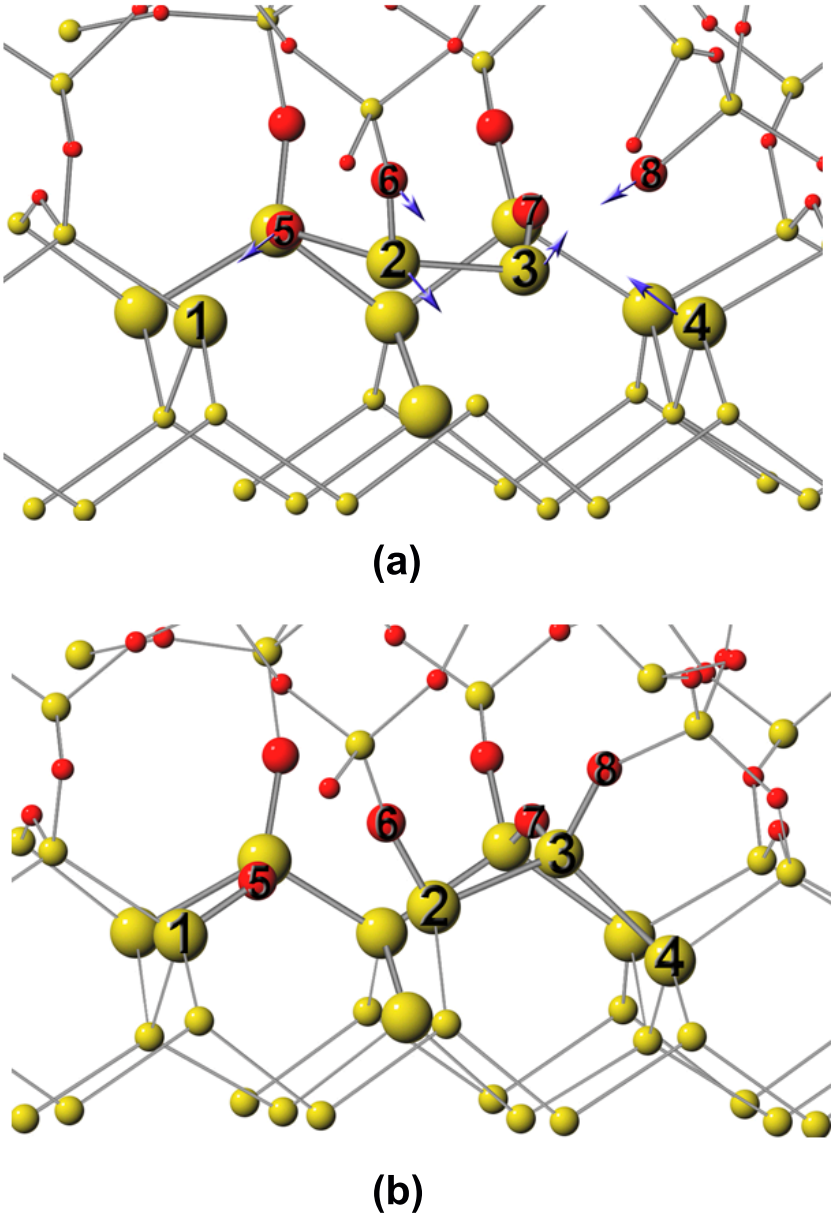

Figure 5.11: Second saddle point (a) and (b) final configuration of vacancy diffusion along Si/SiO_2 interface.

point from the atom 2 and re-bond to the interface Si atom 1. We have tested 4 different locations and found the range of migration barriers from 0.1 eV to 1.3 eV, with the average migration barrier of 0.8 eV. The return barrier is at least 0.5 eV higher, as the surface vacancy is more stable. The wide range of migration barriers and higher return barrier suggests that interface might be an effective sink for vacancies even at low temperatures.

We have also calculated energy barrier and pathway for a vacancy migration along the same interface Si-O-Si row. For the simplicity we have only considered migration between low energy neighboring vacancy sites as the most populated ones. Vacancy migration at the interface involves switching of at least two Si-O bonds. In this case, as can be seen from Fig. 5.10, Si-O bonds 2-5 and 4-8 will be replaced by, correspondingly, Si-O bonds 1-5 and 3-8. Initially sub-interface Si atom 3 moves upward in the direction of neighboring vacancy. Interface Si atom 2 follows, moving in the direction of Si atom 3. At the saddle point 4-8 Si-O bond disconnected, causing sharp increase in total energy. After that 3-8 bond is created and 2-5 bond is disconnected. Finally, 1-5 Si-O bond is created and configuration evolve farther until Si atoms 2 and 3 reach their final positions. Forward (from higher energy vacancy to lower energy vacancy) migration barriers for the pathways between three pairs of neighboring interface vacancies were found to be 0.4-0.8 eV. Thus at sufficiently high temperature interface vacancy can migrate along the Si-O-Si row before either being trapped at low energy location or combine with another vacancy at the same row to form more stable DV defect.

5.5.3 Vacancy clustering at Si/SiO_2 interface

In analogy to the clean Si(100) surface we can expect that interface vacancy agglomerations such as missing dimmer defects might be considerably more stable compared to the separated point vacancy defects.

This expectation is verified by constructing different interface di-vacancy (DV) configurations at several interface locations. It has to be noted that we found the most stable DV at the same interface locations where the most stable single vacancies exist.

In all tested configurations combination of the two single vacancies into DV leads to additional energy reduction per vacancy ranging from 0.2 eV to 0.8 eV. The most stable interface DV is 1.8 eV more stable compared to DV at 5th and 6th c-Si sublayers of c-Si/a-SiO_2 supercell. The most stable interface DV configuration is shown on Fig. 5.12.

For DV construction we remove two Si atoms from the interface Si-O-Si bridge (atoms 6 and 8, Fig. 5.9(a)) and rearrange remaining unpaired O atoms 3,4 and 6 such that four-fold coordination of all atoms in the supercell is restored. In resulting DV structure two Si-O-Si bridges (8-6-9 and 10-4-11) formed in the direction perpendicular to the existing Si-O-Si raw. The remaining O atom 3 may either remain bonded to the interface layer Si atom 5, or disconnect and form a bond with Si atom 2 on SiO_2 side of interface. Which configuration will be the lowest in energy strongly depends on interface site. Stability of each of the two configurations is found to be determined largely by local strain associated with bond topology on the SiO_2 side; that is, more

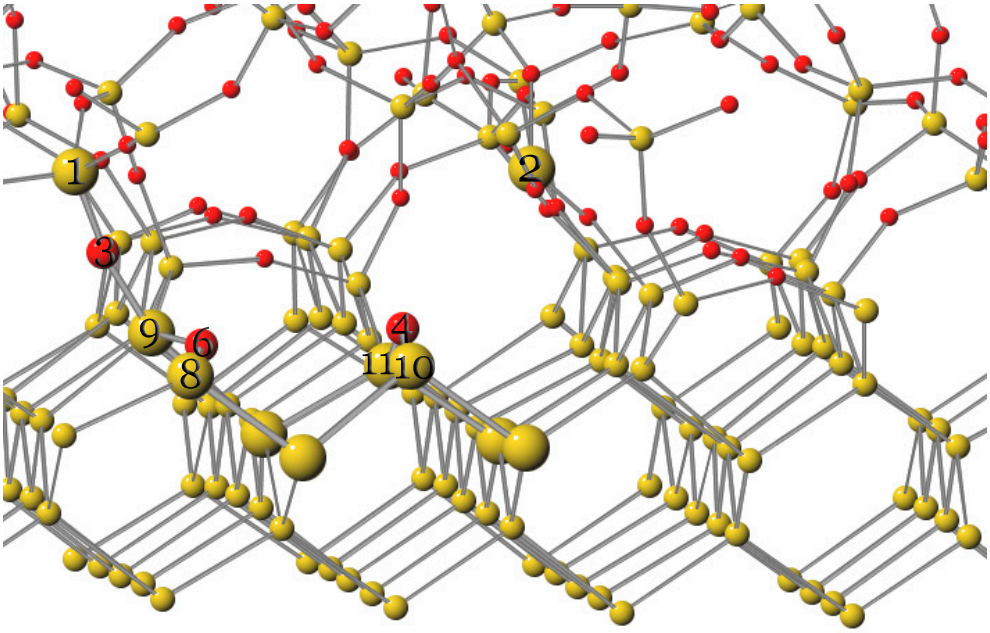

Figure 5.12: Stable di-vacancy structure at Si/SiO_2 interface

flexible bond topology with local compressive strain yields 'fully coordinated' interface DV, whereas local tensile strain results in more stable 'dangling bond' DV. Formation of the 'dangling bond' DV at interface may also be facilitated by the presence of point defects in a-SiO_2 such as oxygen vacancy, what are often present at partially oxidized Si/SiO_2 interfaces[103].

We continue the investigation of stabilization at interface for larger interface vacancy clusters. In the bulk Si binding energy of vacancy to a cluster increases with the cluster size. Contrary to that, our calculations show that beyond DV additional vacancies attach to the existing vacancy cluster more or less independently. Rebonding between interface Si and O atoms upon formation of interface vacancy site introduces strain into the system which

limits the number of vacancies that can be accommodated at interface. Addition of another vacancy to the interface DV does not lead to the considerable additional stabilization per vacancy, trading off advantages of removal of dangling bonds against the cost of strain energy. To check this assumption, first we estimate that stability of tetra-vacancy at the clean reconstructed Si(001) surface formed by two missing neighbor dimmers (type B defect) is 0.4 eV more stable than two separate type A defects. This can be compared to the bulk c-Si, where (symmetric) TV is 3.0 eV more stable than two separate DV. Qualitatively we observe the same trend at the Si/SiO_2 interface. However the lowest energy interface TV we found is 0.1 eV less stable than symmetric TV in bulk c-Si layer. This result may be in part due to the supercell-size limited statistics of the interface TV. Thus we can conclude that interface DV is the most stable interface defect, similar to the missing dimmer (type A defect) defect at Si(001) surface.[15]

5.6 Conclusions

The structure, energetics, bonding, and diffusion of single Si interstitials have been examined in the vicinity of c-Si/c-SiO_2 and c-Si/a-SiO_2 interfaces using planewave basis, pseudopotential total energy calculations. These calculation results show that single Si interstitials can easily migrate from Si to the Si/SiO_2 interface, with no sizable barriers. For both c-Si/c-SiO_2 and c-Si/a-SiO_2 cases, the interface interstitials are energetically far more favorable than bulk interstitials in Si, with an energy gain of greater than 1.0 eV. This clearly supports

a common belief that Si/SiO_2 interfaces are an effective sink for excess interstitials in Si. The bond analysis of interface interstitials based on electron localization functions and local density of states suggests that the interface stabilization can be mainly attributed to the strong chemical bonding of interstitials to Si and/or O lattice atoms with no significant strain induced by lattice distortions. Our calculations also predict that Si interstitials prefer to remain at the interface in the c-Si/c-SiO_2 system, whereas they favorably migrate to the SiO_2 part in the c-Si/a-SiO_2 system. This suggests the migration of excess Si interstitials to the SiO_2 region, rather than interface precipitation, during thermal oxidation and ultrashallow junction formation, as SiO_2 will mostly remain amorphous.

The structure, energetics and bonding interstitial Si atoms have been examined in defect-free c-SiO_2 and amorphous SiO_2 using planewave basis, pseudopotential total energy calculations. In c-SiO_2, we identify that single excess Si atoms can exist at three different energy minimum states including i) fourfold coordinated (FC), ii) bond centered (BC), and ring centered (RC). It turns out that the BC and RC structures are respectively 0.57 eV and 1.8 eV less favorable than the most stable FC structure. Single excess Si atoms are predicted to undergo diffusion via the energy minima, with an overall energy barrier ranging from 2.2 to 2.6 eV. In amorphous SiO_2, stable FC and RC states are identified, but the RC state is unlikely because of the lack of symmetric six-member rings in disordered a-SiO_2. We find that the inserted Si atom can be fully integrated into the amorphous SiO_2 network by succes-

sive O-vacancy diffusion, which in turn yields two separated Si^{3+}-Si^{3+} charge configurations. If fully relaxed, the fully incorporated state is energetically comparable to the FC state, and they are about 2 eV more stable than the BC state. Our extensive calculations suggest that the overall barrier for excess Si diffusion in amorphous SiO_2 is primarily determined by O-vacancy diffusion and Si hopping from a FC site to a BC site.

We found that vacancy formation energy at interface is reduced by 1.9 eV, and even larger stabilization possible for interface vacancy clusters. We can conclude that Si/SiO_2 interface may serve as a (limited) sink for neutral vacancies. Formation of stable vacancy structures may represent an initial step of formation of interface steps Si/SiO_2 interface.

Chapter 6

Behavior of Boron-Interstitial Pairs at Si-SiO_2 Interface

6.1 Introduction

Precise control of dopant redistribution and activation in the vicinity of the semiconductor-dielectric interface has become crucial for fabrication of deep sub-micron metal-oxide -semiconductor field-effect transistor (MOSFET) devices. Ultrashallow junction engineering becomes more challenging due to much more complicated dopant diffusion behavior at interfaces compared to the bulk of the semiconductor. Understanding the exact mechanisms of dopant lateral diffusion, precipitation and segregation at the very interface is largely

hindered by complexity of direct experimental observations. From the modeling side Boron-Interstitial(BI) pair in bulk Si as well as in c-SiO_2 has received a lot of attention recently, but study of BI behavior at the Si/a-SiO_2 is still lacking. In this study we will address the structure, bonding, energetics, and diffusion of boron-interstitial near the Si/SiO_2 interface. In recent theoretical study[104] we consider behavior of Si interstitials in the vicinity of Si/SiO_2 interface. For both c-Si/c-SiO_2 and c-Si/a-SiO_2 cases, we find that the interface interstitials are energetically far more favorable than bulk interstitials in Si, with an energy gain of greater than 1.0 eV. The interface stabilization is mainly attributed to the strong chemical bonding of interstitials to Si and/or O lattice atoms with no significant strain induced by lattice distortions. One could expect that the Si interstitial stabilization may lead to a decline in the stability of interstitial-dopant complexes, such as boron-interstitial (BI) pairs. This in turn may significantly alter the mechanism of diffusion of BI and boron precipitation in the vicinity of Si/SiO_2 interface. As BI pair approaches interface, there are several possible scenarios of BI behavior: i) BI pair may break up to boron at substitutional position (Bs) liberating Si interstitial atom into SiO_2 ii) Boron may be trapped at interface in the form of boron interstitialcy iii) Boron atom nay diffuse into SiO_2. To elucidate boron behavior at interface, in particular boron precipitation at interface and diffusion in SiO_2, we first investigate change of BI, SiI and B_s formation energies at interface. Then we present structure and energetics of stable boron interstitialcy configurations at interface. Finally we consider BI dynamics at interface compared to the bulk

Si, including BI pair break up and interface crossover.

To model Si/SiO_2 interface we consider defect-free Si(001)/amorphous SiO_2 (a-SiO_2) structure. For its construction we use continuous random network (CRN) model [49, 84, 52]. To check the reliability of of the structure constructed using this approach, we also constructed a-SiO_2, with fixed experimental density of 2.2 g/cm^3, yielding the average Si-O-Si bond angle of $136^\circ \pm 15^\circ$, consistent with experimental measurements. [98] We calculate interstitial defect structures and energies using plane-wave pseudopotential method within the density functional theory (DFT) [28, 29], as implemented in Vienna ab-initio Simulation Package (VASP) [30, 31]. The exchange-correlation energy functional is represented using the generalized gradient approximation (GGA) in the Perdew and Wang form (PW91)[37]. To represent nuclei and core electron shells of O and Si atoms we have used ultrasoft Vanderbilt-like [39] pseudo-potentials[54]. Outer electron wave-functions are expanded with plane-wave basis set up to cutoff energy of 210 eV. For the k-space summation, we use the $(2 \times 2 \times 1)$ Monkhorst-Pack mesh[38] and finite temperature smearing.[99] All atoms are fully relaxed using the conjugate gradient method to minimize the total energy until all residual forces on each constituent atom become smaller than $5 \cdot 10^{-2}$ eV/Å. We calculate the diffusion pathways and barriers under the static approximation using the climbing nudged elastic band method. [55]

For reference, we first determined the lowest energy structure of a boron-

interstitial pair in the middle of the Si layer of the model Si-SiO_2 composite system, where the interface effect is insignificant (Fig. 6.1. As predicted in Si bulk previously [105, **?**, 9], the C_3v-symmetry structure (which consists of B substantial and tetrahedral Si interstitial) turns out to be energetically most favorable. Here, we assess the formation of B-Si complexes, compared to the neutral Bs-Si_i pair in the deep Si layer. While their relative stability is still under debate, recent DFT studies have predicted that a Bs-Si_i pair preferably exists positively charged at the intrinsic condition, with an energy gain of (less than eV) relative to the neutral state [**?**]. Furthermore we find stabilization of boron clusters at interface to be more significant.

We also expect the most stable interface boron interstitial complexes to remain neutral. Thus taking into account charged clusters would merely shift reference point by the difference in energy between BsIt0 and $B_sI_t{}^+$, leaving the general picture of B-I behavior at interface intact. Therefore we have restricted our investigation to neutral boron clusters. The picture extracted from our investigation can provide general insight into boron behavior at interface with oxide.

6.2 Structure of BI pair at interface

From an extensive search with several starting configurations we identified the lowest-energy structure of an inserted B atom at each region of the Si-SiO_2 interface system, as depicted in Fig. 1. At the silicon-side interface the B atom shares a lattice site with an adjacent interface Si atom while they are aligned

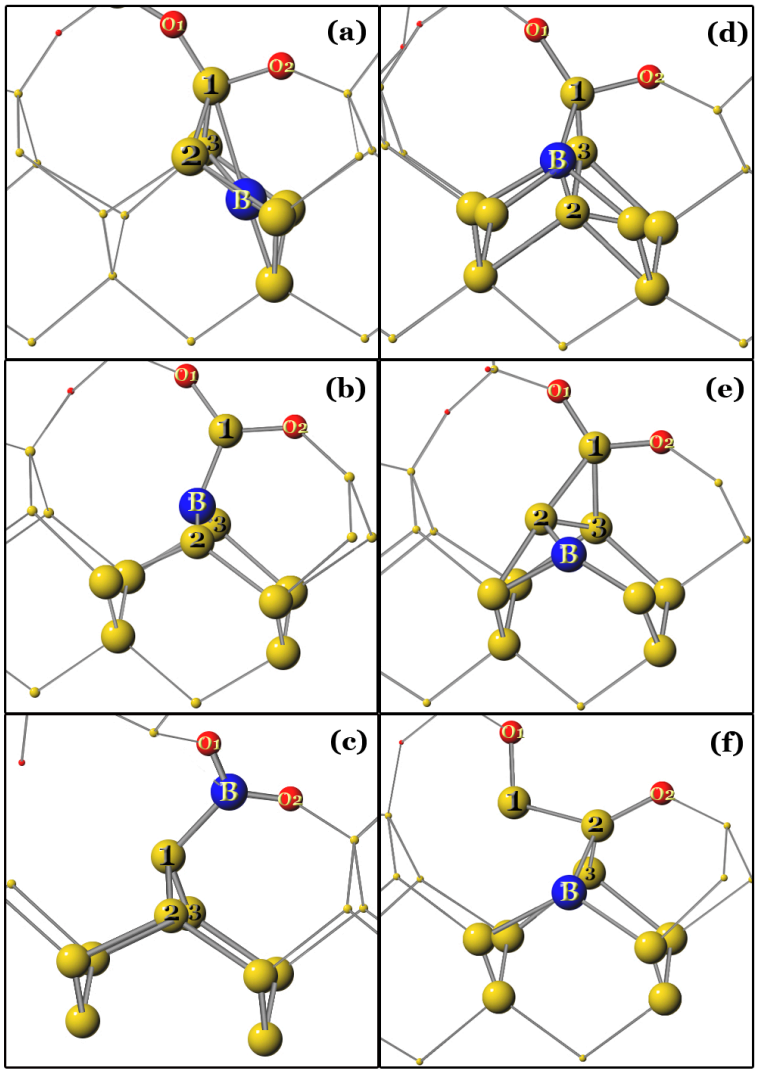

Figure 6.1: Stable and meta-stable Boron-Interstitial configurations near Si/SiO_2. Atoms involved in the BI structure are enlarged. boron atom (B) is shown as blue (large black) sphere, Si atoms are shown as yellow(light gray), oxygen atoms are shown as red (small dark gray) spheres. a) Boron interstitialcy at hexagonal position b) Interface (111)-split boron interstitialcy. c) Boron interstitialcy B_{2O} at the oxide side of interface. d) Subinterface B_sI_t pair. Atom 2 denotes Si interstitial at tetrahedral position. e)Boron-Si(111)-split interstitial pair.Atom 2 denotes Si(111)-split interstitial. f)Boron-BC_I Si interstitial.

in the (111) direction, (which is hereafter referred to as a (111)-split B) (Fig. 6.1(b)). At the oxide-side interface, we fond stable boron interstitialcy (which is hereafter referred to as a B_2O) as shown at Fig.
refconfig(c)). B_2O is formed then B atom breaks two original Si-O bonds and becomes bonded to neighboring Si and two O oxide lattice atoms (Fig. 6.1(c)).

For the (111)-split B, we examined 8 different locations and found that interface B(111)-split configuration is on average 0.5 eV more stable than bulk B_sI_t, with maximum as low as 0.9 eV. Boron atom in B(111)-split configuration becomes three-fold coordinated, forming ideal sp_2 planar bonding configuration with two Si subinterface atoms 2 and 3 (bond lengths 1.96 A) and interface Si atom 1 (bond length 1.85 A). We can expect that existence of stable B(111)-split will significantly alter mechanism of boron migration along interface, especially in the direction parallel to the Si-O-Si bridge.

For B_2O we found that formation energy of the configuration drops by 0.8 eV compared to the bulk B_sI_t pair, with the most stable configuration to be 1.6eV lower in energy. In B_2O configuration boron atom becomes bonded to Si atom 1 and two bridging oxygen atoms O1 and O2 (Fig.6.1(c)). All four atoms (B, O1, O2 and 1) what form the B_2O structure belong to the same plane, thus B atom forms sp_2-like bonds similar to the interface B (111)-split.

In the bulk SiO_2, stable boron interstitialcy (referred to as B_O) of the energy comparable to B_2O can be formed. In the B_O configuration boron atom intervenes between Si and O atoms and becomes twofold coordinated, forming the structure similar to the recently reported in theoretical study of boron-

related defects in c-SiO_2. We found that the formation energies of B_O is larger than B_2O, with the most stable structure 0.6 eV lower in energy compared to the bulk B_sI_t.

Although stable boron interstitialcy are substantially more stable at interface compared to the bulk, interface B-I pair with boron and substitutional site and Si interstitial at stable interface (111)-split site is more energetically favorable. To estimate stability of interface B-I pair we separately examine stable Si interstitial structures and substituional boron at several locations at the Si/SiO_2 interface.

The Si interstitials in oxide and at interface turn out to be substantially more stable compared to the interstitials in bulk Si. This stabilization can be mainly attributed to bond formation with neighboring lattice Si and/or O atoms. The most stable one is about 1.6 eV (Si(111)-split at interface) and 1.8 eV (BC Si interstitial in the a-SiO_2) more stable than the (110)-split bulk interstitial, with an average energy gain of 0.4-0.5 eV.

We calculated change of Bs formation energy at several locations at subinterface layers by replacing Si atoms with boron and relaxing the structure. On average the Bs is 0.2 eV lower in energy at the first two subinterface layers compared to the fifths sublayer (considered to be bulk Si layer), with the most and least stable Bs are correspondingly 0.4 eV lower and 0.1eV higher in energy compared to the Bs in the bulk. This reduction in total energy can be attributed either to the effect of compressive strain induced by SiO_2

in subinterface Si layers or to the change in electronic structure as B placed closer to interface. To check this assumption we perform calculations of boron formation energy change in the bulk $(2 \times 2 \times 2)$ (64 Si atoms) supercell. We found that formation energy of boron monotonically decrease with level of uniform compressive strain with the rate of -0.3 eV/kBar.

We find that interface B-I pair comprised of B substituional and Si(111)-split

Given 1.8 eV Si interstitial stabilization at interface combined with observed slight stabilization of B_s at interface of up to 0.4 eV we can conclude that both B(111) and B_{2O} are metastable with respect to break up to interface Si interstitial and subinterface substitutional boron. Indeed, separate B_s and interface Si_I are more energetically favorable than any of interface or bulk B-I pair. Therefore, it is more likely that interstitial Si diffuses into the SiO_2 layer while leaving substitutional boron behind, rather than having interstitial boron diffuse over the interface and segregate into SiO_2.

We also examine change in energy of B-I pair with its location with respect to Si/SiO_2 interface. We find that on average its formation energy decreases noticeably by 0.2 eV. This reduction can be attributed mainly to the effect of strain exerted by SiO_2 on Si substrate. Indeed, the strain field varies from the compressive for the regions located under Si-O-Si bridges to the tensile for regions directly under the troughs between Si-O-Si rows. Thus this B_sI_t stabilization can be associated with stabilization of unpaired B_s and/or I_t.

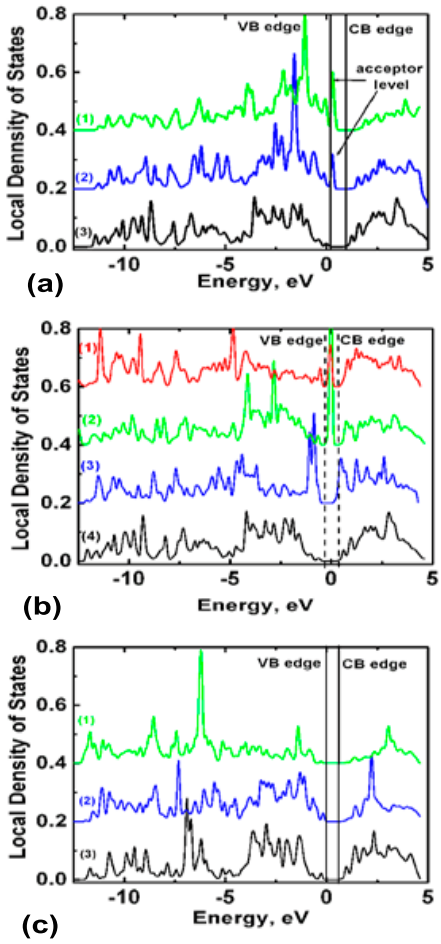

Figure 6.2: Normalized electronic Local Density of States for: a) Boron atom at substitutional site: (1) near the Si/SiO_2 interface; (2) in the Si bulk; (3) reference Si atom in the bulk. b) (1) Boron atom at hexagonal position; (2) one of the six Si nearest neighbors of boron at hexagonal position (3) Interstitials SI atom in B_sI_t pair; (4) reference Si atom in the bulk. c) (1) Boron interstitialcy (2) split(111) boron interstitialcy at interface; (3) reference Si atom in the bulk. Two vertical lines denote positions of bulk Si valence and conduction band edges. Oxygen 2s states of oxygen atom in the bulk SiO_2 is used as a reference energy for different defect supercells. LDOS of each atom is normalized to unity. Vertical coordinate for each subsequent to (1) DOS is offset by 0.2 for clarity.

6.3 Electronic structure

We look at a change in the electronic structure of boron interstitialcy at hexagonal site (B_{hex})) and boron-interstitial B_sI_t pair configurations based on their local densities of states (LDOS) [Fig. 6.2]. B_sI_t does not introduce any deep KS levels in the Si energy gap. It is know that I_t induces two levels: one of the a1 symmetry below the valence band maxima and a triply-degenerate *t2* symmetry level just at or slightly below the conduction band minima. Presence of the B_s at the nearest neighbor position results in symmetry reduction from T_d possessed by the tetrahedral interstitial structure to C_3v and consequently split of the triply degenerate *t2* level into two. But the magnitude of split is small and the lower-splitted doubly-degenerate level is still located shallow below the conduction band bottom. If boron atom placed at interstitialcy position such as B at hexagonal site we can clearly observe deep KS levels in the gap. For B_hex we observe formation of two deep KS levels. For the lower one the corresponding impurity orbitals are localized at the boron atom site. For the higher boron-induced KS level the corresponding orbitals are centered around boron site and smeared in the region of the perturbed bonds of the nearest Si neighbors. On the contrary, split-(111) boron at interface does not show any impurity-induced KS levels in or close to the energy gap (Fig. 6.2(c)). This is a direct consequence of the perfect bonding of the boron with its Si neighbors at interface.

Presence of two oxygen neighbors make notable deference in electronic

structure and energy of the B_{2O} interface boron interstitialcy. As can be seen from the Fig. 6.2(c) the resonance among two stronger B-O bonds opens up the energy gap. Stronger B-O bonds are expected to yield more binding energy compared to B-Si bonds.

It is interesting to note changes in Bs electronic structure with position below the interface. For B_s close to interface occupation of the Kohn-Sham (KS) level corresponding to acceptor level of boron drops. (Strictly, the KS energy levels do not exactly correspond to occupancy levels. In addition, each KS level in supercell is, in principle, subject to dispersion which makes its exact position in the system eigenspectra somewhat ambiguous.) This drop is directly reflected in decrease in total energy of the B_s at sub-interface layers. The 'accepted' by subinterface B_s atom electron is more involved in the bonding with surrounding atoms. However for B_s located close to interface, peak in DOS at the acceptor level appears at the same position and is significantly higher compared to the bulk B_s (Fig. 6.2 (a)). This may be an indication that boron at substitutional site in the vicinity of interface likely remains to be a good acceptor.

6.4 BI pair diffusion at interface

Next we discuss the diffusion of B at the vicinity of Si-SiO_2 interface. In bulk Si the lowest energy migration pathway for neutral BI diffusion between two stable B_sI_t configurations proceeds through hexagonal site. [105]. At interface there are two possible scenarios: i) Boron out-diffusion in oxide (Fig.6.3(a)) ;

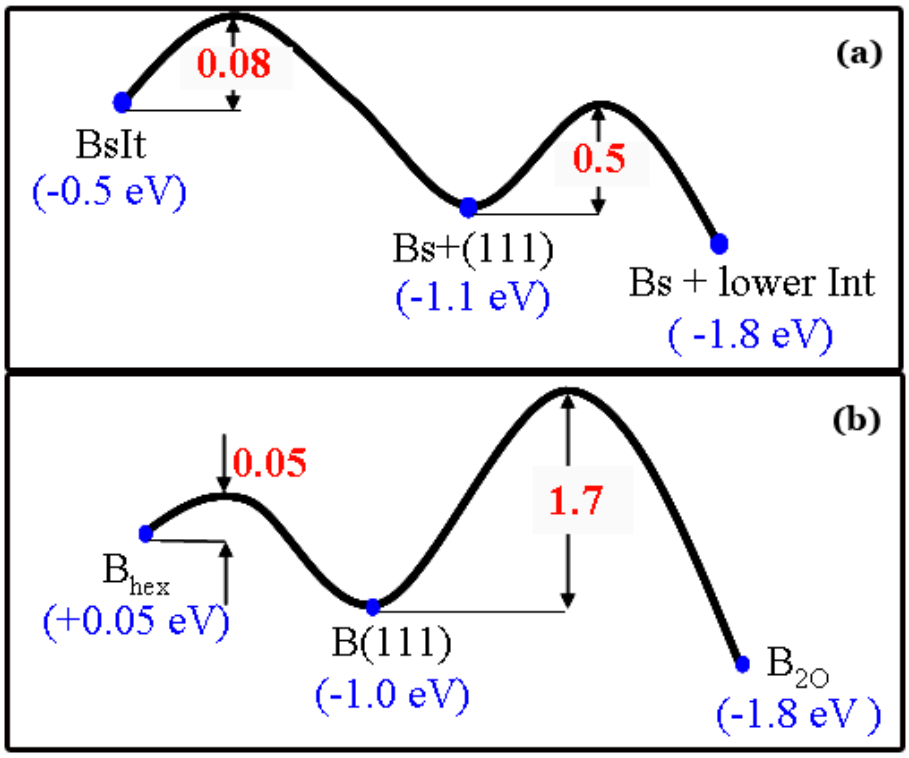

Figure 6.3: BI pair diffusion at interface. (a) Boron out-diffusion in oxide (b)BI pair break-up

ii) Separation of BI pair into B_s and interface Si interstitial Si_I and Si_I diffusion into oxide (Fig.6.3(b)). Next we consider both of these possibilities in detail.

Sub-interface hexagonal Bi found to be unstable and converge quickly to the (111)-split boron configuration in all tested locations. Interface (111)-split configuration can be accessed from sub-interface hexagonal site(Fig. 6.1 (a)) by overcoming energy barrier of 0.06 eV. Once boron atom is trapped in (111)-split, next diffusion jump either along or across interface would require

extra energy to break at least one of the bonds formed between boron and Si atoms. To reach the B_2O in the oxide configuration, boron has to overcome relatively large migration barrier. To migrate form the B(111)-split to B_2O boron atom B has to exchange its position with Si atom 1. For the pathway between the most stable B(111)-split configuration and B_2O configuration we found the migration barrier of 1.0 eV.

We find the migration barrier for boron interstitial diffusion across the Si/SiO_2 to be much (approximately 1.5 eV) higher than jump between two B(111)-split configurations. Thus we can expect that B(111)-split, although metastable with respect to dissociation to interface Bs and Si interface interstitial, may be substantially populated at low temperatures.

For the same interface site we calculate the energy barrier of B_sI_t (Fig. 6.1(d))interstitial break up at interface into Bs and interface interstitial in (111)-split configuration (Fig. 6.1(e)) to be 0.06 eV. Energy barrier of the Si interstitial cross-over to SiO_2 side of interface is 0.1-0.4 eV, suggesting that the Si (111)-split interstitial may quickly convert to Si-O bond-centered interstitial (Fig. 6.1(f)) lowering the total energy of the system. This break-up process is essentially limited by self-interstitial diffusivity, with an energy barrier equal to the migration energy of interstitial diffusion to the interface site.

Thus we can conclude that the scenario of BI breakup at interface is predominant, whereas boron diffusion into oxide is likely to happen at high concentrations of Si interstitials.

6.5 Conclusions

In summary, we have found that boron interstitials are more stable at the Si/SiO_2 interface than in the bulk Si layer. As a result of Si interstitial stabilization at interface BI pairs may easily dissociate as they approach the interface. Si interstitial will migrate into SiO_2, leaving boron atom substitutional site at interface. With significant flux of interstitials or at low temperatures this behavior may change, leading to large boron precipitation at interface in the form of stable (111)-split interstitialcy.

Chapter 7

Charged Defects and Impurities in Si: Supercell Calculations

7.1 Corrections in the total energy calculation of charged defects and impurities

Some defects in semiconductors contribute part of their valence electrons to the conduction band or to levels in the gap. Formation energies of such defects are underestimated by DFT calculation[107, 108]. In order to calculate formation energies of these defects correctly, we have to derive an efficient method for determining corrections to defect supercell total energies. The difficulty lies in that we have to account for changes in the energy in the infinite defect-

crystal system as well as changes due to finite size of a supercell. These corrections may be difficult to extract from the first-principles calculation. In the following chapter, we attempt to derive total energy corrections based only on the information from first principle calculation.

Infinite supercell correction−In this study we consider the case of T-interstitial defect. In a T-interstitial, two s-electrons form the states below the valence band maximum and two p-electrons form the resonance states above the conduction band minima. In an infinitely large supercell, these two p-electrons will be given up to the conduction band and will be attracted to the positively charged interstitial to form two shallow donor levels, similar to the effect of shallow donor impurities [such as B, As and P] in Si. Thus, in order to obtain correct energy of the T-interstitial(as proposed by W.A. Harrison [107]), we have to add a constant shift in energy for the two electrons (which is equal to the difference between calculated and experimental gap $\Delta = E_g - E_g^{DFT}$), and subtract the energy of the donor states that lie 0.03 eV and 0.09 eV below the conduction band minima. The first and the second donor states will be located under six of the conduction band minima in (100) direction. Approximating the real donor state by the hydrogen-like state and taking the geometric mean of the longitudinal and transverse electron mass, we will have the first and second donor levels correspondingly at E_{donor} =0.03 eV and 0.09 eV below conduction band minima.

Finite size correction−In the finite size supercell, these donor levels will interfere with each other and may be broadened into conduction bands. The

defect induced p-electron resonance is also broadened due to interaction with the nearest defect images and may become partially occupied as the Fermi level is shifted. First, consider the occupation of the conduction band and the resonance formed by p-states of the defect by its electrons. For the finite size supercell, the defect donor levels overlap each other and intermix with conduction bands. As a result, defect electrons from these levels appear in the conduction bands and fill them up to the Fermi energy E_f. This leads to an increase in the supercell total energy by $\frac{3}{5}Z_cE_f$, where Z_c is the number of electrons occupying the conduction band levels. As we place the p-state electrons into the conduction band, they form a resonance that is broadened into the resonance band. To calculate occupancy Z_r of resonance(after W.A. Harrison[107]) we assume that resonance is centered at some energy E_r above the conduction band minimum and forms a band with a constant density of states and a finite width W. For three defect p-states of either spin, available number of states for resonance band is $\frac{6}{W}$, out of which

$$\frac{6}{W}(E_f - (E_r - \frac{W}{2})) \tag{7.1}$$

will be occupied as the fermi level E_f crosses resonance bands. Hence, the total energy of supercell will be raised by

$$\frac{1}{2}Z_r(E_f + (E_r - \frac{W}{2})), \tag{7.2}$$

where E_f and E_r are both taken with respect to the conduction band minimum. There is also a minor correction due to the coulombic shift in the resonance states which is equal to $\frac{1}{2}Z_c^2\Delta$.

Combining the correction for the infinite supercell with shifts in energy due to limited size of the supercell, we obtain the following expression for correction to the formation energy of the T-interstitial:

$$E_c = (Z_c + Z_r)\Delta - E_{donor} - \frac{3}{5}Z_c E_f - \frac{1}{2}Z_r(E_f + (E_r - \frac{W}{2})) + \frac{1}{2}Z_c^2\Delta. \quad (7.3)$$

7.2 Description of the method

7.2.1 Charged defects calculation: jellium countercharge and LMCC approaches

The conventional approach[109] to evaluate the energy of the charged supercell assumes the introduction of the homogeneous countercharge background (uniform charge jellium). It keeps the supercell neutral and helps to avoid the monopole-monopole interaction of the supercell with its periodic images which would lead to divergence of the Coulomb energy for the charged defects. The supercell total energy has to be adjusted for the electrostatic energy of the charged defect interacting with the jellium background as well as with induced defect-jellium electrostatic momenta. For the cubic supercell this correction is equal to

$$E_D^q(L) = E_D^q - \frac{\alpha q^2}{2\epsilon L} - \frac{2\pi qQ}{3\epsilon L^3}, \quad (7.4)$$

where α stands for Madelung constant, L represents the length of the supercell, and Q is the quadrupole momentum induced by the charged defect.

For different values of the electron chemical potential, formation energy E_f of the charged defect is evaluated as

$$E_f^q(\mu_e) = E_D^q(L) - E_{Si} + q(E_\nu + \mu_e). \tag{7.5}$$

where $E_D^q(L)$ is the total energy of the charged defect supercell, E_ν is the valance band edge position, μ_e is the chemical potential ($0 \leq \mu_e \leq E_g$), E_{Si} is the total energy of the bulk Si with the same number of atoms as in the defect supercell. E_{Si} is calculated as the difference in energy of the perfect bulk supercell and the cell with one missing electron from the highest occupied state (i.e. valence-band edge state).

An alternative to the jellium countercharge approach is the local moment counter-charge (LMCC) method[110, 111, 112] . In LMCC approach, one can introduce an aperiodic array of countercharges in the supercell such that it cancels out all leading electrostatic moments of the charged defect. The major disadvantage of this method is that it is hard to implement into existing DFT tools and there is no analytical formula available for the LMCC correction to the total energy. It is expected to converge with the size of the supercell at the same rate as the jellium approach[109]

Both jellium and LMCC approaches can give very accurate results for systems where the Fermi level is not located in the gap (such as for metallic systems), or where there are no considerable changes of the Fermi level with

doping (insulators). To calculate the charged defect formation energy at the different Fermi level positions, the total energy of the supercell is combined with the electron chemical potential. The value of electron chemical potential is bounded by the experimental band gap of 1.12 eV.

7.2.2 Doped supercell approach

After application of all necessary corrections[113], the jellium approach gives an adequate estimate of defect formation energies at the valence band edge. The change of the formation energy of the charged defect as the Fermi level changes with the temperature or doping concentration is assumed to be equal to the change of electron chemical potential and given by formula (7.4). This assumption may not be adequate for correct prediction of charged defect formation energy at a given Fermi level.

We propose to apply correction to the electron chemical potential such that its value is scaled proportionally to the defect donor/acceptor level position in the gap. The electron chemical potential that coincides with valence band edge will receive no correction and the electron chemical potential at the conduction band edge will be aligned with experimental band edge so that the change of electron chemical potential in the gap is still bounded by the value of the experimental band gap. For the formation energy dependence on the Fermi level position [instead of using (7.4)], we adopt the formula with scaled

chemical potential:

$$E_f^q(\mu_e = E_D^q(L) - E_{Si} = q(E_\nu + K\mu_e), \tag{7.6}$$

where

$$K = \frac{E_D^0 - (qE_\nu + E_D^q(L) - E_{Si})}{E_{di}} \tag{7.7}$$

is the scaling factor, E_{di} is the calculated value of electron chemical potential at which defect changes its charge state ((+/0) ionization level), E_D^0 is the neutral defect energy ($0 \leq \mu_e \leq E_g$). E_g and E_g^{DFT} are the experimental and calculated band gaps respectively. This approach gives us a more reliable way of scaling formation energies of defects as chemical potential changes.

To determine the correct scaling coefficient, we need to have reliable values of the defect ionization levels. To obtain defect ionization levels, we replace one of the Si atoms in the bulk with an acceptor that has a shallow level in the gap. We need to place an acceptor atom as far as possible from the defect within the supercell. This is done in order to avoid any elastic interactions between the defect and the acceptor atom. In the same way we can find second donor (ionization) level of the interstitial by putting two acceptor atoms in the supercell. If the donor level of the defect is below the acceptor level of the introduced dopant atom, an energetically favorable level in the gap will be created and it will be occupied by one electron of the defect, resulting in a charge defect in the cell. In this method, the neutrality of the cell is preserved at all times. After application of energy corrections for the induced

ionized acceptor (the charged defect electrostatic interaction and defect-boron induced interaction with periodic images) we can extract the donor ((+/0) ionization) level of the defect. It should be noted that the calculated donor level position should be shifted to correct for DFT band gap underestimation.

Thus we essentially use only the total energies obtained from the DFT calculation to find ionization levels of the defect. The scaling is needed for mapping of the donor level position in the calculated band gap to the position in the experimental band gap. In principle, a method similar to this can be used to estimate acceptor levels of defects if they exist in the gap. To do this, a Si atom in the bulk has to be replaced with a shallow donor atom.

7.3 Application to interstitials and boron-interstitial complexes

7.3.1 Silicon interstitial ionisation levels

First, we performed energy calculations for the neutral T-interstitial structure. From the band structure calculation of the bulk 216 atom supercell, we found Δ =0.66 eV (0.49 eV). From the calculated density of states (DOS) of the defect atom, we have E_r =0.56 eV (0.41 eV) above the conduction band minima, W =1.26 eV (0.92 eV), and E_f =0.175 eV (0.113 eV). This computation is close to the Fermi level value of 0.13 eV (0.08 eV) from the supercell calculation. The corresponding occupation of resonance bands is 0.37 electrons (0.53 electrons) and occupation of 1.63 (1.47 electrons) electrons per

conduction band in the 217 atom supercell. From these results, we calculate the shift in energy due to the finite size of the supercell to be 0.177 eV (0.09 eV). The correction to the total energy of the neutral T-interstitial supercell $E_{correction}$ =1.02 eV (0.76 eV). This results in a T-interstitial formation energy of 4.56 eV.

Next, we calculate the ionization (donor) levels of the T interstitial. The formation energy of singly (T^{+}) and doubly (T^{++}) positively charged T-interstitials is calculated with the jellium countercharge background. Similar to the neutral T-interstitial case, we have to add a correction of 0.56 eV (0.41 eV) due to the occupation of resonance and conduction band states to the total energy of T^{+} interstitial supercell. We have also adjusted the total energy of the supercell to account for the electrostatic interaction of the jellium background with the charged interstitial by 0.105 eV (0.104 eV). For the T^{++} interstitial, we have adjusted the total energy by 0.419 eV (0.415 eV) to account for the jellium-defect electrostatic interaction. No additional correction is needed for the total energy of the T^{++} interstitial supercell since the defect p-states are empty. In order to obtain the formation energies of the charged interstitials as a function of Fermi level, we scaled the formation energies using expression (7.4). The formation energy change as a function of electron chemical potential is shown in Fig. 1. Predicted first and second donor levels of the T-interstitial are located respectively at 1.03 eV (1.12 eV) and 0.95 eV (1.03 eV) from the valence band edge. Both levels are located very close to the conduction band edge.

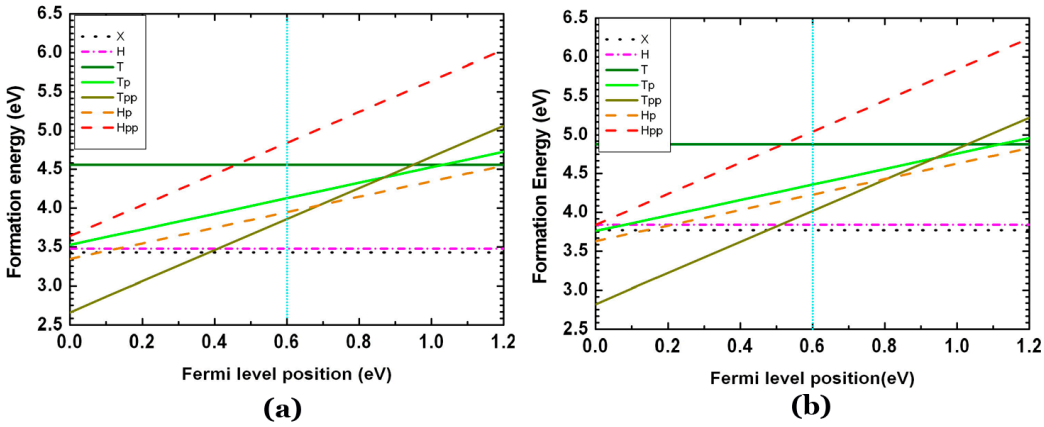

Figure 7.1: Silicon interstitial formation energy dependence on Fermi level position with applied electron chemical potential scaling: (a) LDA and (b) GGA calculation.

From the doped supercell approach, we found that the T interstitial (+/0) ionization level is located 1.05 eV above valence band maximum and the (++/0) donor level is located 0.95 eV above valence band maximum. These results are in excellent agreement with the jellium approach calculation. As it can be seen from Figure 7.1, H and the (110) split interstitial states are the most stable for the Fermi levels above 0.4 eV (0.5 eV).

The doped supercell method allows us to estimate the magnitude of corrections needed for the occupied donor levels of the defect. We can apply this method where it is not easy to provide an analytical formula for the corrections to the total energy of defect supercell, such as in the case of dopant-defect complexes.

As a test case, we calculated the corrections to the total energy of the Boron-Interstitial (BI) pair. From the doped supercell approach, we found

the donor level of the BI pair to be 0.99 eV, in remarkable agreement with experimental observation of a BI donor level of E_c−0.13 eV.

7.3.2 Interstitial diffusion pathway

In this part we revisit the interstitial diffusion in different charge states. Interstitial diffusion may be significantly enhanced at cirtain Fermi level positions as the most stable charge state may change with a change in Fermi level. First, we consider neutral interstitial diffusion. Several low migration energy diffusion pathways are possible such as H-T-H, X-T-X and X-H-X pathways.

As can be seen from Fig.7.1 the X and H sites are the most stable interstitial states for the intrinsic Fermi level. Therefore, it is likely that the X-H-X pathway is the preferable diffusion pathway for the interstitial as the migration barrier would be essentially very close to the total energy difference between H and X sites. We estimate the migration barrier to be on the order of 0.1 eV.

According to Fig.7.1, the T^{++} interstitial becomes the most stable interstitial state for the heavily p-doped Si. The diffusing interstitial atom may capture hole or electron and change its charge state along the pathway (Bourgoin-Corbett mechanism). As T^{++} captures two electrons, it will slide to the neighboring H or X position without having to overcome any migration barrier. Alternatively, the capture of two holes will lead to formation of the T^{++} configuration without having to overcome any potential barrier.

Chapter 8

Summary and Future Work

8.1 Summary of contributions

This dissertation presents several innovative models of defect and dopant behaviors in complex systems such as Si(001) surface, amorphous-crystalline Si and Si-SiO_2 interfaces. The major contributions of this dissertation in the field of semiconductor device fabrication are summarized below.

• Vacancies and interstitials at Si(001)surface:

We examine structure, energetics, and bonding of vacancies and interstitials on the clean and terminated Si(001) surface and its subsurface layers. We propose mechanism of vacancy stabilisation at the surface and subsurface layers. We find that the formation energy of vacancies (interstitials) at the surface is about 2.5 eV (3.2 eV) lower than that at the fifth subsurface layer.

We find both vacancies and interstitials within topmost three subsurface layers are significantly stabilized by their strong interactions with the surface. Their formation energies are predicted to be a few eV lower than those in the bulk. The significant stabilization of vacancy at the subsurface layers is mainly attributed to i) the reduction of dangling bonds in the subsurface layers as a result of rearrangement of surface atoms and ii) the delocalization of electrons on the local surface.

This study suggests that a large fraction of neutral vacancies(interstitials) may reside at surface and subsurface layers. We present diffusion pathways and barriers of vacancies at and in the vicinity of the clean surface. We propose a new mechanism for monovacancy annihilation and single missing dimer creation. Our study shows that an isolated monovacancy can exist fairly stable, rather than liberating the remaining atom of the 'defect' dimer readily. The liberation barrier is calculated to be 1.3 eV. However, the monovacancy can diffuse rapidly along a dimer row by overcoming a barrier of 0.4 eV, leading to vacancy-vacancy pairing at elevated temperatures. These results suggest that the vacancy-vacancy pairing may play a major role in creating a single missing-dimer vacancy (which is 1.7 eV more stable than two isolated monovacancies). We present the pathways and barriers of i) the remaining atom hopping between the buckled-up and down site of the 'defect' dimer and ii) the vacancy diffusion into the subsurface layer.

We find Si(001) surface to be an effective sink for vacancies and interstitials, irrespective of surface passivation.However, our calculations show that

the stability of vacancies and interstitials within the topmost three subsurface layers is greatly influenced by surface passivation. For a single vacancy, compared to the fifth layer one, the formation energy reduces by 2.2 (1.5) eV and 0.8-1.0 (0.8-0.9) eV at the second (third) sub-surface layer in the clean and terminated-surface cases, respectively.

This stability difference at the sub-surface layers implies that the terminated surfaces are not as effective as the clean surface for the surface annihilation of vacancies and interstitials.

• Vacancies and interstitials at amorphous-crystalline Si interface:

We present native defects configuration, energetics and the origin of their stabilization at *a-c* Si interface and in amorphous Si. We find that both vacancies and interstitials prefer to reside on the amorphous side of the interface. In both cases, the most stable defects occur 3-4 Åfrom the a-c interface.Vacancies and interstitials in the a-Si side are predicted to be approximately 2.5 eV and 2.0 eV more stable than those in the crystalline Si part, respectively. After careful analysis it was possible to deduce the mechanisms of vacancy and interstitials stabilization. Vacancy stabilization is found to be due to strain relief provided to the substrate lattice while interstitial stabilization is due largely to bond rearrangement arising from interstitial integration into the substrate lattice.

This study suggests that substrate subamorphization may play an im-

portant role in controlling the density and spatial distribution of defects, and consequently, dopant TED and electrical activation. Our results provide a potential explanation for the dopant TED reduction and enhanced dopant activation that have been experimentally observed when subamorphization strategies have been employed.

• Vacancies, interstitials and Boron-Interstitial pairs at Si-SiO_2 interface:

We have examined the behavior of single Si interstitials in the vicinity of Si/SiO_2 interface. The interface interstitials turn out to be substantially more stable than bulk interstitials in Si, mainly due to bond formation with neighboring lattice Si and/or O atoms. We have identified three stable interstitial configurations at the interfaces, including (111)-split, Si^{2+}-O bond centered, and Si^{4+}-O bond centered. For both *c*-Si/*c*-SiO_2 and *c*-Si/*a*-SiO_2 cases, the interface interstitials are energetically far more favorable than bulk interstitials in Si, with an energy gain of greater than 1.0 eV. We have calculated the diffusion of interstitials from the Si part to the Si/SiO_2 interface, showing the ease of the interface stabilization with no sizable barrier. We also discuss the migration of Si interstitials into the SiO_2 layer at the *c*-Si/*c*-SiO_2 and *c*-Si/textita-SiO_2 interfaces. We have investigated the structure of Si interstitials in c-SiO_2 and *a*-SiO_2 and identified two stable Si interstitial configurations: i) Fourfold-coordinated and ii) Bond-centered. We found that silicon interstitials can readily get into network in amorphous silicon dioxide.

Our calculations predict that Si interstitials prefer to remain at the interface in the c-Si/c-SiO_2 system, whereas they favorably migrate to the SiO_2 part in the c-Si/a-SiO_2 system. This suggests the migration of excess Si interstitials to the SiO_2 region, rather than interface precipitation, during thermal oxidation and ultrashallow junction formation.

We propose original mechanism of vacancy stabilisation and vacancy clustering at interface. Single vacancy and vacancy cluster defects are substantially more stable at c-Si-/aSiO2 interface compared to the bulk c-Si layers away from interface, mainly due to termination of dangling bonds with bridging O atoms and reduction of interface strain. Vacancy formation energy at interface is reduced by 1.9 eV, and even larger stabilization per vacancy is possible for interface vacancy clusters. We propose migration pathway for vacancy diffusion from subinterface to interface as well as vacancy diffusion along interface.

We demonstrated that Si/SiO_2 interface may serve as a (limited) sink for Si vacancies. Unlike interstitials, vacancies do not migrate into SiO_2 and their aglomeration may lead to formation of stable interface vacancy clusters.

We investigated Boron-Interstitial (BI) pair behavior in vicinity of defect-free Si/a-SiO_2 interface. Our results suggest that a-SiO_2 serves as a partially absorbing barrier to the boron diffusion across the interface. We found Boron interstitialcy configurations at interface what are substentially more stable

than BI pairs in the bulk Si.

We found that the interstitial stabilization at Si/SiO_2 interface results in a decline of stability of boron-interstitial complexes, possibly leading to BI break up and facilitating boron precipitation at the $Si\text{-}SiO_2$ interface.

• Correction to the total energy of charged supercells:

We propose original method of correction for total energy of the periodic supercell with charged defect. This method allows to perform consistent calculation of the charged defect formation energies. The method was applied for the calculation of ionisation levels for Si interstitial and Boron-Interstial pair binding energy.

8.2 Suggestions for future work

Although great efforts have been made in the study of defects and dopants behavior at surfaces and interfaces there are many questions that remain. The most pertinent unresolved issues what stem from the results of the present work are as follows:

Behavior of charged defects:

Only neutral defects have been considered in this work. We suspect that behavior of charged defects and dopant-defect complexes may be substantially different from the neutral ones thus defects in charged states should be considered in future work. Developing reliable and physically sound methods of charge and finite size corrections extending the ones proposed in chapter 7

should be applied in the study of the charged defects.

Multi-scale modeling:

Implementation of the key findings on dopant-defect behavior in a Monte-Carlo simulator is necessary to assess validity of the models as well as make practical use of the obtained results. The direct experimental confirmation of the results of this dissertation is only possible on the larger time and length scales. In regards to the parameter extraction from the presented work for continuum or MC simulations it should be noted that all results obtained here are at 0 K. Although we expect that essential mechanisms will remain the same at finite temperatures, particular numerical values should be checked carefully before applying them to the modeling of processes at high temperature.

Si/high-k interfaces:

Investigation of physical properties and dynamical behavior of native defects and dopant-defect complexes at the HfO_2/Si and $Hf_xSi_{1-x}O$/Si interfaces. The DFT calculations with localized base sets and/or ab initio tight binding calculations have to be used to explore the defect-dopant properties and dynamics.

Bibliography

[1] International technology roadmap for semiconductors: 2003 edition,WWW Docuument, public.itrs.net/2003ITRS/Home2003.html.

[2] E.C. Jones. and E. Ishida. *Mat. Sci. and Eng. R-Reports*, 24:1, 1998.

[3] S.C. Jain, W. Schoenmaker, R. Lindsay, P.A. Stolk, S. Decoutere, M. Willander, and H.E. Maes. *J. Appl. Phys.*, 91:8919, 2002.

[4] J. Xu, V. Krishnamoorphy, K. S. Jones, and M. E. Law. *J.Appl. Phys.*, 81:107, 1997.

[5] J. Liu, V. Krishnamoorphy, H.-J. Gossman, L. Rubin, M. E. Law, and K. S. Jones. *J.Appl. Phys.*, 81:1656, 1997.

[6] H.Saleh, M.E. Law, S. Bharatan, K.S. Jones, V. Krishnamoorthy, and T. Buyuklimanli. *Appl. Phys. Lett*, 77:112, 1992.

[7] M.J. Caturla. *Comp.Mat. Sci.*, 12:319, 1998.

[8] S.K.Theiss, M. J. Caturla, M.D. Johnson, and et al. *Thin Solid Films*, 365:219, 2000.

[9] T.J. Lenosky, B. Sadigh, S.K. Theiss, and et al. *Appl. Phys. Lett.*, 77:1834, 2000.

[10] D.C. Mueller, E. Alonso, and W. Fichtner. *Phys. Rev. B*, 68, 2003.

[11] A Hofler, Th. Feudel, N.Strecker, W.Fichtner, K.-H. Stegemann, H. Syhre, and G. Dallmann. *J. Appl. Phys*, 78:3671, 1995.

[12] J.C Lopez and M. Acevedo. *Phys. Stat. Sol.*, 173:289, 1999.

[13] T.J. Lenosky, B. Sadigh, S. Theiss, and M-J. Caturla. *Appl. Phys. Lett.*, 77:1834, 2000.

[14] R.J. Needs. *J. Phys.: Condens Matter*, 84:3555, 1999.

[15] W.-K. Leung, R.J.Needs, and G. Rajagopal. *Phys. Rev. Lett.*, 83:2351, 1999.

[16] K. Kato. *J. Phys.: Condens Matter*, 5:6387, 1993.

[17] S. Goedecker, T. Deutsch, and L. Billard. *Phys. Rev. Lett.*, 88:235501, 2002.

[18] G.S. Hwang and W.A. Goddard. *Phys. Rev. B*, 65:233205, 2002.

[19] S.T.Dunham. *J. Appl. Phys.*, 71:685, 1992.

[20] R. J. Hamers, R.M. Tromp, and J.E.Demuth. *Phys. Rev. B*, 34:5343, 1986.

[21] T. Aruga and Y. Murata. *Phys. Rev. B*, 34:5654, 1986.

[22] C. Tsamis and D. Tsoukalas. *J. Appl. Phys.*, 84:6650, 1998.

[23] M.E. Law, Y.M. Haddara, and K.S.Jones. *J. Appl. Phys.*, 84:3555, 1998.

[24] B. Sadigh, T. J.Lenosky, S.K. Theiss, M-J. Caturla, T.D. de la Rubia, and M. A. Foad. *Phys. Rev. Lett*, 83:4341, 1999.

[25] L.A. Marques, L. Pelaz, J. Hernandez, and J. Barbolla. *Phys. Rev. B*, 64:045214, 2001.

[26] S.T. Pantelides. *Phys. Rev. Lett.*, 57:2979, 1986.

[27] P.M. Fahey, P.B. Griffin, and J.D. Plummer. *Rev. Mod. Phys.*, 68, 2003.

[28] P.Hohenberg and W.Kohn. *Phys. Rev.*, 136:B864, 1964.

[29] W. Kohn and L.J. Sham. *Phys. Rev.*, 140:A1133, 1965.

[30] G. Kresse and J. Hafner. *Phys. Rev. B*, 47:RC558, 1993.

[31] G. Kresse and J. Furthmuller. *VASP the Guide*. Vienna Univ. of Technology, 2001.

[32] M. C. Payne et al. *Rev. Mod. Phys.*, 64:1045, 1994.

[33] N. Argaman et al. *Am. J. Phys.*, 68:69, 2000.

[34] W. Kohn, A. D. Becke, and R. G. Parr. *J. Phys. Chem.*, 100:12974, 1996.

[35] J. P. Perdew, K. Burke, and M. Ernzerhof. *Phys. Rev. Lett.*, 77:3865, 1996.

[36] G. Kresse and J. Hafner. *J. Phys.: Condens. Matter*, 6:8245, 1994.

[37] J. P. Perdew and Y. Wang. *Phys. Rev. B*, 45:13244, 1992.

[38] H.J. Monkhorst and J.D. Pack. *Phys. Rev. B*, 13:5188, 1976.

[39] D. Vanderbilt. *Phys. Rev. B*, 32:8412, 1985.

[40] R. F. W. Bader. *J. Chem. Phys.*, 73:2871, 1980.

[41] R. F. W. Bader and H. Essen. *J. Chem. Phys.*, 80:1943, 1984.

[42] R. F. W. Bader. *Atoms in Molecules: A Quantum Theory*. Oxford Univ. Press, 1960.

[43] B. Silvi and A. Savin. *Nature*, 371:683, 1994.

[44] B. Silvi. *J. Phys. Chem. A*, 107:3081, 2003.

[45] A.D. Becke and K.E. Edgecombe. *J. Chem. Phys.*, 92:5397, 1990.

[46] P.N. Keating. *Phys. Rev.*, 145:637, 1966.

[47] W.H. Zachariasen. *J.of Chem. Am. Society*, 54:3841, 1932.

[48] D.E. Polk. *J. of Non-crystaline solids*, 5:365, 1971.

[49] F. Wooten, K. Winer, and D. Weaire. *Phys. Rev. Lett.*, 54:1392, 1985.

[50] R. Vink, G. Barkena, M. Stijnman, and R.Bisseling. *Phys. Rev. B*, 64:245214, 2001.

[51] G. Barkema and N. Mousseau. *Phys. Rev. B*, 62:4985, 2000.

[52] Y. Tu, J. Tersoff, and G. Grinstein. *Phys. Rev. Lett.*, 81:4899, 1998.

[53] K. Laaziri, S. Kycia, S. Roorda, M. Chicoine, J. Robertson, J. Wang, and S. Moss. *Phys. Rev. B*, 60:13520, 1999.

[54] A.M. Rappe, K.M. Rabe, E.Kaxiras, and J.D. Joannopoulos. *Phys. Rev. B*, 41:1227, 1990.

[55] G. Henkelman, B.P.Uberuaga, and H. Jonsson. *J. Chem. Phys.*, 113:9901, 2000.

[56] D. J. Chadi. *Phys. Rev. Lett.*, 43:43, 1979.

[57] N. Roberts and R. J. Needs. *Surf. Sci.*, 236:112, 1990.

[58] J. E. Northrup. *Phys. Rev. B*, 47:10032, 1993.

[59] J. Fritsch and P. Pavone. *Surf. Sci.*, 344:159, 1995.

[60] A. Redondo and W. A. Goddard III. *J. Vac. Sci. Technol.*, 21:344, 1982.

[61] Z. Jing and J. L. Whitten. *Surf. Sci.*, 274:106, 1992.

[62] K. C. Low, H. S. Lim, and C. K. Ong. *J. Phys. Condens. Matter*, 6:9551, 1994.

[63] G.S. Hwang and W.A. Goddard. *Phys. Rev. Lett.*, 89:233205, 2002.

[64] T. Uda and K. Terakura. *Phys. Rev. B*, 53:6999, 1996.

[65] G. D. Watkins. *in Defects and Their Structure in Non-metallic Solids*. Plenum, New York, 1976.

[66] G. D. Watkins. *in Deep Centers in Semiconductors*. Grodon and Breach, New York, 1986.

[67] M. I. J. Probert and M. C. Payne. *Phys. Rev. B*, 67, 2003.

[68] L. J. Munro and D. J. Wales. *Phys. Rev. B*, 59:3969, 1999.

[69] O. Sugino and A. Oshiyama. *Phys. Rev. Lett.*, 68:1858, 1992.

[70] O. Pankratov, H. Huang, T. Diaz, delaRubia, and C. Mailhiot. *Phys. Rev. B*, 56:13172, 1997.

[71] M.J. Puska, S. Poykko, M. Pesola, and R.M. Nieminen. *Phys. Rev. B*, 58:1318, 1998.

[72] Z. Y. Zhang and H. Metiu. *Phys. Rev. B*, 48:8166, 1993.

[73] T. A. Kirichenko, S. K. Banerjee, and G. S. Hwang. *Surf. Sci.*, 555:187, 2004.

[74] P.M. Fahey, P.B. Griffin, and J.D. Plummer. *Rev. Mod. Phys.*, 61:289, 1989.

[75] M. Ramamoorthy and S.T. Pantelides. *Phys. Rev. Lett.*, 76:4753, 1996.

[76] S. Solmi, M. Ferri, M. Bersani, D. Giubertoni, and V. Soncini. *J. Appl. Phys.*, 94:4959, 2003.

[77] M. L. Y. Jung, R. Gunawan, R. D. Braatz, and E. G. Seebauer. *J. Elecrochem. Soc.*, 151, 2004.

[78] P. A. Stolk, D. J. Eaglesham, H. J. Gossman, and J. M. Poate. *Appl. Phys. Lett.*, 66:1370, 1995.

[79] D. W. Lawther, U. Myler, P. J. Simpson, P. M. Rousseau, P.B. Griffin, and J. D. Plummer. *Appl. Phys. Lett.*, 67:3575, 1995.

[80] L. Pelaz, M. Jariaiz amd G. Gilmer, H. J. Grossman, C. S. Rafferty, D. J. Eaglesham, and J. M. Poate. *Appl. Phys. Lett.*, 70:2285, 1997.

[81] K. C. Pandey, A. Erbil, G. S. Cardill III, and R. F. Boehme. *Phys. Rev. Lett.*, 61:1282, 1988.

[82] W. W. Luo, S. Z. Yang, P. Clancy, and M. O. Thompson. *J. Appl. Phys.*, 90:2262, 2001.

[83] V. Ranki, K. Saarinen, J. Fage-Pederson, J. Lundsgaard Hansen, and A. Nylandsted Larsen. *Phys. Rev. B*, 67, 2003.

[84] V.M. Burlakov, G.A.D. Brigs, A.P. Sutton, and Y. Tsukahara. *Phys. Rev. Lett.*, 86:3052, 2001.

[85] D. Vanderbilt. *Phys. Rev. B*, 41:7892, 1990.

[86] A. Sultan, S. Banerjee, S. List, and V. mcNeil. *J. Appl. Phys.*, 83:8046, 1998.

[87] S. Aronowitz, H. Pluchner, and J. Kimball. *J. Appl. Phys.*, 85:3494, 1999.

[88] T. Schenkel, A. Persaud, S. J. Park, J. Nillson, J. Bokor, J. A. Liddle, R. Keller, D. H. Schneider, D. W. Cheng, and D. E. Humphries. *J. Appl. Phys.*, 94:7017, 2003.

[89] S. Whelan, A. La Magna, V. Privitera, and et al. *Phys. Rev. B*, 67, 2003.

[90] G. Fortunato, L. Mariucci, A. La Magna, and et al. *Appl. Phys. Lett.*, 85:2268, 2004.

[91] S. Lombardo, B. De Salvo, C. Gerardi, and et al. *Microelectronics Ehgineering*, 72:388, 2004.

[92] S. Tiwari, F. Rana, H. Hanafi, and et al. *Appl. Phys. Lett.*, 68:1377, 1996.

[93] B. Fernandez, M. Lopez, C. Garcia, and et al. *J. Appl. Phys.*, 84:876, 2002.

[94] D.J. Chadi. *Phys. Rev. B*, 64:195403, 2001.

[95] T.A Kirichenko, S.K. Banerjee, and G.S. Hwang. *Phys. Rev. B*, 70:045321, 2004.

[96] T.A.Kirichenko, S.K. Banerjee, and G.S. Hwang. *Phys. Stat. Sol. B*, 241:2303, 2004.

[97] S.T.Dunham and C. D. Wu. *J. Appl. Phys.*, 78:2362, 1995.

[98] A. Brunet-Bruneau, D. Souche, S. Fisson, Van V.N., G. Vuye, F. Abeles, and J. Rivory. *J. Vac. Sci. Tech. A*, 16:2281, 1998.

[99] N.D. Mermin. *Phys. Rev.*, 137:A 1441, 1965.

[100] A. A. Demkov, X. Zhang, and D. A. Drabold. *Phys. Rev. B*, 64:125306, 2001.

[101] D.R Hamann. *Phys. Rev. B*, 61:9899, 2000.

[102] D. Yu, T.A. Kirichenko, G.S. Hwang, and S. Banerjee. submitted to Phys. Rev. B.

[103] Y.Tu and J. Tersoff. *Phys. Rev. Lett.*, 84:4393, 2000.

[104] T.A. Kirichenko, D. Yu, G.S Hwang, and S. K. Banarjee. in press, 2005.

[105] W.Windl, M. Bunea, R. Stumpf, S.T. Dunham, and M. P. Masquelier. *Phys. Rev. Lett.*, 83:4345, 1999.

[106] L. Lin, T. Kirichenko, S.K. Banerjee, and G.S. Hwang. *J. Appl. Phys.*, 96:5543, 2004.

[107] W.A. Harrison. *Mat. Res. Symp. Proc.*, 469:211, 1997.

[108] W.Windl. *Phys. Stat. Sol. B*, 241:2313, 2004.

[109] G. Makov and M.C. Payne. *Phys. Rev. B*, 51:4014, 1995.

[110] P.A Schultz. *Phys. Rev. Lett.*, 84:1942, 2000.

[111] P.A Schultz. *Phys. Rev. B*, 60:1551, 1999.

[112] L.N. Kantorovich. *Phys. Rev. B*, 60:15476, 1999.

[113] J. Shim, E.-K. Lee, Y.J. Lee, and R.M. Nieminen. *Phys. Rev. B*, 71:035206, 2005.

Vita

Taras Alexandrovich Kirichenko was born in Kiev, Ukraine on February 1977, the son of Galina Kirichenko and Alexander Kirichenko. After graduating from Ukrainian Lyceum of Physics and Mathematics, Kiev, Ukraine, in 1994 he entered Moscow Institute of Physics and Technology in Moscow, Russia. During 1998 he worked as a undergraduate research assistant at Institute for Nuclear Research, Troitsk, Russia. He received the degree of Bachelor of Science in Physics and Applied Mathematics from Moscow Institute of Physics and Technology in May, 1998. In August 1998, he entered The Graduate School at The University of Texas, Department of Physics. In 2001 he transferred to the Department of Electrical and Computer Engineering, The University of Texas at Austin. He recevied his MS in Electricfal Engineering in May, 2002. He joined Freescale semiconductor as a Technology Computer Aided Design engineer in December, 2004.

Permanent Address: N. Lamar apt 201, Austin TX, 78751

This dissertation was typeset with LaTeX 2$_\varepsilon$[1] by the author.

[1] LaTeX 2$_\varepsilon$ is an extension of LaTeX. LaTeX is a collection of macros for TeX. TeX is a trademark of the American Mathematical Society. The macros used in formatting this dissertation were written by Dinesh Das, Department of Computer Sciences, The University of Texas at Austin, and extended by Bert Kay, James A. Bednar, and Ayman El-Khashab.